

GRAN SASSO SCIENCE INSTITUTE
ASTROPARTICLE PHYSICS DOCTORAL PROGRAMME
CYCLE XXXIII 2017-2020

**SEARCHES OF A COSMOLOGICAL
GRAVITATIONAL-WAVE BACKGROUND
WITH 3G DETECTORS: PROBING THE
VERY EARLY UNIVERSE**

Ph.D. Candidate:
Ashish Sharma

Advisor:
Prof. Jan Harms



Searches of a Cosmological Gravitational-Wave Background with 3G Detectors: Probing the Very Early Universe

A Dissertation Presented

By

Ashish Sharma

In Partial Fulfilment of the Requirements for the

Degree of

Doctor of Philosophy

Advisor:

Prof. Jan Harms

January 29, 2021

GSSI Gran Sasso Science Institute

Viale Francesco Crispi, 7 - 67100 L'Aquila - Italy

Abstract

Gravitational-wave detection from compact binary coalescences with current gravitational-wave detectors has made a tremendous impact on our understanding of astrophysical sources and look forward to the stochastic gravitational-wave background (SGWB) signal detection. An SGWB comprises superpositions of numerous astrophysical and cosmological sources, providing a direct window to study early universe phenomena and fundamental physics. Observation of the early universe gravitational-wave background signal would be paramount. Till yet, there is no direct or statistical evidence of stochastic cosmological gravitational-wave background (SCGWB) signal apart from upper limits has placed on the associated parameters after analyzing the advanced Laser Interferometer Gravitational-Wave Observatory (aLIGO) and advanced Virgo (AdV) data.

With the proposed third-generation ground-based gravitational-wave detectors, Einstein Telescope and Cosmic Explorer, we might be able to detect evidence of an SCGWB. However, digging out these prime signals would be a challenging quest as the dominance of the astrophysical foreground from compact binary coalescences will mask the SCGWB. This idea to deal with the foreground signal and increase future gravitational-wave detector's sensitivity toward SCGWB searches led to the foundation of the work presented in the thesis.

In this work, I study a subtraction-noise projection method with future ground-based detectors, which first subtracts the dominating foreground signals from compact binary coalescences and then makes it possible to reduce the residuals left after subtraction of a foreground of compact binary coalescences, significantly improving our chances to detect an SCGWB. The subtraction of the foreground signal depends upon the accurate parameter estimation of individual binary signals present in the detector data. I carried out the analysis using posterior sampling for the parameter estimation of binary black hole mergers.

The removal of an astrophysical foreground in future detectors with potentially several 10^5 signals per year will be computationally very challenging. I extended state-of-the-art Bayesian parameter estimation and detector modeling

software (Bilby) to incorporate foreground reduction methods based on geometric interpretations of matched filtering. I also developed a numerical approach for the calculation of Fisher matrices that allows the implementation of arbitrary waveform models, i.e. not only the analytical ones.

As a result, I demonstrate the sensitivity improvement of SCGWB searches and find that the ultimate sensitivity of SCGWB searches will not be limited due to residuals left after subtracting the estimated binary black holes foreground. However, the fraction of the astrophysical foreground that cannot be detected even with third-generation instruments, or the possible presence of other signals (non-deterministic astrophysical stochastic background signals) can further impact the sensitivity towards the SCGWB searches.

To search for an isotropic SGWB and their statistical evidence in aLIGO and AdV data, I am involved in research activities with the stochastic group of LIGO VIRGO Collaboration contributing to data analysis and isotropic SGWB searches. The main objective of my contribution is, to analyze the whole third observation run data of aLIGO and AdV, and look for variations in the signal if present, i.e. coherence between the different baselines of aLIGO and AdV detectors. And then to use a stochastic energy density spectrum following a power-law distribution to check for SGWBs either of astrophysical or cosmological origin based on the power-law index, which characterizes the background signal and then helps to put upper limits on the respective SGWB. I, therefore, present the upper limits on isotropic SGWB searches from the third observation run of aLIGO and AdV detectors data. The limits on the isotropic SGWB from the third observation run stochastic data analysis improved by a significant factor in comparison to the upper limits from the first and the second observation run stochastic data analysis.

To my parents

Acknowledgements

I would like to acknowledge and thank all those people without whom I would not be here, and this work would not have been possible.

First, I would like to express my gratitude to my advisor Jan Harms for introducing me to gravitational-wave physics and most importantly, how to analyse the data. When I started, I have not had any knowledge about fundamental gravitational-wave research. Still, thanks to your lectures, also my first formal lectures on gravitational-waves and detector physics, gave me the curiosity to know more about gravitational-wave detection and analysis. Besides physics and research, I learned so many things from you on a personal level.

I would like to thank you Luca Rei from INFN Pisa, without whose help most of the results in this thesis would not be complete. Thank you, Luca, for helping me out with how to use INFN-CNAF cluster resources and all the associated problems.

I would like to thank Andrew Matas, for providing me with an opportunity to analyse the aLIGO and AdV third observation run data and helping me with understanding the codes and digging out deep-buried secrets inside the plots, and also for all those unconditional help with coding issues.

Thanks to karthik, Austin, Valentina, Ambra, Antonio, Francesca and Stefan for sharing an amazing bond and the time we shared with each other.

Without the contribution of my family, everything would always be incomplete. My mother and father, thank you for guiding me at each and every step of my life with your wisdom and character. My sisters, Sanjeev and Sushil, thank you for your unconditional love, support and care.

Contents

Abstract

Acknowledgements

List of Figures

List of Tables

Abbreviations

1	Gravitational waves and detectors	1
1.1	General relativity	2
1.2	Generation of GWs	8
1.3	Gravitational wave detectors	9
1.3.1	Interferometer detector	9
1.3.2	AdV interferometer	11
1.3.2.1	AdV detector layout	12
1.3.3	Noise contribution to sensitivity	14
1.4	Future generation GW Detectors	18
1.4.1	Cosmic Explorer	19
1.4.2	Einstein Telescope	21
1.4.3	GW source for 3G detectors	24
1.5	Global network of GW detectors	25
2	Stochastic Gravitational Wave Background : sources and detection	27
2.1	SGWB from different source	29
2.2	Astrophysical SGWB	31
2.2.1	Estimation of astrophysical SGWB	35
2.3	Cosmological stochastic GW background	38
2.3.1	Phase Transition in the early universe	39
2.3.1.1	Scalar field contribution	40

2.3.1.2	Sound waves contribution	42
2.3.1.3	MHD contribution	43
2.3.2	Cosmic Strings	44
2.3.2.1	Limits from GW detection	48
2.3.3	GWs from inflation	51
2.3.4	Primordial black holes	53
3	Subtraction-noise projection method for SCGWB searches	57
3.1	Introduction	57
3.2	Simulation overview	61
3.3	Matched filtering and Fisher matrix	68
3.3.1	Binary parameters	68
3.3.2	Fisher matrix for signal analysis	69
3.4	CBC waveform template	74
3.5	Sources of confusion noise	77
3.5.1	Overlapping in binary signals	77
3.5.2	Overlapping in waveform	78
3.5.3	Subtraction of best-fit waveforms	79
3.5.4	Waveform model systematic	85
3.6	Projection of subtraction residuals	88
3.6.1	Projection operator and residual noise	88
3.6.2	Geometrical interpretation of projection method	96
3.7	SCGWB and detection	98
3.7.1	Cross-correlation between detectors	99
3.7.2	Optimal filtering of CPSDs	101
3.8	Projection results	104
3.9	Conclusion	114
4	O3 Analysis : Upper limits on SGWB	117
4.1	AdV Characterization	117
4.2	SGWB searches in O3 data	126
4.2.1	Optimal filtering of data	126
4.2.2	Cross correlation spectrum	128
4.2.3	O3 data set	129
4.2.4	Data quality cuts	131
4.2.5	Point estimates and sigma errors	132
4.2.6	Upper limits on SGWB	135
4.3	Conclusion	142
5	Conclusion and future prospects	143
A	IMRPhenomPv2 waveform model	147

A.1	PN and NR waveforms	148
A.2	Phenom waveform	150
B	Detector’s geometrical factors	157
B.1	Antenna response function	157
C	Data Analysis Tools	162
C.1	Introduction to statistical inference	162
C.2	Bayesian inference	164
C.2.1	Bayesian parameter estimation	164
C.2.2	Bayesian computational tools	168
C.3	Fisher information matrix	170
C.4	Matched filtering	171
C.5	Cross-correlations	174
C.6	Optimal filter	177
C.7	Overlap reduction function	180

List of Figures

1.1	Deformation of the ring of particles propagating along z direction. GR allow two modes of tensor polarization (plus and cross), alternative or modified theories of GR allows two vector polarizations (x and y) and two scalar polarizations (breathing and longitudinal) (Figure from [64]).	8
1.2	Plot showing the structural Layout of AdV interferometer. The arm cavity of 3km length is formed by Input Mirror (IM) and End Mirror (EM) in each perpendicular arm. These mirrors are also known as the test masses. Recycling cavities of 12m length lie at the centre of the interferometer. (Figure from [28]).	12
1.3	Plot showing the sensitivity curve for aLIGO and AdV GW detectors with anticipated sensitivity curves for future GW detectors in terms of strain sensitivity. Where A ⁺ LIGO corresponds to future aLIGO after upgrades, A ⁺ VIRGO is upgraded version of AdV. In contrast, ET-D represents the sensitivity curve for Einstein Telescope (ET) with xylophone configuration, and CE is the overall sensitivity curve for Cosmic Explorer (CE).	16
1.4	Plot showing the contribution of different noise channels to AdV noise budget and overall sensitivity curve of AdV detector. On frequency scale, one can see the frequency band in which these noise contributions dominate, and limit the detector sensitivity. The plot has been reproduced using for an output power source of 200W using gwinc code [2].	17
1.5	The plot shows the anticipated sensitivity curve for future generation CE detector during stage 1(CE1) and stage 2 (CE2) with the sensitivity curve of A ⁺ and aLIGO GW detector. The sensitivity curve for CE1 and CE2 are from [5].	20

1.6	Einstein Telescope (ET) proposed a triangular shape configuration with high and low frequency interferometers placed at 60° with respect to each other, forming a full ET GW detector. The shape, which is considered to be the final shape till now, is known as Xylophone configuration (ET-D) shown with another proposed ET-C configuration (Figure from [94]). Solid lines represents the original laser beam and dashed lines represent a squeezed laser beam.	22
1.7	Plot showing the anticipated noise budget curve for low frequency ET detector. Different noise sources contribute to the sensitivity of the ET detector at different frequency ranges.	23
1.8	Anticipated noise budget curve showing the contribution towards the high frequency ET detector from various noise sources.	23
1.9	Plot showing the astrophysical reach of non-spinning equal mass binaries accessible with aLIGO, ET, and CE GW detectors (figure from [118]).	24
2.1	A representation of how an SGWB might look like in an observed signal by a GW detector (Figure from [7]).	30
2.2	Plot showing the SGWB spectra from the various cosmological sources and previous limits from aLIGO detector, constraints based on the CMB observations and the pulsar time array (PTA). In addition to the SGWB spectra, the anticipated sensitivity curves for third-generation and LISA detector is shown. The grey band shows the expected SGWB from astrophysical sources (figure from [118]).	31
2.3	The sensitivity curves for combined O1+O2 and O3 run of aLIGO and Adv GW detectors with a design sensitivity for the SGWB singal energy density from BBH, BNS and NS-BH. The purple line shows the total SGWB contribution from BBH and BNS with a Poisson error region in grey box calculated from the local BBH merger rate given in [18] and for BNS a combined merger rate from GW170817 and GW190423 events is used [21].	37
2.4	The SCGWB energy density spectrum from the first-order phase transitions and the sensitivity curves for aLIGO with combined O1 and O2 data (in solid black line) with aLIGO sensitivity (in dashed line) and for ET detector (in dotted line). The grey shade area comes from the indirect upper bound set by Planck CMB data. The blue lines correspond to the bubble wall collision with $\kappa_\phi = 1$, and the red lines shows the sound waves contribution with $\kappa_{SW} = 1$ to the energy density curve for some realization of first-order phase transition model (Figure from [168]).	43

2.5	Plot showing the first-order phase transition energy density spectrum as a function of parameter κ with various ground-based and space-borne GW detector's sensitivity curve (Figure from [77]).	45
2.6	The plot shows the SCGWB energy density spectrum from the cosmic string network for the different realization of parameter $G\mu$ with $\alpha = 0.1$ and the sensitivity curve of aLIGO, future ground-based GW detectors ET and CE, space-borne GW detectors LISA [76], DECIGO [104] and BBO [70] with European Pulsar Time Array (EPTA) and Square Kilometre Array (SKA) (Figure from [71]).	49
2.7	Plot showing the upper limits from different observations with the sensitivity curve of third generation (3G) GW detector, constraints are from aLIGO observations and upper limits on microlensing of SNe, caustic disruption, Planck and other various observations. The shaded region represents the PBH mass distribution (which depends upon the density power spectra) due to the QCD phase transition with a mass density centered at $\sim 10M_{\odot}$ (using merger rates from LIGO observations) [51], for different PBH abundance and a primordial scale invariant spectrum (figure from [124]).	54
2.8	The GW energy density spectrum for PBH merger events in thick solid black line with mass $M_{PBH} = 1M_{\odot}$ and various realization of present energy density fraction $f_{PBH} = 10^{-2}, 10^{-3}, 10^{-4}$ and 10^{-5} is shown with the detection sensitivity of current, future ground-based and space-borne GW detectors (Figure from [106]).	56
3.1	Plots showing the 2D histogram of CE and ET detectors SNR with respect to the redshift of 100 BBH signals used for studies in Case1 and Case2.	62
3.2	Mass range for individual BBH mass used in Case1	65
3.3	Mass range for individual BBH mass used in Case2	65
3.4	Distribution of total mass M and redshift z of the 100 BBH signals used in Case1 analysis. Highest-SNR BBH signals are chosen for clearest possible demonstration of the projection method to mitigate the astrophysical foreground.	66
3.5	Distribution of total mass M and redshift z of the 100 BBH signals with lower SNR values (i.e. $SNR > 10$) are chosen for the demonstration of projection method to mitigate the astrophysical foreground in Case2	67

3.6	Parameter estimation error distribution for luminosity distance D_L (in Figure 3.6a) and orbital inclination angle θ_{jn} (in Figure 3.6b) between the true source parameters (red curve) and best-fit estimated parameters (blue curve) for BBH signals used in Case2 . The green spikes give the mismatch between the true source parameters and the best-fit estimated parameters. Wider the green spikes are, large would be the parameter estimation errors (see Equation (3.12)). Consequently, larger would be the residual noise (Equation (3.13)).	75
3.7	Figure showing the template manifold \mathcal{M} of all physical waveforms embedded into the vector space \mathcal{V}_i of all signals measured by GW detectors. The vector space is represented in two dimensional space by axis $T_i^s(t_1)$ which gives all the GW signals observed by GW detectors at time t_1 while axis $T_i^s(t_N)$ gives the total signals observed at different times t_N within the observation duration T_{obs} . The vector space S_i represent the output of i^{th} GW detector, n_i is the instrumental noise of the GW detector, $n_{i\perp}$ and $n_{i\parallel}$ are the component of residual noise remained after the subtraction of estimated best-fit waveforms. On the manifold \mathcal{M} , points $h_i(\lambda^\alpha)$ and $h_i(\hat{\lambda}^\alpha)$ give the location of true waveform and estimated best-fit waveform defined by their respective parameters. λ^α and λ^β are the binary source parameters provide with the parameter space for a waveform model and locate them on the manifold \mathcal{M} of all possible waveforms. The top right-hand side gives the enhanced view of projection residual on the curved manifold.	84
3.8	Predicted waveform accuracy for current GW detectors, their future upgrades (Aplus and Voyager) and proposed GW detectors (ET and CE) for two binaries <i>left</i> : SXS BBH 0308, and <i>right</i> : SXS BBH 0104. Each panel shows the mismatch in SNR for a GW detector. The solid line represents the NR signals, and dash lines give hybridized PN-NR signals in the inspiral phase. The blue lines with data points show the mismatch, which falls with the rise in SNR of the binary signal. The dashed-dotted grey line shows the systematic errors from waveform inaccuracy which are smaller than statistical errors (Figure from [133]).	86
3.9	Plots are for Case1 without detector noise. Simulated spectrum (i.e. square root of PSDs) of astrophysical foreground after injecting 100 BBH signals (in red), subtraction residuals after subtracting the best-fit signals (in blue), and residual spectrum after projecting out the subtraction residuals (in blue) for ET and CE detector is shown in Figure 3.9a and 3.9b respectively. The change in the curve for ET-D.1 and CE detectors are due to the difference in their sensitivity at low frequencies.	94

3.10	Plots are for Case2 without detector noise. Simulated spectrum (i.e. square root of PSDs) of astrophysical foreground after injecting 100 BBH signals (in red), subtraction residuals after subtracting the best-fit signals (in blue), and residual spectrum after projecting out the subtraction residuals (in blue) for ET and CE detector is shown in Figure 3.10a and 3.10b respectively. The change in the curve for ET-D_1 and CE detectors are due to the difference in their sensitivity at low frequencies.	95
3.11	Plot showing the ORF $\gamma(f)$ between Cosmic Explorer at aLIGO Hanford location (CE-H), Cosmic Explorer at aLIGO Livingston location (CE-L) and Einstein Telescope (ET) at AdV location. The CE-H and CE-L are L-shape detectors, and ET is a triangular shape detector. The ORFs is shown in logarithmic frequency axis. Note that the ORF between different detectors of the ET triangle is constant with a value of about -0.38. For the subtraction-noise projection method and analysis, I used CE-H (CE as used) and ET detector network pair.	100
3.12	Plot showing the Optimal filter function $\tilde{Q}(f)$ between Cosmic Explorer at aLIGO Hanford location (CE-H), Cosmic Explorer at aLIGO Livingston location (CE-L) and Einstein Telescope (ET) at AdV location. The CE-H and CE-L are L-shape detectors, and ET is a triangular shape detector. The optimal filters between detectors of the ET triangle are all identical. For the subtraction-noise projection method and analysis, I used CE-H (CE as used) and ET detector network pair.	103
3.13	SNR of a flat $\Omega_{GW} = 2 \cdot 10^{-12}$ stochastic background. The curves are the SNRs accumulated from high to low frequencies. Total observation time is 1.3 years. The ORF between CE and ET is used with triangular shape ET detector and L shape CE detector.	104
3.14	Plots are for Case1. Plots of CSDs for CE and ET-D_1 detector pair with a BBH foreground 3.14a, after best-fit subtraction 3.14b, and after noise projection 3.14c. The CPSDs are 1.3-year averages with a total of 10^6 injected BBHs. The astrophysical reference model (red curve) is only an approximation valid below about 100 Hz since it is predicted to fall more strongly above 100 Hz. The purple curve represents an SCGWB with frequency-independent $\Omega_{GW} = 10^{-15}$. The blue curves are the simulated CPSD measurements. The green curve is the predicted instrument noise. The orange curves show the CPSD for simulations without instrument noise.	108

3.15	<p>Plots are for Case1. Plots of residual CSDs averaged over all ET detector pairs with BBH foreground Figure 3.15a, after estimated best-fit BBH signals subtraction Figure 3.15b, and after subtraction residuals projection Figure 3.15c. The CPSDs are 1.3-year averages and also averaged over all detector pairs of the ET triangle with a total of 10^6 injected BBHs. The astrophysical reference model (red curve) is only an approximation valid below about 100 Hz since it is predicted to fall more strongly above 100 Hz. The purple curve represents an SCGWB with frequency-independent $\Omega_{GW} = 10^{-15}$. The blue curves are the simulated CPSD measurements. The green curve is the predicted instrument noise. The orange curves show the CPSD for simulations without instrument noise.</p>	110
3.16	<p>Plots are for Case2. Plots of residual CSDs for CE and ET-D.1 detector pair with BBH foreground Figure 3.16a, after best-fit subtraction Figure 3.16b, and after residual noise projection Figure 3.16c for Case2. The CPSDs are 1.3-year averages with a total of 10^6 injected BBHs. The astrophysical reference model (red curve) is only an approximation valid below about 100 Hz since it is predicted to fall more strongly above 100 Hz. The purple curve represents an SCGWB with frequency-independent $\Omega_{GW} = 10^{-15}$. The blue curves are the simulated CPSD measurements. The green curve is the predicted instrument noise. The orange curves show the CPSD for simulations without instrument noise.</p>	112
3.17	<p>Plots are for Case2. Plots of residual CSDs averaged over all ET detector pairs with BBH foreground Figure 3.17a, after best-fit subtraction Figure 3.17b, and after noise projection Figure 3.17c. The CPSDs are 1.3-year averages and also averaged over all detector pairs of the ET triangle with a total of 10^6 injected BBHs. The astrophysical reference model (red curve) is only an approximation valid below about 100 Hz since it is predicted to fall more strongly above 100 Hz. The purple curve represents an SCGWB with frequency-independent $\Omega_{GW} = 10^{-15}$. The blue curves are the simulated CPSD measurements. The green curve is the predicted instrument noise. The orange curves show the CPSD for simulations without instrument noise.</p>	114
4.1	<p>Flicker noise (in cyan color) after the replacement of photodiodes which is altogether constant above 50 Hz. The red curve shows the difference between the audio channels.</p>	119
4.2	<p>An increase in flicker noise (in cyan color) a night before the observation (see Figure 4.1). The red curve shows the difference between the audio channels.</p>	119

4.3	The frequency line at 80 Hz starts to rise in the AdV spectrum from January 26, 2020, onwards.	120
4.4	Plot showing high correlation between the 80 Hz frequency line and ENV_NE_CT_ACC_Z.	121
4.5	Plot showing the coherence investigation between Herc and the main environmental channel (CEB-IPS, CEB-UPS and CEB-Magnetic) of the AdV detector site. The Coherence value in the frequency range (46 - 48) Hz is in range (0.10-0.24), while coherence in frequency range (50-54) Hz is in range (0.20-0.40).	122
4.6	Plot showing the coherence investigation between Herc and the main environmental channel (NEB-Mangetic, NEB-Seismic and WEB-Seismic) of the AdV detector site.	122
4.7	Plot showing the acoustic coherence between Herc and the CEB_UPS, WEB_UPS and NEB_UPS of the AdV detector site. The coherence with UPS lines before mitigating 48 Hz in WEB_UPS (purple color line) and after that (blue color line) shows an apparent reduction in the coherence level.	123
4.8	Plot showing that AdV reached 59 Mpc BNS range during O3 observational run. Plot was produced by AdV group. Y-axis is in Mpc.	123
4.9	Time Frequency distribution of transient noise detected by Omicron on February 3, 2020 in AdV data.	124
4.10	The glitch occurred due to the movement between the suspension fibre edge and the mirror.	125
4.11	Spectrum observed during the glitch in Figure 4.10 providing information about the event dynamics.	125
4.12	Histogram showing the total O3B data and data after applying the $\delta\sigma$ cut for L1V1 baseline.	131
4.13	Kolomogorov-Smirnov test for L1V1 baseline to check for the Gaussianity of dataset after the data quality cuts applied.	132
4.14	Plot showing the optimal estimator Ω for L1V1 baseline over the number of observation days for O3B data.	133
4.15	Histogram showing the distribution of excess residual correlated noise (i.e. ratio between standard deviation Ω and the corresponding statistical uncertainty σ_Ω) for L1V1 baseline data with 192 s segment before and after the data quality cuts.	134
4.16	Plots showing the trend of optimal estimator Ω (top right), σ (bottom left), ratio of standard deviation of Ω with σ (bottom right) over the whole O3B run for L1V1 baseline.	135
4.17	IFFT spectrum of point estimates for L1V1 baseline. If spectrum has a sharp features near zero lag, it could be the signature of the stochastic signal in the dataset.	136

4.18	Running point estimates Ω are shown over the course of the run for the L1V1 baseline. In the presence of a signal the spectrum will be smooth towards the observed value. The data quality cuts have been applied for the analysis.	136
4.19	The cross-correlation spectrum obtained after combining the O3 run data from all baselines (H1L1, H1V1, L1V1) with a power-law index $\alpha = 0$ and $\pm 1\sigma$ uncertainty level in the red and yellow line.	139
4.20	The cross-correlation spectrum obtained after combining the O3 run data from all baselines (H1L1, H1V1, L1V1) with a power-law index $\alpha = 2/3$ and $\pm 1\sigma$ uncertainty level in the red and yellow line.	140
4.21	The cross-correlation spectrum after combining the data from H1L1 baseline in O1 and O2 run, and from all baselines (H1L1, H1V1, L1V1) in O3 run with a power-law index $\alpha = 0$. $\pm 1\sigma$ uncertainty level in shown in red and yellow line [26].	140
4.22	The cross-correlation spectrum after combining the data from H1L1 baseline in O1 and O2 run, and from all baselines (H1L1, H1V1, L1V1) in O3 run with a power-law index $\alpha = 2/3$. $\pm 1\sigma$ uncertainty level in shown in red and yellow line.	141
4.23	Corner plot for the posterior distribution for Ω_{ref} and slope α of a SGWB with a prior uniform in log of Ω_{GW} . The top and right plots show marginalized posterior for Ω_{ref} and α . While the center plot shows the 2D posterior density [26].	141

List of Tables

3.1	Summary of source parameters used to define the distribution of BBHs used in the study. Out of these source parameters only m_1 , m_2 , θ_{jn} and D_L are used to perform the BBH parameter estimation.	70
4.1	Timeline of the O3 data set for aLIGO and AdV detectors. These observation time periods are defined as livetime as both aLIGO and AdV detectors were operating simultaneously.	130
4.2	Table showing the notch frequency list witnessed in both detectors of each baseline during the O3B. Notch frequencies 46-51 Hz during the O3B are due to the active damping mechanical mode around 48 Hz which were observed during the period I was contributing to AdV detector characterization (Figure 4.5 and 4.6).	134
4.3	Isotropic SGWB searches with O3 data for power law $\alpha = 0, 2/3, 3$. For all three baselines (H1L1, H1V1, L1V1), I present the point estimates with $\pm 1\sigma$ uncertainty for cross-correlation estimates \hat{C}_{ij} . Each baseline contains 99% of the sensitivity in frequency band from 20 Hz to respective frequency level $f_{99\%}$. From the table, it is easy to see that H1L1 baseline is the most sensitive towards SGWB searches. In contrast, H1V1 and L1V1 are sensitive to SGWB searches on higher frequencies due to the longer baseline [26].	138
4.4	Isotropic SGWB searches with O1, O2, O3 and combined data using optimal filtering for GWs with various power-law distribution choices $\alpha = 0, 2/3, 3$. The values corresponding to α in O1, O2, O3 and O1+O2+O3 shows the point estimates and the corresponding 1σ error values for the cross-correlation estimates C_{ij} .	138

Abbreviations

GW	G ravitational W ave
GWs	G ravitational W aves
LIGO	L aser I nterferometer G ravitational W ave O bservatory
aLIGO	A dvanced L aser I nterferometer G ravitational W ave O bservatory
AdV	A dvance V irgo
SGWB	S tochastic G ravitational W ave B ackground
SCGWB	S tochastic C osmological G ravitational W ave B ackground
IMR	I nspiral M erger R ingdown
PSD	P ower S pectral D ensity
LVC	L IGO V IRGO C ollaboration
CPSDs	C ross P ower S pectral D ensities
SNR	S ignal-to- N oise R atio
BBH	B inary B lack H ole
BNS	B inary N eutron S tar
CBCs	C ompact B inary C oalescences
PN	P ost- N ewtonian
NR	N umerical R elativistic
NS	N eutron S tar
BH	B lack H ole
O1	F irst O bservation R un
O2	S econd O bservation R un
O3	T hird O bservation R un

Chapter 1

Gravitational waves and detectors

Einstein's theory of general relativity describes how spacetime and mass relate to each other, i.e. mass distorts the spacetime around it and in turn spacetime mandate the flow of matter. The solution of Einstein field equations leads to the concept of gravitational-waves (GWs), which are analogous to the electromagnetic waves. GWs are perturbations (time-varying oscillations) in spacetime metric, which provides a unified description of the geometry of spacetime and gravity itself. These perturbations in the spacetime metric lead to the concept of GWs as a physical entity. In 2015, the first direct detection of GW from the merger of binary black hole (BBH) was observed by LIGO (Laser Interferometer Gravitational-Wave Observatory) and Virgo detectors [10]. After the first detection of BBH merger signal, in August 2017 a binary neutron-star (BNS) merger was detected [13] by these GW detectors, which was followed by a short gamma-ray burst after a few seconds of the merger [14].

Beside these breakthrough detections, the most interesting and outstanding

observations made by current GW detectors came in during their third observation period (O3) where numerous events were detected with different characteristics leading to question our understanding of binary objects and their coalescence processes [25]. The event GW190412 was observed from the merger of two asymmetric black-holes (BH) [22], followed by another event GW190425 [21] from the merger of two neutron-star (NS) with total mass larger than any known BNS. Later, another event GW190814 was detected from the coalescence of a $23M_{\odot}$ black hole and $2.6M_{\odot}$ compact binary object [24].

In this chapter, I provide a short and cursory overview of Einstein's theory of general relativity. Section 1.1 introduces Einstein's field equations followed by generation of GWs in Section 1.2. Section 1.3 focuses on the GW detectors, their layout, functionality and various noise sources which contribute to the limitation's of a GW detector sensitivity. Subsection 4.1 contains the outcome of detector characterization (DetChar) shift during O3 run from January 28 2020, to February 3 2020. Future GW detectors and their scientific reach to detect binary sources are discussed in Section 1.4 with a highlight on GW detector network in Section 1.5.

To understand the concept of GWs, now I will introduce the mathematical formalism of general relativity and GWs.

1.1 General relativity

Einstein field equation shows how spacetime curvature is related to mass-energy and written as [169]

$$G_{\mu\nu} = R^{\mu\nu} - \frac{1}{2}g^{\mu\nu}R = \frac{8\pi G}{c^4}T_{\mu\nu}. \quad (1.1)$$

The term $G_{\mu\nu}$ on the left-hand side of Equation (1.1) is the Einstein tensor, describing the curvature of spacetime. The term in centre expresses Einstein tensor in terms of Ricci tensor (represent the distortion in spacetime), Ricci scalar (trace of Ricci tensor) and metric tensor $g_{\mu\nu}$ describing the geometry of spacetime. In contrast, $T^{\mu\nu}$ is a stress-energy tensor representing the density of mass and energy. G is the Newtonian gravitational constant, and c is the speed of light.

Due to the non-linear behaviour of the Einstein field equation only a few exact solutions are known. Therefore, to study GWs and their properties, it is convenient to follow a natural way by using linearized approximation or weak-field approximation leading to linear equations. Considering Minkowski metric with small perturbations (only lowest order perturbations), with the introduction of perturbations, metric tensor takes the form

$$g_{\mu\nu} = \eta_{\mu\nu} + h_{\mu\nu} \quad | \quad h_{\mu\nu} | \ll 1, \quad (1.2)$$

where μ and $\nu = 0, 1, 2, 3$ and $\eta_{\mu\nu} = \text{diag}(-1, +1, +1, +1)$, $\eta_{\mu\nu}$ is flat Minkowski metric, on the other hand $h_{\mu\nu}$ defines small metric perturbations to the Minkowski metric. The non-zero component of $h_{\mu\nu}$ is assumed to be much less than 1 in order to hold the condition mentioned in Equation (1.2), which is valid only in the linear terms of h . The condition $| h_{\mu\nu} | \ll 1$ is valid only in weak-field regime to the restricted set of co-ordinate transformations (known as gauge-transformations) where Equation (1.2) holds.

Before expanding $h_{\mu\nu}$ to leading order terms, the Christoffel symbol and Ricci tensor in linearized metric perturbation $h_{\mu\nu}$ is

$$\begin{aligned}\Gamma^\mu_{\alpha\beta} &= \frac{1}{2}\eta^{\mu\nu} (h_{\alpha\nu,\beta} + h_{\beta\nu,\alpha} - h_{\alpha\beta,\nu}), \\ &\equiv \frac{1}{2} (h_{\alpha^\mu, \beta} + h_{\beta^\mu, \alpha} - h_{\alpha\beta}{}^{,\mu}),\end{aligned}\tag{1.3}$$

where subscript “,” is used to set off the index that is being used for the derivative of the respective terms. The Equation (1.3) yields Ricci tensor as

$$R_{\mu\nu} = \frac{1}{2} (h_{\mu^\alpha, \nu\alpha} + h_{\nu^\alpha, \mu\alpha} - h_{\mu\nu, \alpha^\alpha} - h_{, \mu\nu}).\tag{1.4}$$

Using Equation (1.4), one can further calculate for Ricci scalar. Now we will define trace-reversed metric $\bar{h} = h_{\mu\nu} - \frac{1}{2}\eta_{\mu\nu}h$ and $trace(h) = \eta^{\mu\nu}h_{\mu\nu}$, which by using Equation (1.1) and (1.4) gives the Einstein field equation in terms of a trace-reversed metric perturbation as given by

$$\bar{h}_{\mu\alpha, \nu}{}^\alpha + \bar{h}_{\nu\alpha, \mu}{}^\alpha - \bar{h}_{\mu\nu, \alpha^\alpha} - \eta_{\mu\nu}\bar{h}_{\alpha\beta,}{}^{\alpha\beta} = \frac{16\pi G}{c^4}T_{\mu\nu}.\tag{1.5}$$

General relativity is a gauge-invariant theory; therefore, slowly varying infinitesimal coordinate transformations $x^\mu \rightarrow x^\mu + \chi^\mu$, where χ^μ is an infinitesimal vector field, are the symmetry of the linearized theory [169]. Consequently, Equation (1.5) can be simplified by making such coordinate transformation. Hence $h_{\mu\nu}$ transforms as

$$\bar{h}'_{\mu\nu} = \bar{h}_{\mu\nu} - \chi_{\nu, \mu} - \chi_{\mu, \nu} + \eta_{\mu\nu}\chi^\alpha{}_{, \alpha},\tag{1.6}$$

where χ can be chosen such that the following condition is satisfied (known as harmonic gauge condition)

$$\bar{h}_{\mu\nu, \nu} = 0. \quad (1.7)$$

Thus, the Einstein field equation in harmonic gauge can be reduced to the simplest form by using Equation (1.5), thus giving

$$-\bar{h}_{\mu\nu, \alpha}{}^{\alpha} = \frac{16\pi G}{c^4} T_{\mu\nu}. \quad (1.8)$$

Equation (1.8) represents the linearized theory of general relativity. This choice of gauge is known as Lorenz-gauge condition and is always feasible. Equation (1.8) is nothing but merely a wave equation of a source with energy-momentum tensor $T_{\mu\nu}$. The benefit of writing Einstein tensor ($G_{\mu\nu}$) in terms of $\bar{h}_{\mu\nu}$ is that it eliminates the trace and restricts the coordinate system to only those who verify Lorenz-gauge condition as given in Equation (1.7). Einstein's field equation in term of the trace-reversed metric is useful and forms the basis for the generation of GWs. By deriving wave equation for the metric perturbations, one can find the solution and representation of GWs.

Since Equation (1.8) represents the wave equation it would be possible to calculate the solution for GW propagation. If we consider the case of vacuum where $T_{\mu\nu} = 0$, Equation (1.8) will reduce to the form $\bar{h}_{\mu\nu, \alpha}{}^{\alpha} = 0$ with the real part of plane wave solution of form

$$\bar{h}_{\mu\nu} = \mathcal{R} [A_{\mu\nu} e^{ik_{\alpha} x^{\alpha}}], \quad (1.9)$$

where $A_{\mu\nu}$ is amplitude of the wave and k_{α} is the wave vector of a wave travelling with the speed of light, $k_{\alpha} k^{\alpha} = 0$. Furthermore, $A_{\mu\nu}$ and k_{α} are orthogonal to each other, therefore $A_{\mu\nu} k^{\nu} = 0$.

To know about how many components of $\bar{h}_{\mu\nu}$ have physical meaning, i.e. the total number of degrees of freedom, we will consider a vacuum spacetime in which $T_{\mu\nu} = 0$ everywhere. It can be shown that in a suitable coordinate system metric perturbations would be spatial and there will be only two independent degrees of freedom that is, trace and spatial components will vanish off $\bar{h} = \bar{h}_{0i} = 0$, and trace-reversed and normal perturbations will become equal $\bar{h}_{\mu\nu} = h_{\mu\nu}$. Hence we will have

$$h_{\mu 0} = 0, \quad h = h^i{}_i = 0, \quad \partial_i h_{ij} = 0. \quad (1.10)$$

Equation (1.10) represents the transverse-traceless (TT) gauge. The TT gauge reduces the degree of freedom of the symmetric matrix $h_{\mu\nu}$. The number of degrees of freedom changes as: starting from elimination of all temporal components which reduces the degree of freedom by four then $\partial_i h_{ij} = 0$ condition eliminates three more degree of freedom (i.e. spatial components are transversal, divergence-free) and one additional degree of freedom eliminated by trace-less condition $h = h^i{}_i = 0$. At last, out of ten, only two degrees of freedom remain, thus, leading to the solution of the wave equation with two degrees of freedom. For a GW travelling in z -direction, $h^T{}_z = 0$, therefore, in TT gauge $h_{\mu\nu} = h_{\mu\nu}^{TT}$ and the remaining components of plane wave solution are

$$\begin{aligned} h_{\mu\nu}^{TT} &= A_{\mu\nu}^{TT} e^{ik^\alpha x_\alpha}, \\ &= A_{\mu\nu}^{TT} \cos(\omega(t - z)). \end{aligned} \quad (1.11)$$

The wave vector with components $k = (\omega/c, \vec{\Omega})$ specifies the frequency and direction of propagation of a GW. From Equation (1.10) and (1.11), it can be shown that only those components of $h_{\mu\nu}^{TT}$ survive which are perpendicular to the direction of propagation of GW i.e. $A_{\mu\nu} k^\nu = 0$. Thus the amplitude of GW is

$$A_{\mu\nu}^{TT} = \begin{bmatrix} 0 & 0 & 0 & 0 \\ 0 & h_+ & h_\times & 0 \\ 0 & h_\times & -h_+ & 0 \\ 0 & 0 & 0 & 0 \end{bmatrix}, \quad (1.12)$$

where h_+ and h_\times are the two polarizations of a GW corresponding to two degrees of freedom in the linearized approximation of general relativity, known as plus (+) and cross (\times) polarization respectively. Using Equation (1.11) and (1.12), one can re-write the plane wave solution as

$$\begin{aligned} h_{ij}^{TT} &= h_+ e_{ij}^+(\hat{z}) + h_\times e_{ij}^\times(\hat{z}), \\ A_{ij}^{TT} &= h_+ e_{ij}^+ + h_\times e_{ij}^\times, \end{aligned} \quad (1.13)$$

where e^+ and e^\times are the polarization tensors for + and \times polarization respectively and are given by

$$e_{ij}^+ = \begin{bmatrix} 0 & 0 & 0 & 0 \\ 0 & 1 & 0 & 0 \\ 0 & 0 & -1 & 0 \\ 0 & 0 & 0 & 0 \end{bmatrix}, \quad e_{ij}^\times = \begin{bmatrix} 0 & 0 & 0 & 0 \\ 0 & 0 & 1 & 0 \\ 0 & 1 & 0 & 0 \\ 0 & 0 & 0 & 0 \end{bmatrix}. \quad (1.14)$$

Here it is assumed that the GW propagates along the z -axis. Because h_{ij}^{TT} is transverse, x - y plane demonstrates the effect of these two polarizations. The plus and cross polarizations cause deformation of the ring of particles, as shown in Figure 1.1, hence leading to their nomenclature.

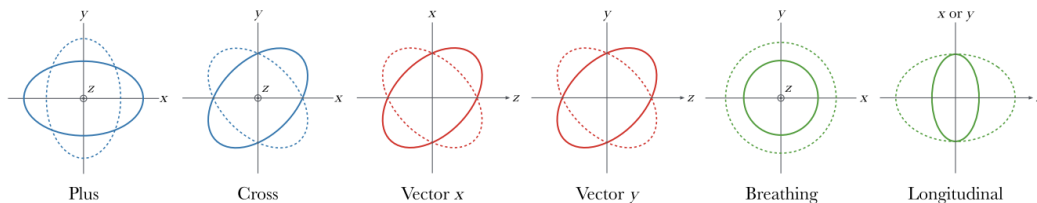


FIGURE 1.1: Deformation of the ring of particles propagating along z direction. GR allow two modes of tensor polarization (plus and cross), alternative or modified theories of GR allows two vector polarizations (x and y) and two scalar polarizations (breathing and longitudinal) (Figure from [64]).

1.2 Generation of GWs

Focusing back on how GWs are generated and characterized by their time-varying mass quadrupole moment we can follow Equation (1.8) with appropriate boundary conditions at the lowest order in terms of reduced quadrupole moment. Thus, from the wave equation one obtains the following GW amplitude

$$h_{ij}^{TT} = \frac{2G}{c^4 r} \ddot{\mathcal{I}}_{ij}, \quad (1.15)$$

where $i, j = 1, 2, 3$ and r is distance between source and observer. A factor of G/c^4 shows that, in general, highly energetic objects are required to produce the GWs, which can then be observed by GW detectors within their sensitivity range and observational frequency band. $\ddot{\mathcal{I}}_{ij}$ is the spatial traceless mass quadrupole moment (each dot represents derivative with respect to time) and can be written as time-varying mass density ρ

$$\mathcal{I}_{ij} = \int d^3x \rho \left(x_i x_j - \frac{1}{3} r^2 \delta_{ij} \right). \quad (1.16)$$

To get a proper understanding, let us take an example of a binary system with masses m_1 and m_2 respectively, orbiting around each other with orbital frequency ω . If r gives the distance between these two masses, as orbital energy starts to

radiate, the distance r between these two masses starts to reduce leading to an increase in the frequency and amplitude of radiation emitted during the process. As the distance between these two masses decreases further, the orbital frequency increases and the whole system starts to radiate at much higher frequencies, causing them to merge and form a new compact object. The radiation emitted during this process can be measured with GW detectors.

1.3 Gravitational wave detectors

A GW propagation through a GW detector causes the compression and expansion between test masses (as discussed in Section 1.1 and 1.2), and can be measured by observing these infinitesimal changes at a proper distance. These relative variations are proportional to the amplitude of GW.

In this section, I will discuss currently operational ground-based GW detectors being used to observe these changes as an influence of GWs. Besides that, I will also focus on proposed future generation ground-based GW detectors. The detection of GWs via these detectors is characterized by detector's intrinsic characteristics, i.e. how sensitive is a detector to observe these signals and in what frequency range a detector is observing these signals. Since there are various technologies for the detection of GWs, hence, I will discuss only the currently being used laser interferometers.

1.3.1 Interferometer detector

Laser interferometers are the resultant of a long quest to detect GW signals. Currently, there are various ground-based GW detectors which are operating namely, Advanced LIGO (aLIGO) [37] in the United States of America (USA), Advanced Virgo (AdV) [28] in Italy, GEO600 [171] in Germany (a

high-frequency range detector). Beside these GW detectors, we have recently constructed Kamioka Gravitational Wave Detector (KARGA) [33], a Japanese initiative to build an advanced GW detector located underground to minimize the contribution of low-frequency noise from various channels using cryogenics, which started its science observation run on February 25, 2020. On the other hand, a new GW detector LIGO-India [157], a joint proposal of India-USA to build future LIGO GW detector in India, is currently under construction. All these detectors use laser interferometric technologies to detect GWs by observing the relative motion of their test masses.

After following continuous upgrades to increase the detection sensitivity, aLIGO started its first observation run (O1) in September 2015, days before the GW150914 event detection. In contrast, AdV joined in August 2017 during aLIGO's second observation run (O2) to take part in joint observations. Followed by another year of continuous upgrades to further increase their sensitivity, aLIGO and AdV have completed their third observation run (O3) in April 2020, making several tens of observations of different types of coalescing binaries [6, 25].

For the detection of GWs, the Michelson interferometer is an ideal instrument. The basic principle is to send the light from a laser source towards a beam splitter splitting the beam into two parts. One half of the beam is transmitted towards the end mirror of one arm and the second half is reflected at 90° (with respect to the transmitted beam) and directed towards another end mirror (see Figure 1.2 for AdV detector layout). In this case, the beam reflects multiple times between the two mirrors to enhance the interaction with a GW. Since a GW detector operates at the dark fringe, both beams interfere destructively towards the output port of the interferometer. In contrast, since a GW signal has opposite sign in the two arms, it interferes constructively towards the interferometer output. The photodetector effectively measures the phase difference as given by

$$\begin{aligned}\Delta\phi &= \frac{2\pi}{\lambda}\Delta L, \\ &= \frac{2\pi}{\lambda}(2Lh),\end{aligned}\tag{1.17}$$

where $\Delta\phi$ is the phase difference due to the GW passing through the detector, λ is the wavelength of the input laser beam and $\Delta L = 0.5 \times L \times h$ is the optical path difference. L gives the separation between two test masses, and h is the amplitude of a GW known as *strain*. The quantity h is given by

$$h = \frac{2GM}{c^2 D} \left(\frac{v}{c}\right)^2.\tag{1.18}$$

where G is gravitational constant, M is mass of an object moving at speed v and observed at distance D . For a GW passing through a GW detector, the measured strain h would be

$$h = \frac{\Delta L}{L}.\tag{1.19}$$

To further understand how a GW detector detects GW signals, I will consider AdV detector for a detailed discussion with the detector layout.

1.3.2 AdV interferometer

AdV [28] is a second-generation (an Italian-French GW detector upgraded from main Virgo detector in 2017) GW detector, with the increased sensitivity, aimed for the direct detection of GWs from binary coalescences. The Virgo [27] detector is a Michelson interferometer consisting of two perpendicular arms, each 3 km long, built at Cascina in Pisa (Italy). AdV commissioning started in 2012

and ended in 2016. AdV started its first observation run on August 1, 2017 with a strain sensitivity level around $10^{-23} (\sqrt{Hz})^{-1}$. During its 20 days of observation run in 2017, AdV contributed to sky localization of the GW signal from the BBH and BNS merger alongside the aLIGO detectors [13].

Now, I will discuss the AdV configuration and how a GW detector works towards the GW signal detection.

1.3.2.1 AdV detector layout

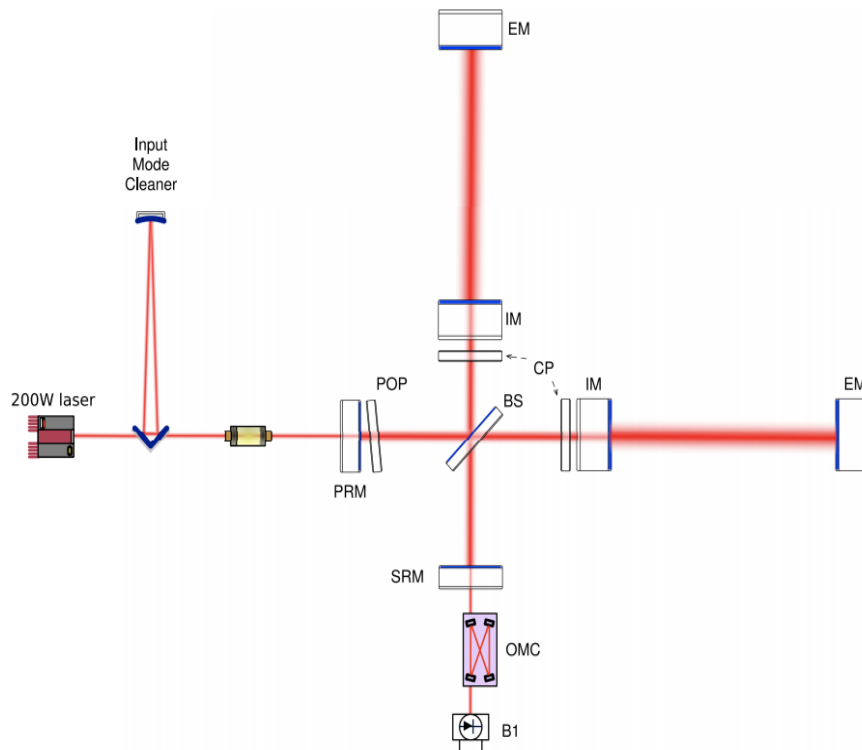


FIGURE 1.2: Plot showing the structural Layout of AdV interferometer. The arm cavity of 3km length is formed by Input Mirror (IM) and End Mirror (EM) in each perpendicular arm. These mirrors are also known as the test masses. Recycling cavities of 12m length lie at the centre of the interferometer. (Figure from [28]).

AdV detector is a dual recycled Michelson interferometer with Fabry-Perot resonant arm cavities to improve the sensitivity towards GWs detection. A

schematic layout of AdV is shown in Figure 1.2. The arm cavities (Fabry-Perot cavities) of AdV are bi-concave with a concave radius of curvature a bit larger than half the arm cavity length to ensure the stability. The main reason behind this is, first, to increase the beam size at mirrors, and then reducing the contribution of mirror coating thermal noise. On the other hand, the second one is to reduce the alignment instability induced by radiation pressure. The two arms perpendicular to each other are formed by input mirror/mass (IM) and end mirror (EM). A beam splitter (BS) is placed at 45° to divide the incident laser beam into two halves. AdV has been using a power-recycling cavity to enhance laser power inside the interferometer, and will use signal recycling in the next observation run to improve its GW response. Signal recycling also makes it possible to tune the sensitivity curve and optimize the detector for different astrophysical source detection. AdV requires a high power continuous wave laser stabilized in frequency, intensity and beam pointing to operate, which is provided by $Nd : YVO_4$ (Neodymium doped Yttrium Orthovanadate) crystals. Thus, the laser can achieve an output power of $P_{out} \sim 200W$. High power is required to reduce shot-noise limitations, in contrast, stabilization takes care of technical noise such that there would be no additional source of a noise coming from the laser itself, affecting the detection of a GW signal. With the increase in laser power, it was necessary to install larger test masses ($m \simeq 42kg$) to reduce the impact of radiation pressure and multiple noise source fluctuations (Subsection 1.3.3).

The interferometer is operated such that upon recombination of the two beams at BS coming from the arm cavities, no light goes to the output unless due to noise or a GW signal. A partial reflective mirror (PRM) is used between the laser source and BS to ensure that the light coming back from interferometer and reflected by PRM is in phase with the incident laser beam, thus enhancing the power inside the arm cavities. The input laser beam is filtered by a triangular cavity known as Input mode cleaner (IMC) placed between PRM and the laser

source. Another cavity output mode cleaner (OMC) is used before photodetector to reject the unwanted component of laser light before signal detection.

Whenever there is a GW signal observed by the detector, the lengths of two arms change with respect to each other leading to a phase difference between the laser travelling in the two arm cavities. Consequently, the beam which carries this differential change in arm length is observed by the photodetector (B1 as showed in Figure 1.2). Together with the signal and noise contributions, a small fraction of the laser beam is allowed to leak into the dark port to ensure a linear dependence of detector output on GW signals and to help overcome noise from the photodetector readout.

To optimize the AdV for better sensitivity, AdV is under continuous monitoring with the help of various sensors, e.g. seismometers, magnetometers acoustic probes, thermometer and other various sensors to measure changes in surroundings of the detector. The data from these sensors are recorded by a monitoring system with the detector's output, which helps to study and distinguish between noise and a GW signal.

AdV has its limitations towards detection of GWs due to the presence of noise from different sources, which I discuss in the following.

1.3.3 Noise contribution to sensitivity

A GW detector detects the phase difference produced by a GW signal while passing through the detector. Equation (1.17) gives the estimates for phase difference, which is of order of $\sim 10^{-13}$ using GW amplitude $h \simeq 10^{-23}$, length of arms $L = 3\text{km}$ and laser wavelength $\lambda = 1064\text{nm}$. For a GW detector to have the sensitivity to measure a signal as weak as of order $\leq 10^{-23}$, it needs to be isolated from the noise sources. Here, I will discuss a few important noise sources which contribute to the detector's overall noise budget.

The measurement of a GW detector sensitivity towards GWs is given by its power spectral density (PSD). PSD is commonly used to represent noise spectra. In contrast to Fourier transforms, it converges for stationary noise. Thus the total output of a GW detector $s(t)$ is the sum of detectors intrinsic noise $n(t)$ and the GW strain $h(t)$ at any given time t

$$s(t) = n(t) + h(t). \quad (1.20)$$

For simplicity, assuming that the noise of a detector is stationary, hence it can be characterized by an autocorrelation of the form

$$C_{ij}(\tau) = \langle n(t_i)n(t_j) \rangle, \quad (1.21)$$

where $\langle \dots \rangle$ denotes the time average for different noise realizations of detector's stationary noise. Since the noise is stationary, correlation $C_{ij}(\tau)$ depends only upon $\tau = |t_i - t_j|$. In reality, this is not true. Noise in a GW detector is not stationary, but we will use this assumption in the following. Consequently, a one-sided power spectral density (PSD) $S_n(f)$ for a GW detector can be defined as

$$S_n = \frac{1}{2} \int_{-\infty}^{\infty} C_{ij}(\tau) e^{2\pi i f \tau} d\tau, \quad (1.22)$$

S_n has units of inverse of frequency times the units of $C_{ij}(\tau)$. Since detector output is a real-valued quantity, it follows: $\tilde{h}(-f) = \tilde{h}^*(f)$ and $\tilde{n}(-f) = \tilde{n}^*(f)$, where terms with “ \sim ” sign denote a Fourier amplitude, consequently, $S_n(f) = S_n(-f)$. S_n is even, and it is sufficient to consider positive frequencies defining the one-sided PSD. Its relation to the Fourier amplitudes is

$$\langle \tilde{n}(f)\tilde{n}^*(f') \rangle = \frac{1}{2}S_n(f)\delta(f - f'). \quad (1.23)$$

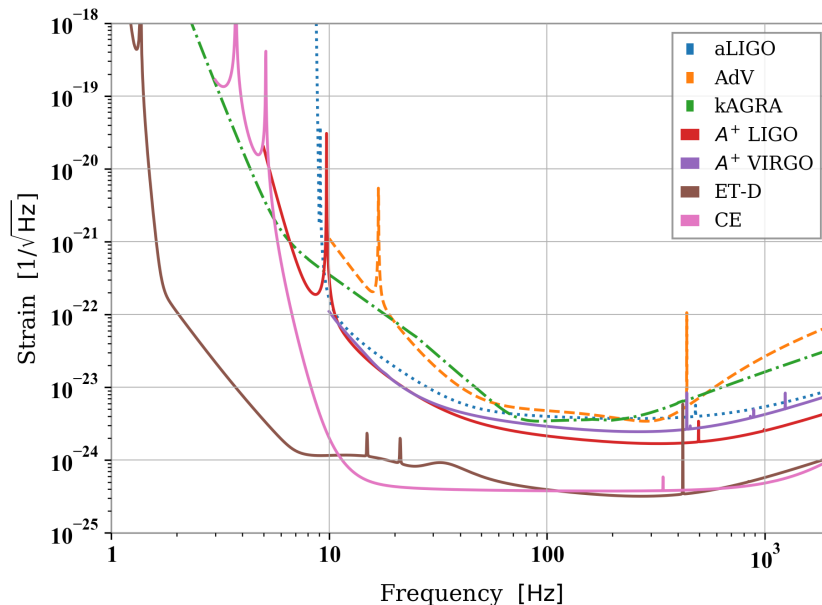


FIGURE 1.3: Plot showing the sensitivity curve for aLIGO and AdV GW detectors with anticipated sensitivity curves for future GW detectors in terms of strain sensitivity. Where A⁺ LIGO corresponds to future aLIGO after upgrades, A⁺ VIRGO is upgraded version of AdV. In contrast, ET-D represents the sensitivity curve for Einstein Telescope (ET) with xylophone configuration, and CE is the overall sensitivity curve for Cosmic Explorer (CE).

The detector's noise contribution can be categorized in two ways: instrumental noise and environmental noise. The first category includes the noise coming from the types of equipment used for detector construction, and the second contribution is due to detector location and infrastructure. There are various types of noises characterized by different spectra. In the low-frequency regime <50 Hz, seismic noise and Newtonian noise, among many others, dominate. In the frequency band 50 Hz - 100 Hz, thermal noise due to fluctuations in mirror coating set limits on the sensitivity and above 200 Hz laser shot noise dominates. Some of the fundamental noise sources which determine the sensitivity of a GW detector are explained in the following:

Newtonian noise: Newtonian noise contribution can come from various fields in the environment (seismic, acoustic, temperature, humidity etc.), and are associated with a GW detector through only one coupling mechanism, namely the generation of gravitational fluctuations leading to test masses movements in the GW detector [78]. Newtonian noise dominates in the lower frequencies of AdV detector as can be seen in Figure 1.4. [90] discusses the handling of Newtonian noise at low frequencies in ground-based GW detectors.

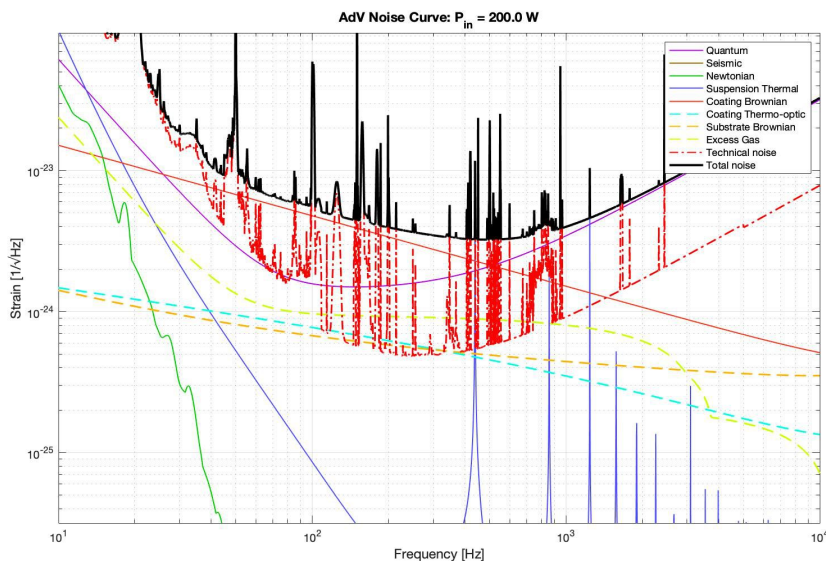


FIGURE 1.4: Plot showing the contribution of different noise channels to AdV noise budget and overall sensitivity curve of AdV detector. On frequency scale, one can see the frequency band in which these noise contributions dominate, and limit the detector sensitivity. The plot has been reproduced using for an output power source of 200W using gwinc code [2].

Quantum noise: Quantum Noise contribution to intrinsic GW detector noise comes from the quantum fluctuations of the laser field. The relevant quantum fluctuations do not come from the laser source; if they do so, the contribution would be negligibly small. Contrarily, these fluctuations originate from the dark-port in the form of vacuum fields contributing to the GW detector output. They are typically divided into shot noise and radiation-pressure noise, where the latter is a consequence of an interaction between the high-power laser field and the

suspended test masses. The quantum fluctuations contribution to a GW detector can be reduced by increasing the detector's arm length using Fabry-Perot cavities to improve the overall response of a GW detector to GWs detection. These improvements further lower all noise sources that contribute to the detector noise budget. More detailed information can be found in [48].

Thermal noise: Thermal noise occurs due to thermal fluctuations in the material used for mirror coating and suspension fibres. There are two ways to follow to reduce the thermal noise contribution. The first one is to lower the temperature which can be achieved by using cryogenics to cool down the thermal vibrations in the test masses and the second one is to develop materials and coating deposition techniques to lower dissipation under deformation, which lowers thermal noise due to the fluctuation-dissipation theorem.

Now, I will present the results from the detector characterization of AdV detector, a part of the research work carried out during the research period.

1.4 Future generation GW Detectors

GW detectors aLIGO and AdV finished their O3 run with several tens of binary merger signals [6, 25]. However, there is still a vast spectrum of GW physics unexplored both in astrophysics and cosmology. In the future, the goal would be to exploit this vast untouched spectrum. The shortcomings of second-generation GW detectors, either in observation of continuous (frequent observations) GW signals, not being sensitive enough in 1 Hz - 20 Hz frequency regime, and inability to measure the polarizations of a GW signal leads to the idea of future generation GW detectors. The future generation GW detectors will overcome these limitations and increase the scientific potential with an improvement in their sensitivity level. Even if current GW detectors run for a longer duration, there would be a linear increase in number of observations, but all detected sources would be in

the local universe with a low signal-to-noise ratio (SNR), which again limits the scientific goal.

Contrary to this, if the sensitivity of a detector can be increased, the detection horizon will also increase to higher redshift values. Therefore, being sensitive in the lower frequency regime from 2 Hz to higher frequencies of a few kHz, future generation GW detectors will open a new window for binary sources and their detection, including the inspiral, the merger, and the ringdown process, ranging from stellar to intermediate masses and other compelling GW signals either of astrophysical or cosmological origin [61]. [88] provides insight into the metric of future generation GW detectors, thus pointing out how to maximize the scientific scope [118] of these detectors.

For accomplishing these goals, two next-generation ground-based GW detectors ET and CE have already been proposed. These future GW detectors (also referred to as third-generation or 3G detectors) will allow us to explore the dark universe up to high redshift. The main benefits of the third-generation GW detectors over current ones are frequent detection of binary sources and detection of signals from rare events (core-collapse supernovae, magnetars etc. . .) and many other phenomena which radiate GWs. With these detectors, a larger part of the universe would be within the observable range up to high redshift values $z \geq 10$. The progress in different areas of the detector physics will also play an essential role in determining their scientific potential. Focusing back on third-generation detectors, I will discuss the two proposed third-generation detectors ET and CE.

1.4.1 Cosmic Explorer

Cosmic Explorer (CE) [12, 138] is the US proposed third-generation ground-based GW detector based on current aLIGO, and its future successor A⁺. CE consists of an L-shaped detector like aLIGO with an increase in arm length from

4km to 40 km to achieve a sensitivity level enhanced by a factor of 10 and more (see Figure 1.5). CE is envisaged to be a two-stage detector program. In stage one, known as CE1 (the targeted operation is in the 2030s), there would be upgrades in technologies of A⁺ and scaling of detector arms (up to 40 km) close to the length of GWs at kHz frequencies. With this colossal increase in the detector’s arm length, all noise contributions will change (i.e. reduction in the noise budget), thus leading to an improvement in the CE sensitivity. [12] provides more detailed information about the contribution of noise sources and the sensitivity of CE. On the other hand, the stage two of CE is known as CE2, which will become operational in the 2040s. CE will exploit the scientific potential with the full upgraded facility, i.e., new laser sources, changed test masses, mirror and coating material, reduction of thermal noise through cryogenics, and many more.

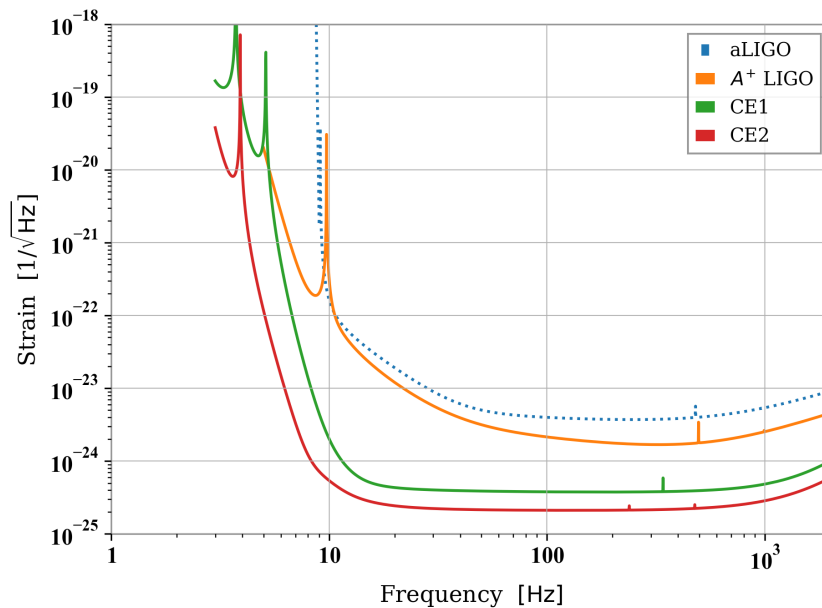


FIGURE 1.5: The plot shows the anticipated sensitivity curve for future generation CE detector during stage 1(CE1) and stage 2 (CE2) with the sensitivity curve of A⁺ and aLIGO GW detector. The sensitivity curve for CE1 and CE2 are from [5].

With these advancements, CE will provide a unique opportunity to observe

GW sources throughout the universe with remarkable accuracy. In an observational frequency band from 5 Hz to 4 kHz, CE would detect sources up to cosmological scale (up to higher redshift $z \sim 20$) [79] and all those sources which have not been detected yet or are barely impossible to detect with aLIGO. Detection of $10^5 - 10^6$ binaries would significantly impact our understanding of GWs, their sources, history, and evolution of the universe until present times.

1.4.2 Einstein Telescope

Einstein Telescope (ET) [131] is a European proposed third-generation GW observatory to increase the scientific goal of GW physics and multi-messenger astronomy. ET will provide with an improvement in the strain sensitivity by an order of 10 times relative to current GW detectors [92], thus, increasing the observational frequency band towards lower frequencies around ~ 2 Hz (see Figure 1.3). This goal of ET to push sensitivity down to 2 Hz will make it the most sensitive ground-based future GW detector.

The ET observatory is envisaged to be a triangular shape Michelson interferometer. The triangular shape consists of three V-shaped Michelson interferometers with 60° opening to each other and a length of 10 km each (see Figure 1.6). To achieve the sensitivity level in the 2 Hz - 10 Hz frequency range is not an easy task as many factors can cause challenges in the lower frequency range (see Subsection 1.3.3). Hence, a xylophone configuration [93] has been proposed. In this configuration, each V-shape detector splits into two interferometers. These two interferometers are installed in a V-shape triangle, i.e., one interferometer with high power having sensitivity at high frequencies (at room temperature) and one with low power having sensitivity at lower frequencies (see Figure 1.6). These triangles are then placed underground to reduce the contribution from various noise sources, making it feasible to achieve ET's anticipated sensitivity level.

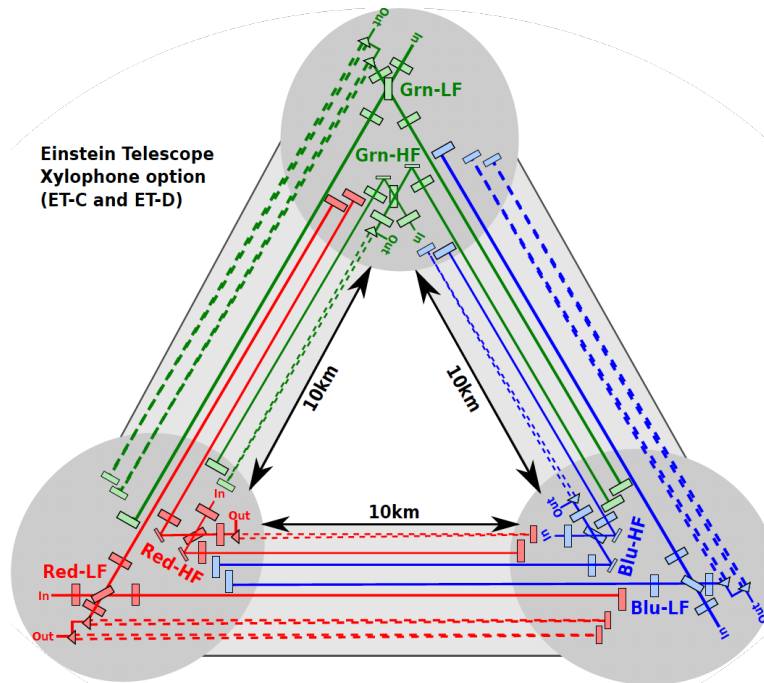


FIGURE 1.6: Einstein Telescope (ET) proposed a triangular shape configuration with high and low frequency interferometers placed at 60° with respect to each other, forming a full ET GW detector. The shape, which is considered to be the final shape till now, is known as Xylophone configuration (ET-D) shown with another proposed ET-C configuration (Figure from [94]). Solid lines represents the original laser beam and dashed lines represent a squeezed laser beam.

For achieving this utmost sensitivity level as low as 2 Hz in frequency, ET will require 500 W of input laser power with 3 MW of arm cavity power in the high-frequency interferometer and 3 W of input laser power and 18 kW of arm cavity power with cryogenic technology in low-frequency interferometers [94].

Since seismic noise is coupled to a GW detector's arm through mechanical suspension and seismic isolation system, it contributes to noise in lower frequencies (see Figure 1.7), reduced by using enhanced seismic isolation methods. Therefore, to overcome the seismic noise, ET is proposed to be built underground [94]. On the other hand, in frequency band 2 Hz - 10 Hz, thermal noise from suspensions and mirrors is another important noise contribution, which cannot be easily mitigated. For this purpose, cryogenics technologies have been proposed to

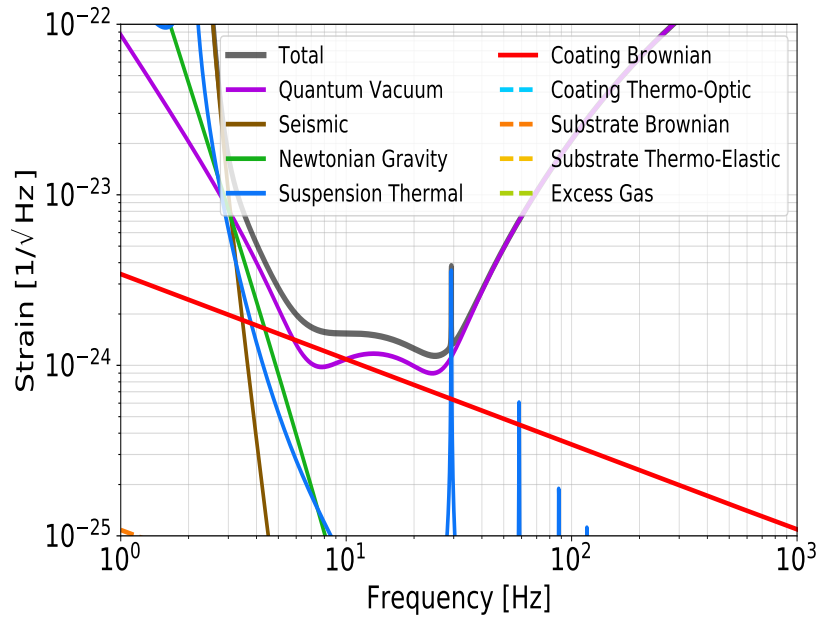


FIGURE 1.7: Plot showing the anticipated noise budget curve for low frequency ET detector. Different noise sources contribute to the sensitivity of the ET detector at different frequency ranges.

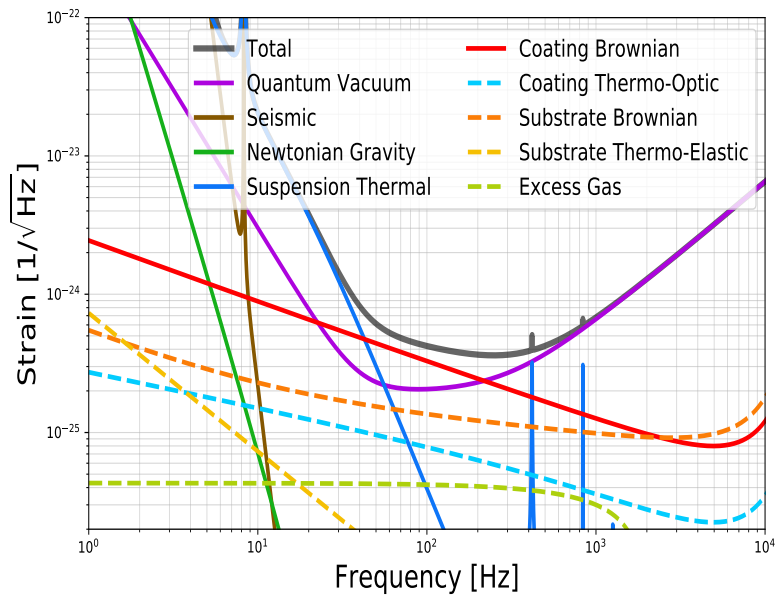


FIGURE 1.8: Anticipated noise budget curve showing the contribution towards the high frequency ET detector from various noise sources.

be used in the low-frequency detector to reduce the thermal noise contribution, leading to a more sensitive ET detector. Such cryogenics are already being used by the KAGRA GW detector to overcome the thermal noise challenges.

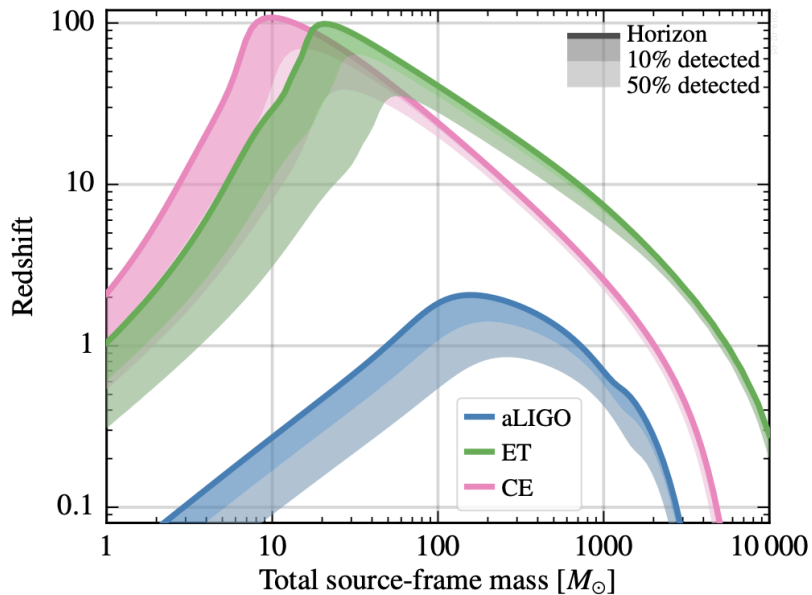


FIGURE 1.9: Plot showing the astrophysical reach of non-spinning equal mass binaries accessible with aLIGO, ET, and CE GW detectors (figure from [118]).

1.4.3 GW source for 3G detectors

Both ET and CE are ground-based GW detectors, hence they will have similar GW sources as that of aLIGO and AdV, namely NS-NS, BH-BH, NS-BH binary mergers. Because these third-generation GW detectors are sensitive in low-frequency regime 2 Hz - 10 Hz, binary sources would be long-lived, even a day-long or more. Besides these common sources, there would be the detection of intermediate-mass BH binaries (IMBHB) within the mass range of $10^2 M_\odot - 10^3 M_\odot$ as shown in Figure 1.9. Even if the cutoff is placed around 2 Hz - 10 Hz on lower frequencies, sky localization of GW sources and parameter estimation

accuracy will increase from current GW detectors. For different type of sources accessible with these detectors see [61, 47] and [118].

1.5 Global network of GW detectors

For a confident GW signal detection, the signal must be detected in at least two or more GW detectors. Consequently, such a GW signal would be coincident in all detectors. GW detectors are omnidirectional, which makes them sensitive to detect signals from all over the sky. A GW detector network (two or more) is required to locate the GW signal with the triangulation method. Such a GW detector network will also help to identify the false triggers caused by individual detector noise. At the moment, we have a network of four main GW detectors, namely: two aLIGO detectors, AdV, and KAGRA. Besides these, the LIGO-India detector is under construction. Whenever it joins, it will increase the effective baseline of detectors in the network, increasing the capability to locate the GW sources over the sky and further improving the SCGWB searches.

Chapter 2

Stochastic Gravitational Wave

Background : sources and detection

The GW signals fall under different classes, namely: inspiral, burst, periodic, and stochastic. Inspirational GW signals are produced by compact binary coalescences (CBC) and are well-understood sources of GWs, on the other hand, a burst signal is a short signal with a definite time domain signature. A periodic signal represents the continuous wave (longer duration than the observation period of a GW detector) of gravitational radiation with a distinct signature in the frequency domain. In contrast, the stochastic background is different from the classes mentioned above. The main characteristics of a stochastic background are determined by its time and frequency domain second-order moments like PSDs and CPSDs.

The detection of GW signals from several binary coalescences (e.g. BBH, BNS, NS-BH) can reveal an unknown population of binary objects, further providing us with information on spacetime dynamics, i.e., how different kind of

observations can help us to test theories of general relativity. Since the merger's arrival time from the coalescing binaries is random; consequently the resultant GW signal detected by a GW detector would be random (in the observation period). A huge number of such randomly distributed GW signals is an ideal example of the stochastic background of gravitational radiation.

In principle, a stochastic GW background (SGWB) is the superposition of numerous GW signals (signals overlapping in time and frequency domain) produced by a large number of weak, independent, resolved, and unresolved sources (sources which are unfeasible to identify individually). Such GW sources contributing to the SGWB include CBC, white dwarfs, core-collapse supernovae, stellar core collapse, magnetars [135], first-order phase transitions [103, 102], cosmic strings [161, 75, 155, 125], primordial black holes (PBH), and GWs produced during inflation from quantum fluctuations [160, 80, 87] and many other phenomena [56, 64]. These sources can differ in their evolution and their general characteristics of GWs produced by them. Depending on GW sources and characteristics of GWs emitted by these sources, the SGWB can be classified into two types: astrophysical and cosmological SGWB. Here it is of great importance to clarify the meaning of weak and unresolved sources. These GW sources are unresolved, not due to the properties of the GW background but due to the detectors total observation period and limit in the sensitivity to detect these signals. In contrast, a signal is resolvable only when separated and detected individually, i.e. if GW signals have sufficiently high SNR to be detected with negligible influence on their parameter estimation from other signals potentially present at the same time. Therefore, it becomes crucial to characterize all possible GW sources to achieve a better understanding of the SGWB.

The detection of an SGWB would be a breakthrough discovery. An SGWB provides a direct window to study the astrophysical sources from the beginning of the stellar activity, their properties and the early universe processes, which, on

the other hand, are impossible to probe by any other means. The GW detectors designed to observe GW sources can also detect SGWB. An SGWB detection depends on the detector's operational frequency band, observation period, and the sensitivity to detect GW signals from different sources over the cosmological distances. Even if a detector detects an SGWB from the early universe, it will lead to the question, how we would know if the detected signal is an SGWB (either of astrophysical or cosmological origin)? If it is, then what are the data techniques required to search for such crucial signals before one starts to study these signals and their associated properties?

This chapter focuses on various astrophysical and cosmological sources contributing to the SGWB. Section 2.1 provides a brief introduction to the SGWB in terms of energy density. The contribution of astrophysical SGWB from various binaries is discussed in Section 2.2. The cosmological SGWB (SCGWB) from the various early universe processes is discussed in Section 2.3.

2.1 SGWB from different source

The output of a GW detector in the presence of a GW signal can be divided into two parts: a resolved part of the signal and what remains after removing the resolved part of the signal. The latter part contributes to the combination of unresolved signals and a contribution from the cosmological background in addition to the detector's noise. The overall data of a GW detector in the presence of a GW signal can be decomposed as follows

$$\textit{output data} = \textit{signal} + \textit{noise}$$

$$\textit{signal} = \textit{astrophysical signal} + \textit{cosmological background}$$

$$\textit{astrophysical signal} = \textit{resolved} + \textit{unresolved}$$

$$\textit{cosmological background} = \textit{primordial universe signal}$$

SGWB = unresolved astrophysical background + cosmological background

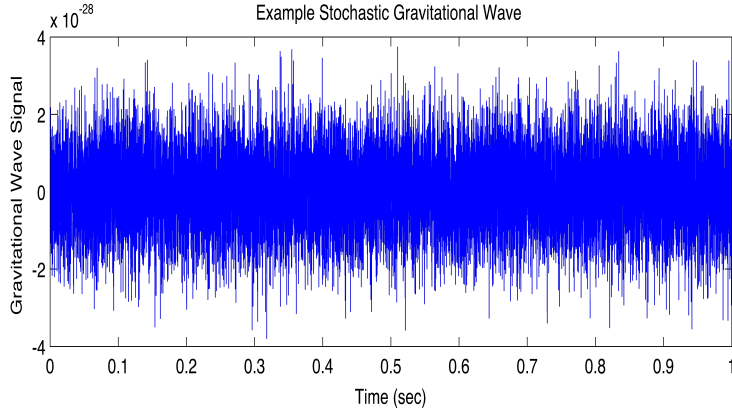


FIGURE 2.1: A representation of how an SGWB might look like in an observed signal by a GW detector (Figure from [7]).

The spectral shape of an SGWB is the key to distinguish it in the GW detector data as different processes can give rise to different spectral shapes. An SGWB is expressed in terms of a dimensionless energy density quantity

$$\Omega_{GW} = \frac{1}{\rho_c} \frac{d\rho_{GW}}{d\ln f}, \quad (2.1)$$

where $\rho_c = \frac{3H_0^2 c^2}{8\pi G}$ represents the critical energy density of the universe, and $d\rho_{GW}/d\ln f$ is the GW energy density per logarithmic frequency bin. The spectral shape of an SGWB carries information about sources; therefore, accurate modeling of the spectral shape can help in unveiling the properties of sources.

The signal from unresolved sources contributes to the unresolved background and would be a random signal in the detector data. Figure 2.1 provides a representation of how an SGWB looks in a GW detector data.

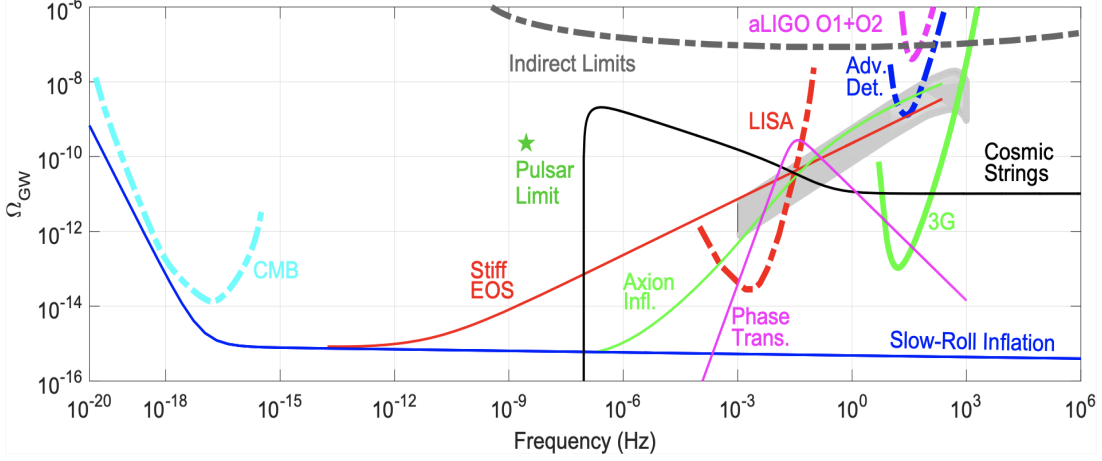


FIGURE 2.2: Plot showing the SGWB spectra from the various cosmological sources and previous limits from aLIGO detector, constraints based on the CMB observations and the pulsar time array (PTA). In addition to the SGWB spectra, the anticipated sensitivity curves for third-generation and LISA detector is shown. The grey band shows the expected SGWB from astrophysical sources (figure from [118]).

2.2 Astrophysical SGWB

An astrophysical SGWB can be characterized by the distribution of astrophysical sources: homogeneous, isotropic, anisotropic and Gaussian. From the beginning of the structure formation (stars, galaxies and other astrophysical objects), astrophysical sources emit GWs through various stellar processes. As mentioned earlier, the superposition of a large number of resolved and unresolved signals from astrophysical sources contributes to the astrophysical SGWB mainly from the periodically long-lived compact binary objects, and the short-lived burst sources (coalescing BBH, BNS, NS-BH which are the dominant sources in ground-based GW detectors). Apart from these binaries, there are SNe explosion, white dwarf binaries, oscillation modes, and instabilities in the rotating star, which can contribute to an SGWB [135].

From the Newtonian analysis, the energy density spectrum of binary objects at low frequencies is defined by the power-law $\Omega_{\text{GW}} \propto \Omega_{\alpha} f^{\alpha}$ with power-law index $\alpha = 2/3$. The amplitude term Ω_{α} is calculated from CBC properties such

as individual masses of binary objects, coalescence rates and their evolution. Such power laws are widely used in SGWB searches and their parameter estimation.

Starting from Phinney's theorem [129], it would be easy to demonstrate how the spectral energy density varies with the redshift evolution of GW sources over the cosmological scales

$$\Omega_{GW}(f) = \frac{1}{\rho_c} \int_{z_{min}}^{z_{max}} \frac{N(z)}{(1+z)} \left(\frac{dE_{GW}}{d \ln f_s} \right) \Big|_{f_s=f(1+z)} dz, \quad (2.2)$$

where $N(z)$ gives the number density of binary events occurring at redshift z , the factor $1/(1+z)$ accounts for redshift in the energy emitted by the coalescing binary objects, $f_s = f(1+z)$ is the frequency of GW in binary source cosmic frame and related to frequency f observed by the GW detectors. $\frac{dE_{GW}}{d \ln f_s}$ is the gravitational energy emitted by an individual binary object in the frequency range f_s and $f_s + df_s$. The limits of integration are set from the beginning of structure formation z_* over redshift z and the emission frequency range (minimum and maximum) in binary source frame frequency given as $z_{min} = \max(0, f_s \text{ min}/(f - 1))$ and $z_{max} = \min(z_*, f_s \text{ max}/(f - 1))$.

For an astrophysical SGWB, the energy density parameter can be obtained in terms of a differential binary event rate and the comoving distance $r_z = D_L/(1+z)$ (D_L is the luminosity distance), by using $\frac{d\dot{N}}{dz} = N(z) c 4\pi r_z^2$, we would have [172, 173]

$$\Omega_{GW}(f) = \frac{f}{\rho_c c} \int_{z_{min}}^{z_{max}} \frac{1}{4\pi r_z^2} \left(\frac{dE_{GW}}{df_s} \right) \Big|_{f_s=f(1+z)} \frac{d\dot{N}}{dz} dz. \quad (2.3)$$

The product of the first two terms inside the integral is the energy flux (spectrum, emitted by a single source) per unit frequency given by

$$\frac{dE_{GW}}{dSdf} = \frac{1}{4\pi r_z^2} \left(\frac{dE_{GW}}{df_s} \right) \Big|_{f_s=f(1+z)}, \quad (2.4)$$

where dS defines the integration over solid angle for the specific intensity of flux at redshift z , and the last term $\frac{d\dot{N}}{dz}$ is the rate of binary events at redshift z per unit comoving volume per unit cosmic time. Therefore the number of events occurring in this particular regime can be written in term of rate density per unit volume $R(z)$ as

$$N(z) = \frac{d\dot{N}}{dz} = \frac{R(z)}{(1+z)} \frac{dV}{dz}, \quad (2.5)$$

where $R(z) = r_0 e(z)$ gives the total number of sources in cosmic time, which depends upon the event rate. The local rate density r_0 (i.e. rate of individually observable sources in the local universe) estimates the detection rate for a GW detector and $e(z)$ provides the binary source rate over cosmic times. The comoving volume element is

$$\frac{dV}{dz} = 4\pi c \frac{r_z^2}{H(z)}, \quad (2.6)$$

where $H(z) = H_0 \sqrt{\Omega_\Lambda + \Omega_m(1+z)^3}$ is the Hubble parameter (recent constraint on these parameters are in [30]). As a result, from Equations (2.2), (2.4), (2.5) and (2.6) we have

$$\Omega_{GW}(f) = \frac{f}{\rho_c} \frac{r_0}{H_0} \int_0^{z_*} \frac{e(z)}{(1+z) \sqrt{\Omega_\Lambda + \Omega_m(1+z)^3}} \frac{dE_{GW}}{df_s} dz, \quad (2.7)$$

Ω_Λ and Ω_m are the energy densities of dark energy and the matter in the universe. The lower and upper limits of integral changes from 0 to z_* in the frequency range

$f_{s \min} \leq f \leq f_{s \max}/(1+z_*)$ in which a coalescing binary object emits the GWs. In terms of characteristic strain $h_c(f)$, Equation (2.4) will turn out to be [173]

$$\frac{dE_{GW}}{dsdf} = \frac{\pi c^3}{2G} h_c^2(f). \quad (2.8)$$

To study the GW energy spectrum using a power-law distribution of particular interest $\Omega_{GW}(f) \approx f^\alpha$, one can define $dE_{GW}/df_s = Af_s^{\alpha-1}$, where A is the total amplitude. Therefore Equation (2.7) can be re-written as

$$\Omega_{GW}(f, \alpha) = \frac{A}{\rho_c} \frac{r_0}{H_0} f^\alpha J(\alpha), \quad (2.9)$$

where $J(\alpha)$ is a dimensionless function given by

$$J(\alpha) = \int_0^{z_*} \frac{e(z)(1+z)^{\alpha-2}}{\sqrt{\Omega_\Lambda + \Omega_m(1+z)^3}} dz. \quad (2.10)$$

For an inspiraling BBH system with individual binary masses m_1 and m_2 , to show the dependence of power-law spectrum, the energy flux $\frac{dE_{GW}}{df_s}$ for a binary system in Equation (2.7) is

$$\frac{dE_{GW}}{df_s} = \frac{(\pi G)^{2/3} M_c^{5/3}}{3} f_s^{-1/3} \quad \text{for} \quad f_{s \min} \leq f \leq f_{s \max}/(1+z_*), \quad (2.11)$$

where G is the Newton's constant, $M_c = M\eta^{5/3}$ is the chirp mass of the binary system, $M = m_1 + m_2$ is the total mass of binaries and $\eta = m_1 m_2 / M^2$ is the symmetric mass ratio. Hence from Equations (2.7) and (2.11), the GW signal from inspiraling binary at frequency $f \leq f_{s \max}$ is

$$\Omega_{GW}(f) = \frac{8}{9} \frac{1}{c^2 H_0^2} \frac{r_0}{H_0} (\pi G M_c)^{5/3} f^{2/3} J(\alpha). \quad (2.12)$$

The resolved signals in a GW detector correspond to non-overlapping binary signals either in the time or frequency domain. If we have a GW detector with an optimal sensitivity which can detect all the astrophysical sources, there would still be a contribution to the astrophysical SGWB from all the resolved signals due to the superposition of these signals.

2.2.1 Estimation of astrophysical SGWB

The GW signals from a population of unresolved binary sources will contribute significantly to an SGWB in the current and future GW detectors. An SGWB due to the unresolved binary sources can be characterized by a set of intrinsic source parameters $\vec{\theta}$ and the merger rate $R_m(z; \vec{\theta})$ [9, 17]. Thus the energy density spectrum of an SGWB can be written (from Equation (2.7)) as

$$\Omega_{GW}(f, \vec{\theta}) = \frac{f}{\rho_c H_0} \int_0^{z_{max}} dz \frac{R_m(z; \vec{\theta}) \frac{dE_{GW}(f_s; \vec{\theta})}{df_s}}{(1+z)E(\Omega_M, \Omega_\Lambda, z)}, \quad (2.13)$$

where $dE_{GW}(f_s; \vec{\theta})/df_s$ is the energy flux emitted by a binary source at the source frequency $f_s = f(1+z)$ and the term $E(\Omega_M, \Omega_\Lambda, z)$ contains information about the cosmological parameters. The $(1+z)$ term in denominator converts the source frame time to the detector frame. A cutoff for integration is set over redshift value at z_{max} .

The unresolved binary sources can be BBH, BNS and NS-BH (in case of ground-based detectors), so it is important to treat the SGWB from BBH and BNS separately as they have different physical properties such as the difference in mass distribution, energy density spectrum and their formation and the

merger conditions. In case of BNS system, since merger happens at very high frequencies ~ 2 kHz, only inspiral phase is considered with energy spectrum $dE/df_s \propto M_c^{5/3} f_s^{-1/3}$. Whereas for a BBH system, it is necessary to consider the full waveform, which includes the inspiral-merger-ringdown (IMR) phase. Hence, the merger rate for the binary system in terms of binary star formation rate with a time delay is given by

$$R_m(z; \vec{\theta}) = \int_{t_{min}}^{t_{max}} R_f(z_f; \vec{\theta}) p(t_d; \vec{\theta}) dt_d, \quad (2.14)$$

where $R_f(z_f; \vec{\theta})$ is the binary star formation rate, z_f is redshift at time $t_f = t(z) - t_d$ of the binary star formation. Here t_d accounts for the time delay between the formation time t_f and the merger time $t(z)$. Term t_{min} is the minimum time delay between the formation and the merger processes for a binary system whereas t_{max} corresponds to the Hubble time.

The detection of a BBH event GW150914 [9] placed the limit on (the astrophysical SGWB from BBHs) $\Omega_{GW}(f = 25 \text{ Hz}) = 1.1_{-0.9}^{+2.7} \times 10^{-9}$ with a 90% confidence limit, which is well approximated by the power-law $\Omega_{GW} \propto f^{2/3}$ at low frequencies (upto 100 Hz), where the inspiral part dominates the energy flux given in Equation (2.11). The BBH observations made by aLIGO and AdV detectors during the first half of the third observation run (O3) estimates the merger rate $R_m = 23.9_{-8.6}^{+14.9} \text{ Gpc}^{-3}\text{yr}^{-1}$ as a function of redshift [25].

The GW170817 [13, 17] event, the first detection of BNS, provided with a limit (the astrophysical SGWB from BNS) on $\Omega_{GW}(f = 25 \text{ Hz}) = 1.8_{-1.3}^{+2.7} \times 10^{-9}$ with a 90% confidence level and on the merger rate $R_m = 760_{-650}^{+1740} \text{ Gpc}^{-3}\text{yr}^{-1}$. The recent BNS event GW190425 (a BNS event with certain limitations) [21], having a uniform intrinsic mass distribution, provides with the merger rate $R_m = 460_{-390}^{+1050} \text{ Gpc}^{-3}\text{yr}^{-1}$. A combined BNS merger rate for GW170817 and GW190425 is $R_m = 1090_{-800}^{+1720} \text{ Gpc}^{-3}\text{yr}^{-1}$ [21]. The observation made by aLIGO and AdV detectors

during the first half of O3 estimates the merger rate for BNS, $R_m = 320_{-240}^{+490}$ $\text{Gpc}^{-3}\text{yr}^{-1}$ [25].

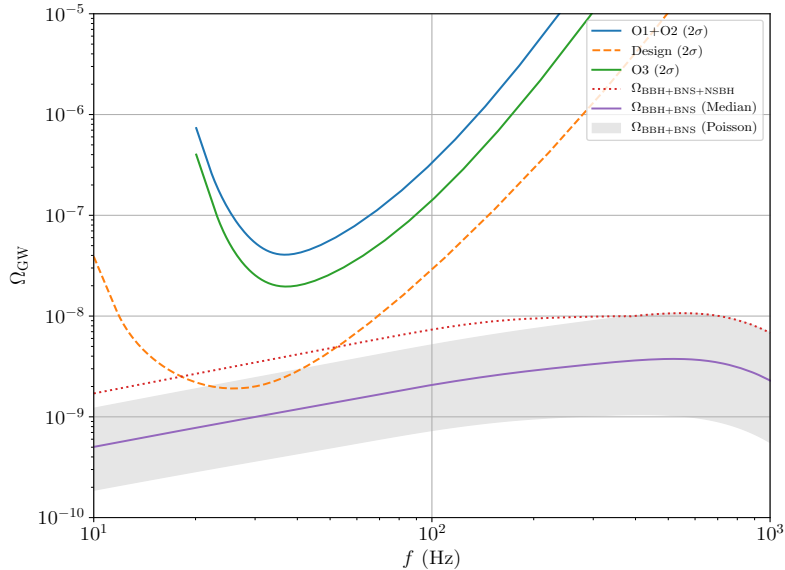


FIGURE 2.3: The sensitivity curves for combined O1+O2 and O3 run of aLIGO and AdV GW detectors with a design sensitivity for the SGWB signal energy density from BBH, BNS and NS-BH. The purple line shows the total SGWB contribution from BBH and BNS with a Poisson error region in grey box calculated from the local BBH merger rate given in [18] and for BNS a combined merger rate from GW170817 and GW190423 events is used [21].

A combined SGWB from coalescing BBH and BNS lies at the high end of the frequency spectrum between 25 Hz - 10^3 Hz of a GW detector, which is the sensitive frequency band for most of the current GW detectors (Figure 2.3 shows the energy density of astrophysical SGWB from BBH, BNS and NS-BH). In future, the detection of various unknown BBH and BNS coalescing processes with updated current GW detectors or future detectors ET and CE will help us to study and understand the nature of astrophysical SGWB and various other stellar processes responsible for their formation. With the results from O3 run, we will see more stringent limits on the merger rate and the energy density spectrum of SGWBs from BBH, BNS and NS-BH binary objects.

2.3 Cosmological stochastic GW background

Apart from astrophysical sources, GWs from cosmological sources also contribute to the overall SGWB. Various early universe processes can produce the SCGWB, including inflation, first-order phase transitions, cosmic strings, vacuum quantum fluctuation and primordial black-holes (PBH) leading to primordial GWs signatures. Figure 2.2 shows the contribution of various cosmological process towards SCGWB. Since gravity interacts very weakly with matter (sources distributed throughout the universe), thus the GWs produced in the early universe survive beside the change in redshift due to the expansion of the universe. Hence, detection of an SCGWB would have a strong impact on our understanding of the early universe phenomena, a few seconds after the big-bang, and fundamental physics. Till now, there is no direct-detection of an SGWB (either of astrophysical or cosmological origin) with the GW detectors. However, the upper limits have been placed on the energy density spectrum of SGWB from the various observation runs of aLIGO and AdV GW detectors.

Subsection 2.3.1 discusses the SCGWB spectrum from the phase transitions in the early universe, Subsection 2.3.2 provides the overview of SCGWB from cosmic strings with the upper limits from O1 and O2 runs of aLIGO. Whereas Subsection 2.3.3 discusses inflation processes and how do these processes contribute to the SCGWB. The contribution of PBHs is discussed in Subsection 2.3.4. The detailed discussion of the concepts of spontaneous symmetry breaking and generation mechanism of scalar fields are not discussed here as there is already a vast literature in existence, but some concepts have been used to understand the production mechanism of the SCGWB spectrum.

2.3.1 Phase Transition in the early universe

After the big-bang, the universe has undergone several physical processes during its cosmological evolution. These process occurred at the phase when symmetries of fundamental interactions start to break down spontaneously. Consequently, the energy gets confined in some regions of the space, whose topological structure defines the nature of the defect. For example, Grand Unified Theories (GUT) transition occurs around the critical temperature $T_c \equiv 10^{15}$ GeV, breaking symmetries into two parts, first is gravity, and the second one is electronuclear forces. The electroweak phase transition took place at times when the critical temperature is around $T_c \equiv 100$ GeV. The QCD phase transitions occurred around the critical temperature $T_c \equiv 200$ MeV, which confines quarks and gluons to form hadrons. With a further downfall in the temperature of the universe below T_c , the symmetry breaks down from $SU(2) \times U(1)$ to $U(1)_{em}$. These transitions due to symmetry breaking can generate a huge energy density spectrum of SCGWB. Since GWs produced in the early universe are weakly perturbed by interactions with masses, the properties of a primordial GW background observed today would provide an unobstructed view on the state of the universe at very early times.

Out of all, in the perspective of GW production mechanism and detection, the most significant source of GWs are the first-order phase transitions [43, 55]. The three components that contribute to the first-order phase transitions are: collision of bubble walls [109, 108, 107, 54], sound waves [96, 97] and MHD (magneto-hydrodynamic turbulence) [52, 53] in plasma after the bubble collision. These three processes coexist and contribute to the SCGWB as a linear combination of energy densities given by

$$h^2\Omega_{GW} = h^2\Omega_\phi + h^2\Omega_{SW} + h^2\Omega_{MHD}. \quad (2.15)$$

2.3.1.1 Scalar field contribution

With the cosmological evolution (following adiabatic expansion), the temperature of the universe falls below the critical temperature T_c leading to the metastable state and the formation of a bubble. In this low-temperature regime, the bubble walls start to expand until they move approximately with the speed of light. This process continues until the temperature of the universe rises back to T_c via thermal or quantum fluctuations, further increasing the energy stored in the bubble walls. With the continuous expansion of the universe, bubble walls become thinner and thinner with high energy density. When two such bubbles with high energy density stored in their walls collide with each other symmetry breaks down, hence, leading to the generation of GWs. The main feature of GW spectrum, peak frequency, amplitude and the slope at low and high wavenumber can be predicted to understand the nature of these fields.

The GW spectrum after bubble collision can be defined as given in [103]. Consider a bubble of radius R_* , then the energy density emitted by bubble would be $\Omega_{GW} \propto (R_* H_*)^2$, where H_* is the characteristic scale provide the peak point of GW production (i.e. Hubble time during the phase transition). Thus the amplitude of GW radiation during the first-order phase transition from a thin-walled bubble at a frequency f , from numerical simulations [99, 43, 55], is given by

$$h^2 \Omega_{env}(f) \approx 1.67 \times 10^{-5} \left(\frac{H_*}{\beta} \right)^2 \left(\frac{\kappa_\phi \alpha}{1 + \alpha} \right)^2 \left(\frac{100}{g_*} \right)^{1/3} \left(\frac{0.11 v_b^3}{0.42 + v_b^3} \right) S_{env}(f), \quad (2.16)$$

where κ_ϕ defines the fraction of energy contributed to the GW out of the total available energy, Figure 2.4 shows the GW spectrum (Equation (2.16)) after the bubble collision for $\kappa_\phi=1$. α is the latent heat released during the process, β is

inverse of the time duration of the phase transition and v_b is the bubble velocity. $S_{env}(f)$ parameterize the shape of the GW radiation given by

$$S_{env}(f) = \frac{3.8(f/f_{peak})^{2.8}}{1 + 2.8(f/f_{peak})^{3.8}}. \quad (2.17)$$

The peak frequency f_{peak} is a function of bubble wall velocity given by

$$f_{peak} \simeq 16.5 \times 10^{-6} \text{ Hz} \left(\frac{f_*}{\beta} \right) \left(\frac{\beta}{H_*} \right) \left(\frac{T_*}{100 \text{ GeV}} \right) \left(\frac{g_*}{100} \right)^{1/6}, \quad (2.18)$$

where

$$f_* = \frac{0.62\beta}{1.8 - 0.1v_b + v_b^2}. \quad (2.19)$$

Equations (2.16) and (2.18) show that the first-order phase transitions have extended with the adiabatic expansion of the universe from Hubble time to the present times. Here g_* is number of relativistic species at temperature T_* when GWs are produced. The bubble velocity is given by the ratio (ζ) of vacuum energy density (ρ_{vac}) to the radiation energy density (ρ_{rad}) at the time of phase transition as

$$v_b(\zeta) = \frac{\sqrt{1/3} + \sqrt{\zeta^2 + 2\zeta/3}}{1 + \zeta}. \quad (2.20)$$

with ratio ζ given by

$$\zeta = \frac{\rho_{vac}}{\rho_{rad}}, \quad (2.21)$$

and β is

$$\begin{aligned}\beta &= \frac{\Gamma'}{\Gamma} = - \left. \frac{dS}{dt} \right|_{t=t_n} \\ &= T_n H(T_n) \left. \frac{dS}{dt} \right|_{T=T_n},\end{aligned}\tag{2.22}$$

where $\Gamma(t)$ is the nucleation rate, and S is a Euclidean action of the bubble. T_n is the temperature at which the first-order phase transition occurs and t_n is the end time of the first-order phase transition.

2.3.1.2 Sound waves contribution

The acoustic waves due to the bubble collision produced in the plasma lead to the GW energy density spectrum given by [96, 97] (see Figure 2.4)

$$h^2 \Omega_{SW}(f) = 2.65 \times 10^{-6} \left(\frac{H_*}{\beta} \right) \left(\frac{\kappa_{SW} \alpha}{1 + \alpha} \right)^2 \left(\frac{100}{g_*} \right)^{1/3} v_w S_{SW}(f),\tag{2.23}$$

where κ_{SW} is the amount of vacuum energy converted into bulk motion of the fluid and depends upon the expansion of the bubble. Figure 2.4 shows the acoustic wave contribution (Equation (2.23)) for $\kappa_{SW} = 1$. Thus the corresponding spectral shape is

$$S_{SW}(f) = \left(\frac{f}{f_{SW}} \right)^3 \left(\frac{7}{4 + 3(f/f_{SW})^2} \right)^{7/2}.\tag{2.24}$$

The peak frequency for sound waves f_{SW} is

$$f_{SW} = 1.9 \times 10^{-5} \frac{1}{v_w} \left(\frac{\beta}{H_*} \right) \left(\frac{T_*}{100 \text{ GeV}} \right) \left(\frac{g_*}{100} \right)^{1/6}.\tag{2.25}$$

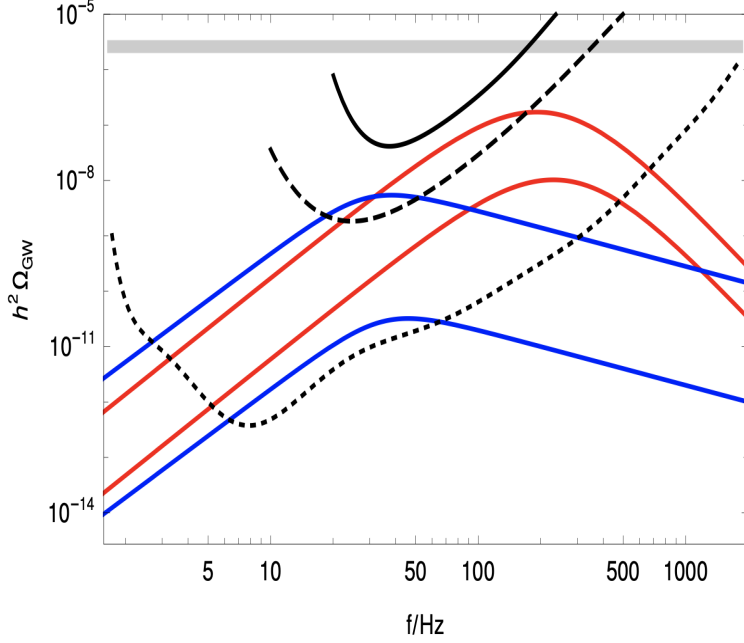


FIGURE 2.4: The SCGWB energy density spectrum from the first-order phase transitions and the sensitivity curves for aLIGO with combined O1 and O2 data (in solid black line) with aLIGO sensitivity (in dashed line) and for ET detector (in dotted line). The grey shade area comes from the indirect upper bound set by Planck CMB data. The blue lines correspond to the bubble wall collision with $\kappa_\phi = 1$, and the red lines shows the sound waves contribution with $\kappa_{SW} = 1$ to the energy density curve for some realization of first-order phase transition model (Figure from [168]).

On comparing Equations (2.16) and (2.23), the spectral shape differ by a factor of β/H_* which is due to the long-lasting nature of sources producing GWs.

2.3.1.3 MHD contribution

A magneto-hydrodynamic (MHD) turbulence in the plasma contributes to the GW spectrum as given by [52, 53, 43]

$$h^2 \Omega_{MHD}(f) = 3.35 \times 10^{-4} \left(\frac{H_*}{\beta} \right) \left(\frac{\kappa_{MHD} \alpha}{1 + \alpha} \right)^{3/2} \left(\frac{100}{g_*} \right)^{1/3} v_w S_{MHD}(f), \quad (2.26)$$

where κ_{MHD} is heat transferred during the turbulence in the plasma. In similar manner to Equations (2.16) and (2.23), there is an additional contribution from the term β/H_* for sources which last longer than $1/\beta$ during the phase transitions. The spectral shape for MHD is given by

$$S_{MHD}(f) = \frac{(f/f_{MHD})^3}{\left[1 + (f/f_{MHD})^{11/3}\right] (1 + 8\pi f/h_*)}, \quad (2.27)$$

where h_* is the Hubble rate given by

$$h_* = 16.5 \times 10^{-6} \left(\frac{T_*}{100 \text{ GeV}} \right) \left(\frac{g_*}{100} \right)^{1/6}. \quad (2.28)$$

Similarly to the sound wave contribution (Sub-subsection 2.3.1.2), the peak frequency in MHD f_{MHD} is in inverse relation with the source length scale

$$f_{MHD} = 2.7 \times 10^{-5} \frac{1}{v_w} \left(\frac{\beta}{H_*} \right) \left(\frac{T_*}{100 \text{ GeV}} \right) \left(\frac{g_*}{100} \right)^{1/6}. \quad (2.29)$$

Figure 2.5 shows the potential of future generation ground-based GW detectors ET and aLIGO+ to detect the signatures of first-order phase transition as a function of parameter κ .

2.3.2 Cosmic Strings

Cosmic strings are one-dimensional topological defects with energy concentrated along the one-dimensional line. Cosmic strings are produced in the early universe when field undergoes a spontaneous symmetry breaking phase transition. These one-dimensional strings can either be closed-loops or infinitely long in shape, and can even maintain a small fraction of the total energy density from the very early universe to present time. The most interesting cosmic strings to

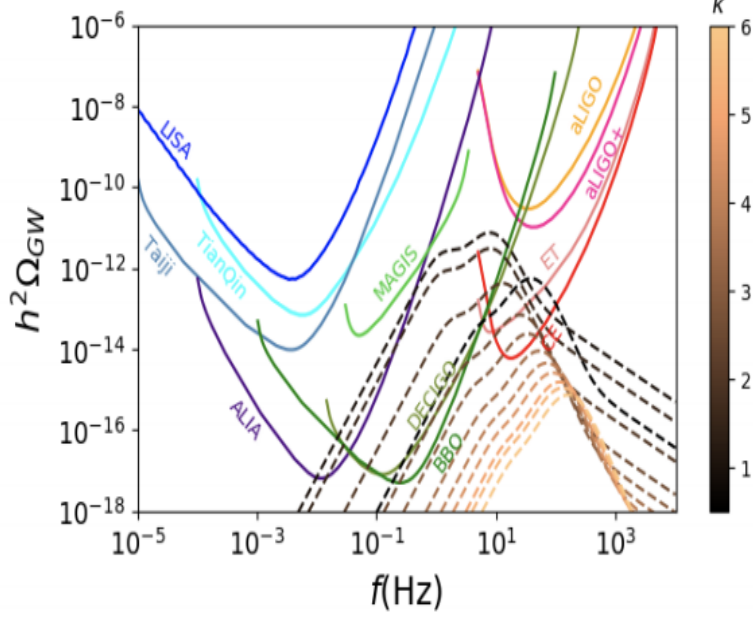


FIGURE 2.5: Plot showing the first-order phase transition energy density spectrum as a function of parameter κ with various ground-based and space-borne GW detector's sensitivity curve (Figure from [77]).

study are Nambu-Goto strings on cosmological scales [139]. The important trait of Nambu-Goto strings is that they are stretched by the expansion of the universe and characterized by the scale factor $a(t)$. If cosmic strings exist, they would be present throughout the history of the universe. Nambu-Goto cosmic strings lead to the production of loops and then to GW emission. Thus, such radiations can lead to a signature of SCGWB, which can be observed in the observational frequency band of ground-based or space-borne GW detectors. These strings can induce anisotropies into the cosmic microwave background (CMB), and their existence can be tested via CMB measurements. CMB data from Planck experiment [130] and numerical simulation to search for cosmic string signals constrain the Nambu-Goto string tension $G\mu < 1.5 \times 10^{-7}$ and Abelian-Higgs strings with $G\mu < 2 \times 10^{-7}$ [122, 114]. [84] provides an in-depth review of the SCGWB from cosmic strings and the detection limits with ground-based and space-borne GW detectors.

How do cosmic strings produce GWs? To understand this question, it is crucial to know what are the properties of these strings and how much energy do these strings have (or they produce) such that one can access cosmic string parameters through GW observations. Cosmic strings can develop two different types of structures, namely kinks (discontinuities on the tangent vector of string) and cusps (when string reaches the speed of light). The probability of intersection between cosmic strings is an essential quantity as it provides with the cosmological evolution of cosmic string network [101]. The different channels for cosmic strings to interact are when two long cosmic strings intersect each other, or a single string intersects itself. The first interaction method leads to the production of two kinks and one loop formation, whereas the latter part leads to one kink and a loop formation (loops can also form cusps). Hence, string loses energy in the form of loops which then decay by radiating GWs. The kinks and cusps can create a burst of GWs, leading to a superposition of stationary and Gaussian GWs, thus leading to an SCGWB.

A cosmic string loop with length L has a period $T = L/2$, frequency $\omega = 4\pi/L$ and mass $M \sim \mu L$, where μ is mass per unit length of the string. Therefore, the power emitted by cosmic strings with frequency ω and decay lifetime $\tau = L/P$ during the various harmonics as they move relativistically is

$$P = \Gamma G\mu^2 , \tag{2.30}$$

where the numerical factor Γ is a dimensionless quantity, and G is the gravitational constant. $\Gamma \sim 50 - 100$ is a radiative efficiency factor provides with the effectiveness of GW emission. The term $G\mu$ is a dimensionless string tension parameter, which characterize the cosmic strings. Since μ depends upon the mass of the cosmic string, therefore, a massive string will decay much faster. The energy radiated by a cosmic loop in the form of GWs can be defined as

$$\mu \frac{dL}{dt} = -\Gamma G \mu^2. \quad (2.31)$$

The term dL/dt represents the loss in energy. For a cosmic loop with a length L_0 at any time t_0

$$L_0(t_0) = \alpha t_0, \quad (2.32)$$

where α is constant loop size parameter, the lifetime of the string due to the GW emission would be $T = L_0/(\Gamma G \mu)$. For a cosmic string of length L , which is a function of time (t), the length of the cosmic loop will decrease at initial time t_i (the time at which loop is created) given by

$$L(t) = L_0(t_i) - \Gamma G \mu(t - t_i). \quad (2.33)$$

The GWs emitted by a cosmic loop of length L lies on a specific frequency $f_{emit} = 2n/L$, where n is an integer and give normal modes of oscillation. All these processes of intersection between various cosmic strings, oscillation and emission allow cosmic strings to shed energy without dominating the energy density of the universe. The GW energy emitted by the cosmic strings redshifted as a^{-1} . Therefore the frequency f , observed with a GW detector from oscillation mode n , is related to the GW emission time and cosmic loop formation rate as

$$f = \frac{2n}{\alpha t - \Gamma G \mu(t - t_i)}. \quad (2.34)$$

The GW energy density per unit frequency is [71] (Figure 2.6 shows Ω_{GW} for the various realization of $G\mu$)

$$\Omega_{GW} = \frac{f}{\rho_c} \frac{d\rho_{GW}}{df} = \sum_n \Omega_{GW}^n(f), \quad (2.35)$$

where

$$\Omega_{GW}^{(n)}(f) = \frac{1}{\rho_c} \frac{2n}{f} \frac{0.1\Gamma^{(n)}G\mu^2}{\alpha(\alpha + \Gamma G\mu)} \int_{t_F}^{t_0} dt \frac{C_{eff}(t_i)}{t_i^4} \left[\frac{a(t)}{a(t_0)} \right]^5 \left[\frac{a(t_i)}{a(t)} \right]^3 \Theta(t_i - t_F), \quad (2.36)$$

where C_{eff} is the loop production coefficient and $\Gamma^{(n)} = \Gamma/(3.6 \cdot n^{4/3})$ is the emission rate per mode. The formation time of a loop of n^{th} mode is a function of the GW emission time t given by

$$t_i(t, f) = \frac{1}{\alpha + \Gamma G\mu} \left[\frac{2n}{f} \frac{a(t)}{a(t_0) + \Gamma G\mu t} \right]. \quad (2.37)$$

2.3.2.1 Limits from GW detection

The GW detectors aLIGO searched for the GW burst signal from cosmic string loops during the O1 run (from 2015-2016) [16]. Without any concrete evidence of the signals from cosmic strings, an upper limit has placed on the cosmic string parameters for various loop distribution models [16, 64].

A GW burst signal emitted by cusps and kinks in a frequency domain is

$$h(L, z, f) = A_q(L, z) f^{-q} \Theta(f_h - f) \Theta(f - f_{low}), \quad (2.38)$$

where $q = 3/4$ and $q = 5/3$ for cusps and kinks respectively. f_{low} is the lower frequency cutoff determined by kinks or cusps amplitude $A_q(L, z)$ (from a string of loop size L at redshift z). The amplitude $A_q(L, z)$ is given by

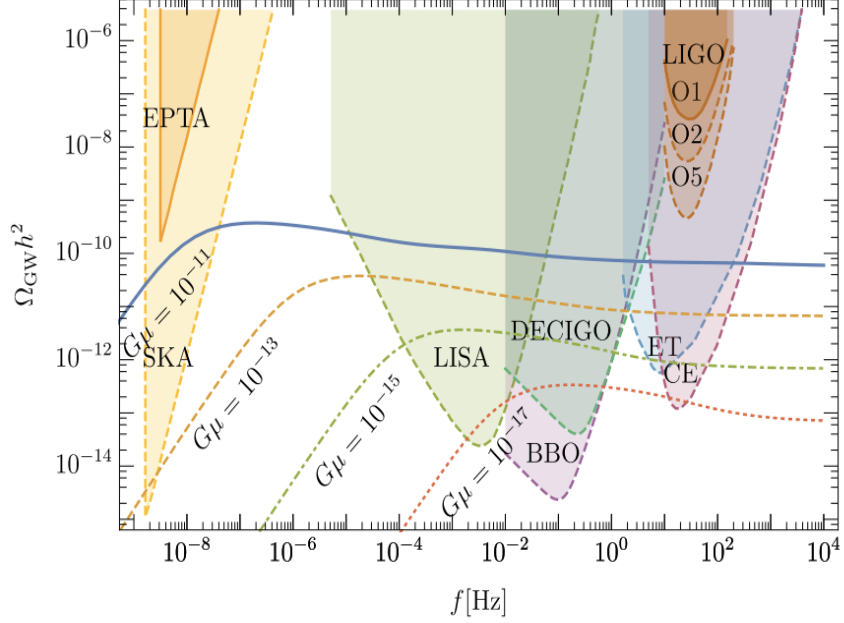


FIGURE 2.6: The plot shows the SCGWB energy density spectrum from the cosmic string network for the different realization of parameter $G\mu$ with $\alpha = 0.1$ and the sensitivity curve of aLIGO, future ground-based GW detectors ET and CE, space-borne GW detectors LISA [76], DECIGO [104] and BBO [70] with European Pulsar Time Array (EPTA) and Square Kilometre Array (SKA) (Figure from [71]).

$$A_q(L, z) = g_1 \frac{G\mu L^{2-q}}{(1+z)^{q-1} r(z)}, \quad (2.39)$$

where $r(z) = H_0^{-1} \varphi_r(z)$ is the proper distance to the source and depends on the Hubble parameter H_0 , and quantity $\varphi_r(z)$ consisting of cosmological parameters. The parameter g_1 gathers uncertainties and becomes crucial for the calculation of cusps and kinks waveforms. The waveform in Equation (2.38) is valid only when it is linearly polarized, and beaming angle is

$$\theta_m(L, z, f) \equiv (g_2 f (1+z) L)^{-1/3} < 1, \quad (2.40)$$

where g_2 is a numerical factor and θ_m must be less than one for the detection of a GW from cosmic string (cusps or kinks).

The analysis of O1 and O2 data from aLIGO detector [20] placed upper limits on cosmic strings parameter $G\mu \leq 1.1 \times 10^{-6}$ for model [45] and $G\mu \leq 2.1 \times 10^{-14}$ for model [115]. Figure 2.6 shows the GW energy density spectrum from a cosmic string network with different set of values for $G\mu = 10^{-11}, 10^{-13}, 10^{-15}, 10^{-17}$ respectively, with the current, future ground-based and space-borne GW detectors sensitivity curves towards the cosmic string SCGWB detection. Based on the number of CBC signals expected to be observed by future GW detectors, there would be an observation of the astrophysical SGWB. Since the astrophysical SGWB peaks in the frequency range 1 Hz - 1000 Hz with $\Omega_{GW} = 10^{-9}$ (following a power-law distribution $f^{2/3}$), the CBC background will overlap with the cosmic string background, further making it difficult to differentiate between two backgrounds. However, cosmic string background for values $G\mu > 10^{-15}$ (see Figure 2.6) would be easy to observe with space-borne GW detectors well above the astrophysical SGWB. For a possible detection of the cosmic string background with ground-based GW detectors, it is necessary to subtract the foreground of astrophysical sources. The reduction in the astrophysical SGWB will improve the detection probability of all SGWB (including cosmic string background) that are masked by CBC foreground. [136] suggested that the astrophysical SGWB with future GW detectors can be reduced upto a level $\Omega_{GW} = 10^{-13}$ whereas BBO [70] will provide much better sensitivity after background subtraction [91]. For this purpose, with the future-generation ground-based GW detectors ET and CE, I studied a subtraction-noise projection method (see Chapter 3) to reduce the contribution of astrophysical SGWB and to increase the sensitivity of GW detectors towards the SCGWB detection.

Besides the contribution from coalescing binaries to the SGWB, it is also vital to distinguish cosmic string background from the other SCGWB in the detector data. A distinctive feature of cosmic string background which separates them from the other SCGWB is that they have a flat plateau at higher frequencies (see Figure 2.6). If we compare this with the first-order phase transition GW

background in Figure 2.5, the spectrum in phase transition follows a power-law in frequency which falls at higher frequencies.

The other challenge can come from the inflationary background. The power spectrum of an inflationary background is scale-invariant, thus, the GW energy density spectrum would be flat (see Subsection 2.3.3). Since the SCGWB spectrum from inflation varies as f^{-2} at lower frequencies $f \leq 10^{-16}$, in the matter era, it would be analogous to cosmic string signal as they rise with $f^{-1/2}$ in the matter era. Further, the CMB isotropic and polarization measurement set the limits $\Omega_{GW} \leq 10^{-15}$ (for $f < 10^{-15}$ Hz) on the GW energy density spectrum from the inflation.

2.3.3 GWs from inflation

A GW signal from inflation [86, 112] is due to the amplification of quantum fluctuations in the standard inflationary model. Inflation plays an important role to understand the early universe as it addresses the origin of primordial fluctuations (inhomogeneities), which are required to explain the large scale structure formation of the universe. These fluctuations are the quantum fields (scalar or tensor field) in the inflationary background, giving rise to the SCGWB. Besides these contributions, fields in inflationary dynamics can give rise to the anisotropies (traceless and transverse components), playing the role of SCGWB sources. Whereas, theories of modified gravity lead to non-standard GW sources [87, 41]. Since these primordial fluctuations are the quantum fluctuations, therefore, they will introduce the spatial dependence into the spacetime metric with a scale-invariant spectrum. Amplification of these metric fluctuations during the transition between de Sitter, the radiation dominated and the matter-dominated phases produces an SCGWB when stretched over the horizon scale. The energy density then gives the magnitude of these fluctuations. CMB observations [30] provides us with the order of these fluctuations to be around $\sim 10^{-5}$ leading to

the fact that primordial fluctuations have a nearly a scale-invariant power spectrum. Further, inflation also helps to understand the Gaussian or non-Gaussian nature of these quantum fluctuations.

If a GW signal from the inflationary background is detected in future, it will provide a promising way to test the inflation models, to probe the quantum nature of fields and gravity. In the standard inflation models, expansion is caused by the slow roll of a scalar field to its minimum potential and the tensor fluctuation is characterized by a scale-invariant spectrum. The power spectrum from inflationary background can be connected to the GWs, thus, opening a window to study and constrained the cosmological parameters. In particular, the GWs affect the multipole of the temperature and give rise to the polarization anisotropies of CMB photons during their propagation from the last scattering surface. The relic of such SCGWB from the early universe can be detected by ground-based or space-borne GW detectors. The energy density of irreducible GWs from inflation encodes information about its energy scale or the Hubble parameter during the inflation [41]. The amplitude of this irreducible background at CMB scale ($f = f_{CMB}$) is given by

$$h^2\Omega_{GW}^{CMB} \equiv h^2\Omega_{GW}(f_{CMB}) \approx 5 \times 10^{-16} \left(\frac{H}{H_{max}} \right)^2, \quad (2.41)$$

which is represented in terms of frequencies corresponding to CMB scale $f_{CMB} = 10^{-18}$ Hz -10^{-17} Hz, H is inflationary Hubble parameter at CMB scale and $H_{max} = 8.8 \times 10^{13}$ GeV is the current upper bound on H . If the energy density of GWs can be parametrized at different frequencies as a power-law distribution, then the present SCGWB energy density Ω_{GW} in Equation (2.41) is

$$\Omega_{GW}(f) = \Omega_{GW}^{CMB} \left(\frac{f}{f_{CMB}} \right)^{n_T}, \quad (2.42)$$

where $n_T = -r/8$ is a spectral index in the single slow-roll inflation models with $r = A_T/A_S$ known as the tensor-to-scalar ratio. A_T and A_S are the amplitude of primordial tensor and scalar power spectra.

2.3.4 Primordial black holes

In the past couple of years, a surge to search for PBH signals with the GW detectors has grown exponentially. This is also due to an increase in the potential to observe the GWs over a vast frequency spectrum from 10^{-9} Hz - 4×10^3 Hz including pulsar time array's (PTA) [36], space-borne Laser Interferometer Space Antenna (LISA) [76], Big-Bang Observer (BBO) [70], TianQin [116], Deci-Hertz Interferometer Gravitational wave Observatory (DECIGO) [104], TAIJI [117] and ground-based detectors aLIGO, AdV with upcoming detectors ET and CE. The first BBH detection GW150914 (triggering event for BBH studies) and the recent observations of BBH [25] to name a few are, GW190425 and GW190814, where one of the BBH mass is less than $10M_\odot$ can point towards the fact that with future GW detectors it would be possible to detect the signal from coalescing PBH formed in the early universe. PBHs are also interesting candidates for cold dark matter in the universe in the mass range of 1-10 M_\odot [66].

The main scenarios responsible for the PBH formation are the gravitational collapse of highly overdense regions in the early universe and the non-linear structure formation. The most common mechanism for PBH formation is the gravitational collapse of primordial fluctuations during the inflation period (radiation and matter era) when these fluctuations reenter the Hubble horizon. These small scale perturbations lead to the scalar perturbation of second order. A review on the PBH formation, merger and detection is in [152, 85]. The detection of a GW signal from PBH explicitly depends upon their formation mechanism and models being used for the studies. Therefore, the detection of a GW signal from PBH

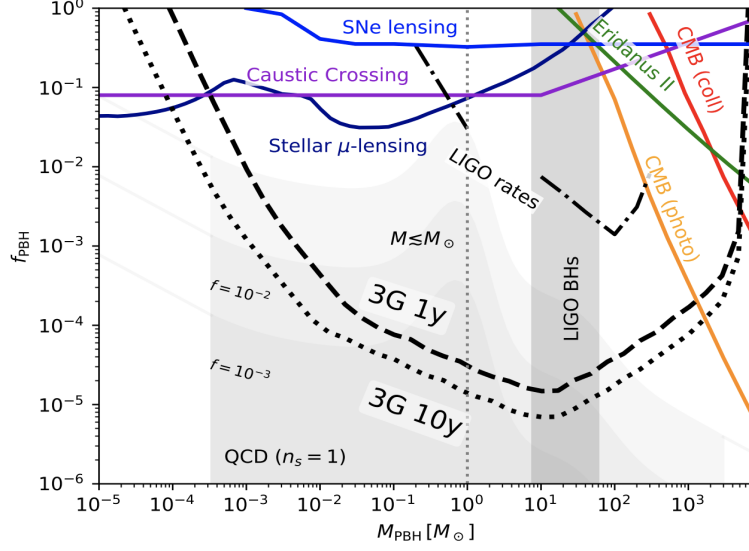


FIGURE 2.7: Plot showing the upper limits from different observations with the sensitivity curve of third generation (3G) GW detector, constraints are from aLIGO observations and upper limits on microlensing of SNe, caustic disruption, Planck and other various observations. The shaded region represents the PBH mass distribution (which depends upon the density power spectra) due to the QCD phase transition with a mass density centered at $\sim 10M_\odot$ (using merger rates from LIGO observations) [51], for different PBH abundance and a primordial scale invariant spectrum (figure from [124]).

will help to understand the distribution and nature of the matter in the universe and the corresponding formation mechanism and models therein.

The mass of PBH at formation when primordial fluctuation reenters the Hubble horizon is associated with horizon mass M_H through the relation given by [57]

$$M_{PBH} = \gamma_{GC} M_H = \gamma_{GC} \frac{4\pi}{3} \rho (H^{-1})^3, \quad (2.43)$$

where γ_{GC} is an efficiency parameter for the gravitational collapse, ρ is the energy density of the epoch in which these primordial fluctuations enter the horizon. Since PBHs are epoch dependent, i.e. matter or radiation epoch, PBH mass (i.e. the amount of the universe mass out of which PBH is formed) depends on the value $\beta(M)$ of the mass scale of the epoch (M) at the time of formation. If

PBHs are monochromatic in the mass function, the mass they have during the formation time t_i will also depend on their number density $n_{PBH}(t_i)$ given by [58]

$$\beta(M) = \frac{Mn_{PBH}(t_i)}{\rho_{t_i}}, \quad (2.44)$$

where ρ_{t_i} is the energy density during the formation of PBH. The abundance of PBH as a function of mass M can be defined as the ratio of energy densities given by

$$f_{PBH}(M) \equiv \frac{\Omega_{PBH}(M)}{\Omega_c}, \quad (2.45)$$

where $\Omega_{PBH} = \rho_{PBH}/\rho_c$ and $\Omega_c = \rho/\rho_c$ are the present normalized energy densities. The quantity f_{PBH} is a crucial parameter which helps to distinguish the PBH properties and used to characterize them. Figure 2.7 shows the current limits on PBH studies and the potential of third-generation GW detectors to observe the mass and the spatial distribution of PBH. The present energy density for PBH (not yet evaporated) is

$$\Omega_{PBH} = \frac{Mn_{PBH}(t_0)}{\rho_c}. \quad (2.46)$$

The present merger rates of PBH from binaries formed in the early and the late universe are given in [134]. Using Equation (2.7) and a choice of the energy density profile of PBH in Equation (2.46), one can predict the energy density spectrum Ω_{GW} of PBH. [119, 152, 66] and references therein provides with various approaches to study the energy density spectrum of PBH and their merger rates.

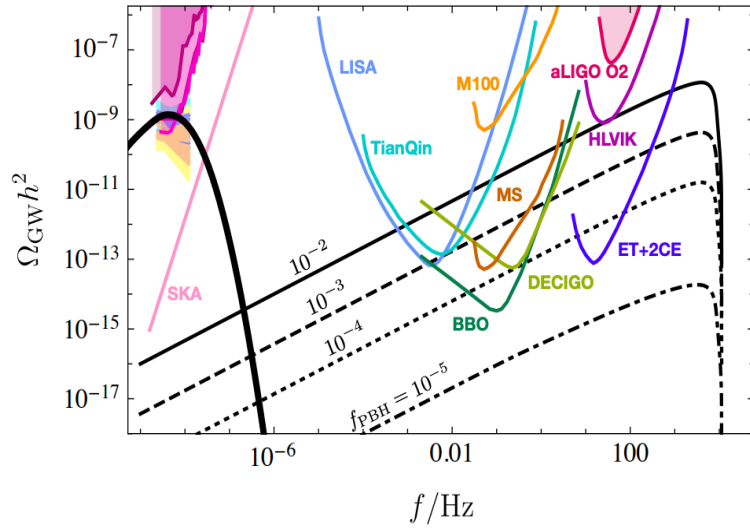


FIGURE 2.8: The GW energy density spectrum for PBH merger events in thick solid black line with mass $M_{\text{PBH}} = 1M_{\odot}$ and various realization of present energy density fraction $f_{\text{PBH}} = 10^{-2}, 10^{-3}, 10^{-4}$ and 10^{-5} is shown with the detection sensitivity of current, future ground-based and space-borne GW detectors (Figure from [106]).

Chapter 3

Subtraction-noise projection method for SCGWB searches

3.1 Introduction

The accomplishment of detecting GWs from the mergers of BNS and BBH systems opened a new window to study the astrophysical and cosmological phenomena of the universe. The continuous improvement in the sensitivity and detection of several GW signals from the coalescence of BNS and various BBHs during the O1, O2 [19] and O3 run [6, 25] of aLIGO [37] and AdV [27] detectors marks the beginning of a cosmic catalog of sources so far, reaching out to distances of about 3 Gpc and only capturing a small fraction of all compact binaries in this volume [19].

A primary objective of modern cosmology is to detect the early universe GW signals, which are crucial to test current cosmological models and to further our understanding of the evolution of the universe [8, 29]. A cosmological SGWB (SCGWB) signal can arise from various processes, as discussed in Chapter 2. On the theoretical side, there is a vast advancement to understand the concept and

generation of these SCGWB. In contrast, on the observational and experimental side to detect these signals with GW detectors is also in advancement and provides us with the capability to detect these signals in the future. If detected, an SCGWB provides a direct window to study the early universe phenomena and fundamental physics.

However, the detection of an SCGWB is exceptionally challenging. Mission concepts that would make the detection of an SCGWB more probable, the space-borne detectors Big-Bang Observer (BBO) [70] and DECIGO [104], still require substantial advances in laser-interferometer technology, and it is unknown when or if these experiments will become operational. Two ground-based, third-generation GW detectors have been proposed, ET and CE (see Chapter 1 Section 1.4), which are expected to be operational by 2035 and potentially with the capacity to detect an SCGWB. The SCGWB is predicted to lie well below the instrument noise of all conceived future GW detectors. The SGWB searches with GW detectors follow the cross-correlation method based on the assumption that fields of SGWB produce correlations between detectors, while the instrument noises do not, or in a well-understood way with options to mitigate correlated noise, e.g., Schumann resonances [159, 68]. Optimal cross-correlation filters (see Appendix C.5, C.6 and Subsection 4.2.2) can be employed to obtain the maximum SNR integrated over a band of frequencies and thus maximizing our chances to detect an SCGWB [63, 35]. It is also possible to estimate parameters of SCGWB such as spectral slopes and possible anisotropies of the GW field [40, 142].

With the proposed third-generation GW detectors ET and CE, we will step into a new era of GW physics, and we will overcome the scarcity of GW sources, such that we will be able to detect binary signals up to high redshifts $z \geq 10$. Analyses of data from the O1 and O2 runs of LIGO and VIRGO constrain the local BBH merger rate to about $10 - 100 \text{ Gpc}^{-3} \text{y}^{-1}$ [18]. The BBH merger rate as

a function of redshift is estimated from the star-formation rate [163], distribution of time-delays between formation and merger [42], and by normalizing to the local merger rate [167]. It predicts about $10^5 - 10^6$ BBH mergers per year and a large fraction of them detectable with ET or CE. Since cross-correlation between detectors (Appendix C.5) is predicted to be dominated by an astrophysical foreground of CBCs, detection of an SCGWB is strongly impeded, and mitigation of the foreground is required.

For a detector to be sensitive enough to detect the SCGWB, it is necessary to subtract the GW foreground from $10^5 - 10^6$ coalescing binaries. The foreground created by such a large number of CBCs will dominate over the detector's instrumental noise which in turn will dominate the SCGWB. To achieve a sensitivity threshold with the ET and CE towards the detection of an SCGWB, as a first step, the foreground can be reduced by subtracting the estimated waveforms of all detected signals. Previous work has shown that a combination of unresolved sources, i.e., signals lying below the detection threshold, and residuals left in the data after subtraction can still limit the sensitivity of SCGWB searches with future GW detector networks [137, 147]. Both publications neglected the possibility to reduce subtraction residuals as proposed in earlier work for space-borne detectors [73, 91]. Furthermore, a full-Bayesian analysis of primordial and astrophysical signals is expected to lower the impact of sub-threshold signals [156].

The subtraction of estimated best-fit waveform signal from the detector data will give rise to residual noise due to mismatch between the estimated best-fit and physical parameters of the GW signal, whereas all unresolved sources will contribute to a confusion noise. This residual noise (a combination of instrumental noise + subtraction residuals), in addition to confusion noise, would be too high and still mask an SCGWB [91]. To be able to search for a primordial signal, we need to project out this noise from the detector's data stream. Consequently,

an SCGWB might become the dominant contribution to correlations between detectors.

In this work, I study a subtraction and noise projection method to deal with the problem of reducing the subtraction residuals of the astrophysical foreground in ET and CE, and for this goal I test the subtraction-noise projection method for BBH [73, 91], significantly improving our chances to detect an SCGWB. As was pointed out in a recent publication [147], the foreground of BNS is expected to be more challenging to reduce. However, I have not simulated this problem beyond what has already been done in previous work, as it requires an effective posterior sampler for parameter estimation in ET, which is a major challenge due to the length of BNS waveforms in ET (around a day), and it needs to account for the rotation of Earth during the observation time. I carried out the analysis based on simulations of ET and CE, and using posterior sampling for the parameter estimation of BBH mergers. I also discuss the misconceptions of residual noise in the context of Gaussian parameter estimation.

The chapter is organized as follows. Details of the simulation of the detector network and astrophysical foreground are presented in Section 3.2. In Section 3.3, I introduce the subtraction-noise projection and the binary parameters that I use to study BBH population. With the subtraction-noise projection method, I study the signal model using Fisher matrix and provide an estimate of the residual noise.

Section 3.4 deals with the importance of the waveform template in the subtraction of GW signals. On the other hand, Section 3.5 sheds light on the different channels of noise contribution and challenges in implementing the subtraction-noise projection method. The projection of the residual noise is discussed in Section 3.6 with a geometrical interpretation, hence providing a better understanding of how projection method works. The cross-correlation measurement

between CE and ET is discussed in Section 3.7. At last, I discussed the result of the foreground-mitigation procedure in Section 3.8 after projecting out the residual noise from the data stream of a GW detector, with a conclusion in Section 3.9.

3.2 Simulation overview

The second-generation GW detectors aLIGO and AdV, after incremental updates, already observed several tens of binary-merger signals including the candidates of the last observing run [18]. There is still a vast region of GW physics that remains unexplored both in astrophysics and cosmology. To explore this new physics, we need next-generation GW detectors with much better sensitivity than current GW detectors. Two ground-based detectors have been proposed so far: ET and CE [131, 12]. Individually and as a detector network together with advanced versions of current-generation detectors (including KAGRA [33] and LIGO India [157]), these third-generation detectors have a rich science case covering topics in fundamental physics, cosmology, astrophysics, and nuclear physics [124, 118].

The simulation consists of two case studies which depend upon the choice of BBH distribution (choice of redshift distribution in particular) to perform the analysis as follows

1. **Case1** : Calculation of a 1.3-year-long stretch of GW data for ET (three individual data streams) and CE divided into 10000-time segments of length 4096 s for 100 BBHs with highest SNR (i.e. all BBHs are in local Universe with redshift $z < 0.1$) [154]. These highest SNR signals are extremely loud signals, i.e. I deliberately chose the first 100 injections (ascending order in

redshift) from a cosmological distribution of 10^6 BBH signals. Figure 3.1a shows the redshift vs SNR distribution of these 100 BBH signals.

2. **Case2:** In this case, I again simulated a 1.3 year-long stretch of the GW data for ET and CE detectors, and divided them into 10000-time segments of length 4096 s for 100 BBHs with $\text{SNR} > 10$. Figure 3.1b shows the redshift vs SNR distribution of these 100 BBH signals. [153].

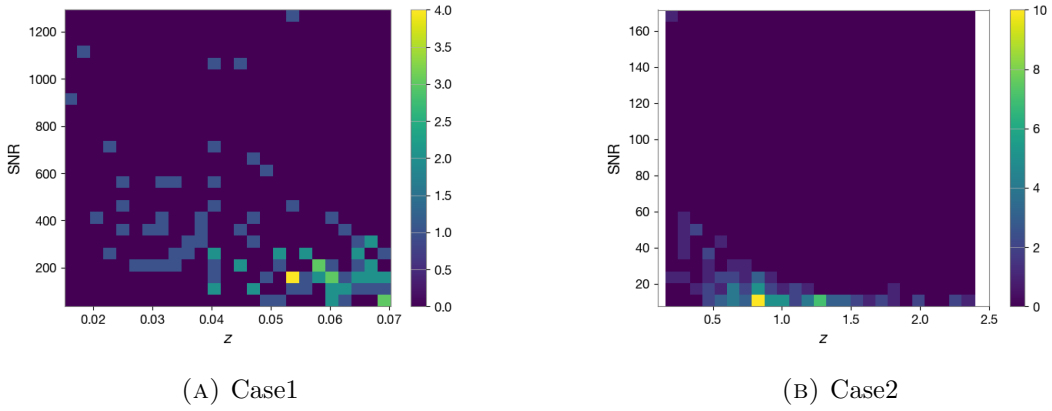


FIGURE 3.1: Plots showing the 2D histogram of CE and ET detectors SNR with respect to the redshift of 100 BBH signals used for studies in Case1 and Case2.

Besides these assumptions, the rest of the approach to study the cases mentioned above is similar. Further, we will also see the effect of BBH candidates with different distribution on the mismatch between true source parameters and estimated best-fit parameters and how these different choices of BBHs will affect the efficiency of projection method to reduce the residual noise.

For a GW detector, with an observation time period T_{obs} (the total observation time I consider for studies is $\sim 10^7$ s), which consist of $n_{seg} = 10000$ number of data time segments, each of duration $T_{seg} = 4096$ s. The data stream of a detector T_i^s , where i is the number of detectors and s is the output of the detector, can be considered as a vector \mathcal{V}_i . Consequently, data segments are also vectors of this vector space \mathcal{V}_i . The output data from a detector is sampled

uniformly with a sampling frequency f_s (2048 Hz, in our studies) giving the total number of measuring points equal to $N = f_s \cdot T_{obs}$. Further, measuring point at any time $t_k = k/f_s$ can be considered as a part of N dimensional vector $T_i^s = (T_i^s(t_1), T_i^s(t_2), \dots, T_i^s(T))$ in \mathcal{V}_i of all detector outputs [39, 91].

The subtraction of estimated best-fit waveforms is carried out in time domain, while the residual-noise projection is most comfortable to perform in the domain of the waveform model (i.e. frequency domain in the studies) as explained in Section 3.6. The projection requires Fisher matrices, which in turn require the derivatives of waveforms with respect to their parameters. I carry out the differentiation numerically so that in future, I can use this simulation also to study systematic related to waveform modeling without requiring analytical waveforms. Cross-spectral densities (CSDs) of time series between all four detectors are calculated after each of the following steps [154],

1. creation of time series only with instrument noise,
2. injection of GW signals in ET + CE detectors,
3. subtraction of estimated best-fit waveforms,
4. residual-noise projection

to demonstrate the impact of each step on the CSD. Finally, optimal filters are applied for an evaluation of the ultimate sensitivity of the network to an SCGWB.

Whenever possible, the analysis uses functions of the Python parameter-estimation software package *Bilby* [38, 144]. The calculation of noise time series is done by built-in functions of *Bilby* using instrument noise models of ET and CE in the form of spectral densities. Also, injection of GW signals in the data and posterior sampling are done with *Bilby*. Subtraction of the best-fit waveforms is done using the injection algorithm with a change of the sign of the waveform.

To implement the projection of residual noise I wrote a code for projection part incorporating all the requirements mentioned earlier. The optimal filters used in the final step for the detection of an SCGWB depend on the ORF between detectors (see Appendix B), which can be calculated straightforwardly using antenna pattern functions provided by Bilby.

However, even when focusing on BBH mergers, providing parameter estimations of $10^5 - 10^6$ signals by posterior sampling, which is an important ingredient in this work compared to previous studies of the projection method, is computationally prohibitively expensive. As a way forward, I adopted the following scheme. Only 100 BBH signals are selected to perform a Bayesian statistical approach for the parameter estimation to calculate the best-fit (maximum likelihood) parameters. Calculating the best-fit estimates also supports the idea that all binaries have been detected, thus representing an optimal scheme for the analysis, i.e. to search for all BBH signals simultaneously. The other way is a hierarchical approach, starting with the signal with the highest SNR and going step by step down to the lowest SNR until the last binary is identified and detected. In this way, parameters of detected binaries can be refined with the decrease in the confusion noise.

After having an ensemble of all 100 BBH signals for each case, I injected them into ET and CE detectors network to simulate a foreground of BBH signals in addition to the detector noise. The idea behind this approach is to avoid the full-scale CBC analysis and calculate the residual-noise vector on the waveform template manifold. However, in a realistic scenario, it is crucial to identify all the CBC signals individually from the data stream of a detector.

In the cases mentioned above, all 100 BBH waveforms are injected with random time shifts so that the merger occurs in the respective time segment. In this way, phase relations between all signals are randomized, and the CSD between detectors has the properties of a stochastic foreground. In Case1, the

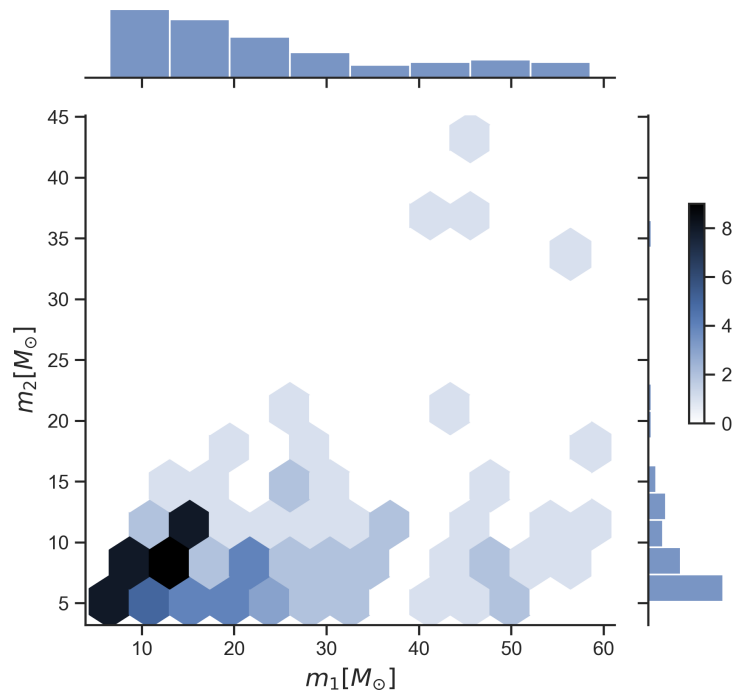


FIGURE 3.2: Mass range for individual BBH mass used in **Case1**.

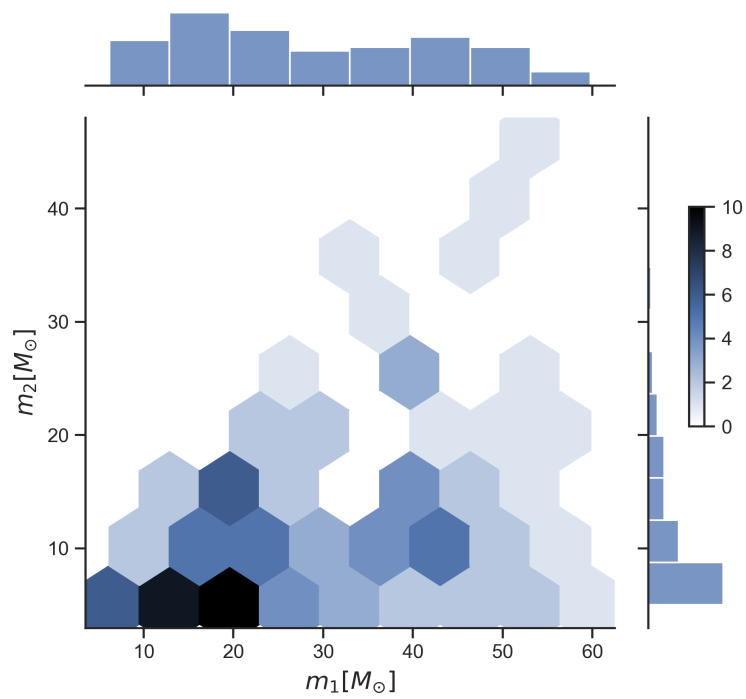


FIGURE 3.3: Mass range for individual BBH mass used in **Case2**.

overall amplitude is *stronger* than it would be in a more realistic simulation since I deliberately chose highest-SNR BBH signals from the cosmological distribution to have the clearest demonstration of the effect of residual-noise projection. I employ a redshift independent power-law distribution for both intrinsic masses with a power-law index $\alpha = -1.6$, motivated by the second observation run (O2) of aLIGO and AdV detectors [18], constraining the individual masses to lie within the range $5\mathcal{M}_\odot \leq m_2 < m_1 \leq 60\mathcal{M}_\odot$. This leads to the sample of 100 BBH masses shown in Figure 3.2 and 3.3 for Case1 and Case2 respectively. More detail about the parameters used for studies is given in Table 3.1.

The sampled redshift and total mass of the signals used in Case1 and Case2 are shown in Figure 3.4 and 3.5 together with smoothed distributions derived from these samples (which explains why there is no low-mass bound of the mass distribution). The only difference between these two distribution is the choice of redshift distribution for BBH signals.

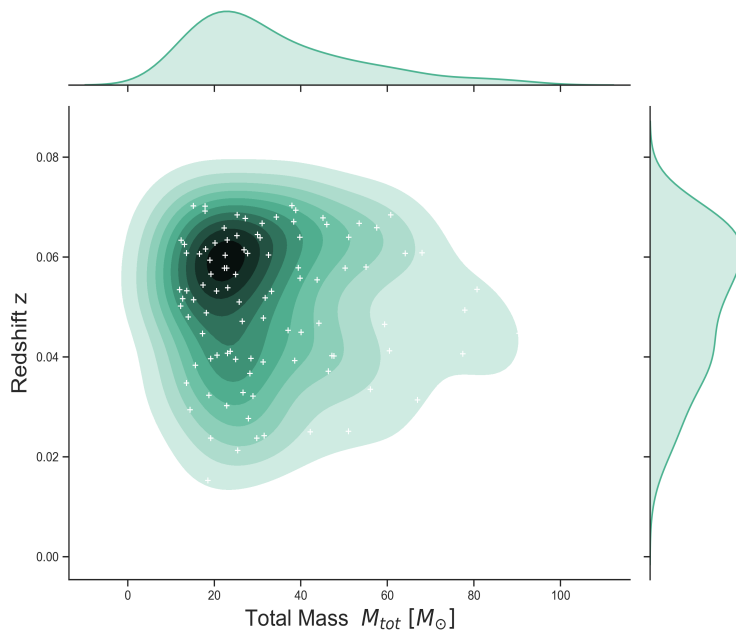


FIGURE 3.4: Distribution of total mass M and redshift z of the 100 BBH signals used in **Case1** analysis. Highest-SNR BBH signals are chosen for clearest possible demonstration of the projection method to mitigate the astrophysical foreground.

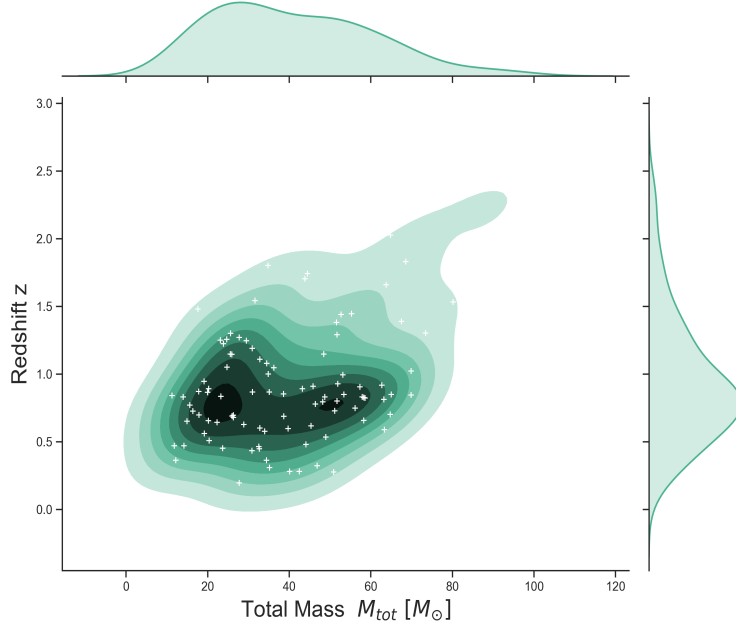


FIGURE 3.5: Distribution of total mass M and redshift z of the 100 BBH signals with lower SNR values (i.e. $\text{SNR} > 10$) are chosen for the demonstration of projection method to mitigate the astrophysical foreground in **Case2**.

In the next step, I subtracted the best-fit estimated waveform for all identified binaries from the data stream of the detector to reduce the foreground of detected CBCs to a threshold level such that only instrumental noise and residual noise from unresolved binaries remains in addition to SCGWB. After subtraction of the best-fit waveform, since the maximum likelihood (best-fit estimated) waveform does not perfectly match the true signal due to the instrumental noise, residual noise corresponding to the mismatch between the true waveform of BBH and the best-fit estimated waveform remains. This residual noise would be too high and still mask an SCGWB [91].

In the last step, I applied the projection method to remove the residual noise left after the subtraction of the best-fit waveform. These residual errors due to the residual noise from unresolved binaries plus instrumental noise are calculated by using Fisher-matrix formalism. As a result, there would be only the SCGWB and the instrumental noise in the data stream of the detector. Hence, one can

apply theoretical models or can perform an un-model search for the SCGWB searches.

3.3 Matched filtering and Fisher matrix

This section focuses on the importance of Fisher-Information Matrix (FIM) (see Appendix Section C.3) in the subtraction-noise projection method. Fisher matrices are widely used in the GW data analysis to characterize the parameter estimation based on the Taylor expansion of likelihood function around the true source parameters of the detected signals [162]. With the current generation GW detectors, it is possible to have multi-event detection, making it more challenging to extract information about the detected signals and their properties. Therefore, it is of great importance to improve the accuracy of data extraction methods. For such purpose, Fisher matrices become useful as they are closely linked to matched filtering providing a simplified view into its properties. Matched filtering techniques use an inner product of the detector data with a theoretical waveform template depending on a set of parameters.

I used Fisher matrices for the signal analysis in Subsection 3.3.2 and 3.5.3, for the formalism of the projection operator and to project out the subtraction residuals in Section 3.6.

3.3.1 Binary parameters

A set of physical parameters are required to describe the GW signal emitted by coalescing binary objects. Coalescing binaries, the first source of GWs, depend on fifteen parameters in total (including intrinsic and extrinsic parameters), characterizing the dynamics of a binary object, the waveform of emitted signal and relation of coalescing binary source to the GW detector. In particular,

the merger of the BBH is described by eight intrinsic parameters, the individual masses m_i and their two spin vectors \vec{a}_i . Apart from these intrinsic parameters there are seven extrinsic parameters required to further describe a BBH, namely: right ascension ϕ and declination θ (providing the sky localization information), luminosity distance D_L , orbital inclination θ_{jn} , polarization angle ψ (characterizing the orientation of coalescing binary), coalescence time t_c and orbital phase ϕ_c at time of coalescence t_c . Beside these fifteen parameters, the eccentricity of binary objects is also a potential observable parameter; still, there is no experimental evidence so far about the eccentricity of BBH in GW detectors. With the detection sensitivity in lower frequency band (2 Hz - 10 Hz), the eccentric BBH encounter would be easy to detect with ET and CE detectors as the waveform amplitude of eccentric BBH signal is larger than that of quasi-circular BBH during the inspiral evolution [62].

The GW signal detected by the GW detectors consists of merger signal which carries the information about the physical parameters of the binary objects in addition to instrumental noise of the detector. By using the theoretical waveform models (see Appendix A) one can extract the information about these physical parameters up to a certain level of accuracy using Bayesian inference approach to perform the parameter estimation. A list of BBH parameters used to create a uniform distribution of BBHs over the cosmological scale is given in Table 3.1.

3.3.2 Fisher matrix for signal analysis

The probability of two BBH signals to overlap in time in ET data is relatively high but depends on details of the mass distribution [137]. Lower-mass signals last longer (up to a few minutes) and if present in a greater number would lead to more frequent overlap. However, it is unlikely that the number of detectable BBH signals with third-generation detectors will be impacted significantly by the presence of other signals, which is in contrast to the situation described for future

Variable	Form	Range	Motivation
Primary mass (m_1)	const	$[5, 60] M_\odot$	Uniform BBH
Secondary mass (m_2)	const	$[5, 60] M_\odot$	Uniform BBH
Primary spin magnitude (a_1)	const	$[0, 0.8]$	Uniform
Secondary spin magnitude (a_2)	const	$[0, 0.8]$	Uniform
Polar angle between primary spin and Orbital Angular momentum ($tilt_1$)	$\propto \sin(tilt_1)$		aligned-spin
Polar angle between secondary spin and Orbital Angular momentum ($tilt_2$)	$\propto \sin(tilt_2)$		aligned-spin
Azimuthal angle between primary and secondary spin (ϕ_{12})	const	$[0, 2\pi]$	Uniform in orientation
Azimuthal angle between total angular momentum and orbital angular momentum (ϕ_{jl})	const	$[0, 2\pi]$	Uniform in orientation
Declination angle (θ)	$\propto \cos(\theta)$	$[0, \pi]$	Uniform in sky
Ascension angle (ϕ)	const	$[0, 2\pi]$	Uniform in sky
Orbital Inclination (θ_{jn})	$\propto \sin(\theta_{jn})$	$[0, \pi]$	Uniform in orientation
Polarization (ψ)	const		Uniform in orientation
Coalescence phase (ϕ_c)	const	$[0, 2\pi]$	Uniform in phase
Luminosity Distance (D_L)	const		Uniform in volume
geocent time	const	4 sec	signal window

TABLE 3.1: Summary of source parameters used to define the distribution of BBHs used in the study. Out of these source parameters only m_1 , m_2 , θ_{jn} and D_L are used to perform the BBH parameter estimation.

space-borne GW detectors where the foreground itself acts as excess noise [76, 73]. It is, therefore, enough to consider the impact of the astrophysical foreground on the correlation measurements between detectors, which is addressed by the subtraction-noise projection method discussed in the following using Cutler and Harms [73].

The basis of the subtraction-noise projection method is the expansion of parameter errors or likelihood functions with respect to the inverse of the SNR of signals, which means that this approach works better for high-SNR signals. For a Gaussian instrumental noise, the metric of the statistical manifold is defined by the Fisher matrix whose components take the form (from Equation (C.18))

$$\begin{aligned}\Gamma_{\alpha\beta} &= \langle \partial_\alpha h(\vec{\lambda}) | \partial_\beta h(\vec{\lambda}) \rangle \\ &= 4 \int_0^\infty df \frac{\Re(\partial_\alpha h(f) \partial_\beta h^*(f))}{S^n(f)},\end{aligned}\tag{3.1}$$

where $\vec{\lambda}$ is the vector of model parameters. The scalar product requires an estimate of the instrument-noise spectral density $S^n(f)$. The Fisher matrix is expressed as a scalar product $\langle \cdot | \cdot \rangle$ between derivatives of the waveform model with respect to model parameters $\partial_\alpha = \partial / \partial \lambda^\alpha$. The Fisher matrix can be interpreted as a metric on the curved template manifold defined by the waveform model $h(\vec{\lambda})$. The template manifold is a sub-manifold of the sampling space whose points describe realizations of detector data including instrument noise and signals not described by $h(\vec{\lambda})$ (see Figure 3.7).

For a signal model $h(\vec{\lambda})$ to be fully parameterized a set of λ^α parameters are needed. The entire analysis is fully based on the signal model, as there is no real data. Therefore, it is crucial to differentiate between the simulated signal h , which adds to the instrumental noise n to form output s of a GW detector, and the best-fit estimated signal.

The probability for noise to have some realization n_0 when noise is Gaussian, given by [74]

$$p(n = n_0) \propto e^{-\langle n_0 | n_0 \rangle / 2}, \quad (3.2)$$

where weighting is performed by defining an inner product for two real valued signals $g(t)$ and $h(t)$ as given by

$$(g|k) = 4\Re \int_0^\infty df \frac{\tilde{g}(f)^* \tilde{k}(f)}{S_n(f)}, \quad (3.3)$$

where $\tilde{g}(f)$ and $\tilde{k}(f)$ are the Fourier transform of signals $g(t)$ and $h(t)$, $*$ represents the complex conjugate, and $S_n(f)$ is one-sided noise power spectral density.

For a GW detector to measure the overall output s , with an actual incident waveform h conditioned on waveform parameters λ^α in addition to the instrumental noise n_0 , the Gaussian probability density is defined as

$$p(s) \propto e^{-\langle s-h | s-h \rangle / 2}. \quad (3.4)$$

Consequently, for a measured GW signal s , if the best-fit template waveform \hat{h} with parameters $\hat{\lambda}$ maximizes the likelihood i.e., if it minimizes the quantity $\langle s - \hat{h} | s - \hat{h} \rangle$ in Equation (3.4) (which is log-Gaussian probability of residual after the best-fit waveform has been subtracted) then for signals with sufficiently high SNR, \hat{h} fulfils the following equation [74]

$$\langle s - \hat{h} | \partial_\alpha \hat{h} \rangle = \langle n + (h - \hat{h}) | \partial_\alpha \hat{h} \rangle = 0, \quad (3.5)$$

for all derivatives ∂_α . The vanishing of first scalar product in Equation (3.5) means that the line in sampling space connecting the point s with the best-fit

waveform \hat{h} is perpendicular to the template manifold, i.e., the best-fit waveform is obtained by determining the template on the manifold with minimal distance to s (Figure 3.7). The vanishing of the second scalar product means that the residual noise $\delta h = \hat{h} - h$ (Equation (3.13)) is equal to the component of the instrument noise tangent to the manifold at the point of best-fit \hat{h} .

In a GW detector, a GW signal h with a different noise realization will lead to different best-fit parameters and corresponding estimated waveforms. As mentioned earlier, the Fisher matrix works accurately for high SNR signals; therefore, the best-fit parameters will have Gaussian distribution centred at true physical parameters. For λ^α being the true source parameters of a binary object and $\hat{\lambda} = \lambda^\alpha + \delta\lambda^\alpha$ being the best-fit parameters in a particular choice of noise realization, the parameter estimation errors for high SNR case will have a Gaussian probability distribution of likelihood function as

$$p(\delta\lambda^\alpha) = \mathcal{N} e^{-(1/2)\Gamma_{\alpha\beta}\delta\lambda^\alpha\delta\lambda^\beta}, \quad (3.6)$$

where $\mathcal{N} = \sqrt{\det(\Gamma_{\alpha\beta}/2\pi)}$ is the normalization factor and $\Gamma_{\alpha\beta}$ is Fisher matrix (see Equation (3.1)). Parameter estimation errors can be drawn from this distribution to substitute a computationally costly posterior sampling (see Equation (C.17) (C.18)).

The best-fit parameter estimation in my studies are based on the computationally costly posterior sampling using Bayesian inference (which provides the robust best-fit estimation of source parameters) (see Appendix Section C.2), Figure 3.6 represents the mismatch between true source parameters (parameter priors used to inject into detector network) and best-fit estimated parameter for BBH parameters luminosity distance D_L and inclination angle θ_{jn} .

For high-SNR case (which is true for Equation (3.6) and for posterior sampling with Bayesian inference), variance and covariance matrix of parameter errors $\delta\lambda$ can be written as [162]

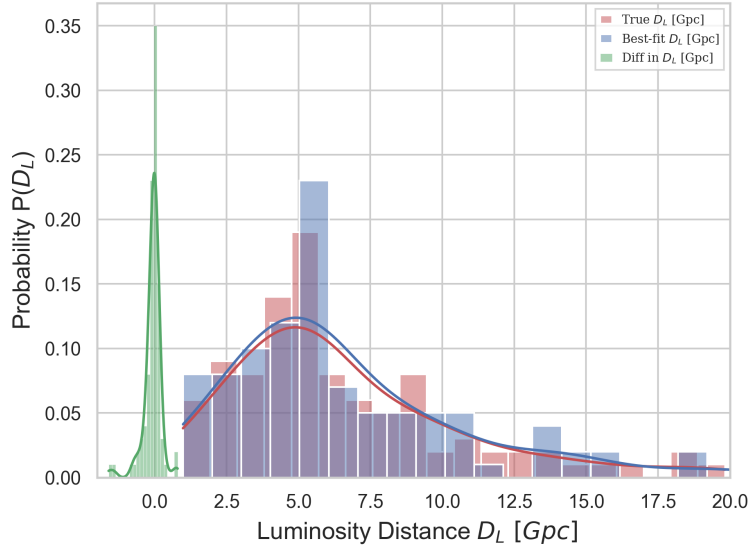
$$\overline{\delta\lambda^\alpha\delta\lambda^\beta} = \Gamma^{\alpha\beta} + \mathcal{O}(\text{SNR})^{-1}, \quad (3.7)$$

where $\Gamma^{\alpha\beta}$ is inverse of Fisher matrix and represents the co-variance i.e. defines variance of α and β with each other.

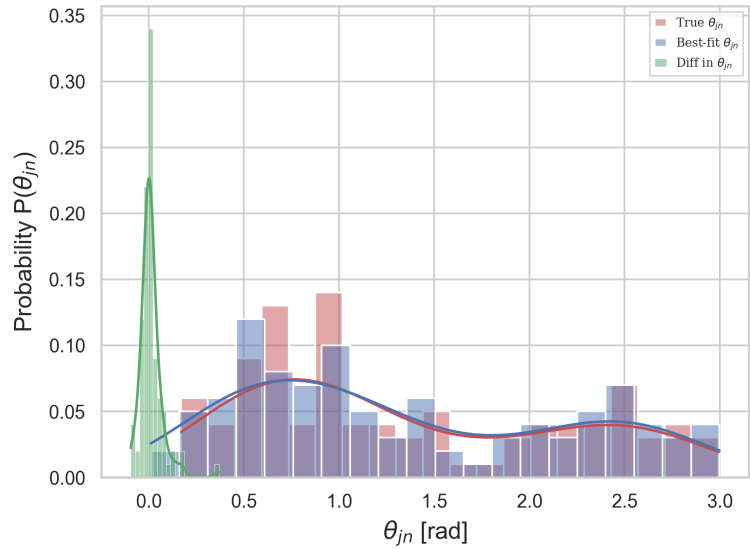
3.4 CBC waveform template

The GW signal waveforms are pivotal and require precision in the knowledge of expected waveforms for the observation and characterization of CBCs with current and future GW detectors. The signal waveform with a set of parameters obtained from theoretical studies of expected signals in analytical approximation, i.e. PN and NR approach enables us to search for IMR phase of CBCs coherently (Appendix A).

Real challenges lie in the construction of a waveform template as they can increase the false alarm rate further posing a data analysis and computational challenge for CBC signal searches. An ensemble of waveform models form a waveform template bank parameterized by the parameters of the binary object. The waveform template bank is constructed from matched filtering (cross-correlation between detector data and waveform template) with a careful discrete sampling of intrinsic parameters. If not, the loss of SNR will lead to a mismatch between template and signal parameters. The reasons behind loss of SNR could be phase mismatch, i.e. inaccurate modelling of waveform or the discreteness of waveform template bank. Thus intrinsic parameters require special attention to define the source dynamics and preciseness in sampling over the parameter space to avoid



(A)



(B)

FIGURE 3.6: Parameter estimation error distribution for luminosity distance D_L (in Figure 3.6a) and orbital inclination angle θ_{jn} (in Figure 3.6b) between the true source parameters (red curve) and best-fit estimated parameters (blue curve) for BBH signals used in **Case2**. The green spikes give the mismatch between the true source parameters and the best-fit estimated parameters. Wider the green spikes are, large would be the parameter estimation errors (see Equation (3.12)). Consequently, larger would be the residual noise (Equation (3.13)).

the mismatch between the template and signal parameters. Besides, a template bank also depends upon the noise PSD of the detector. In case of more than one detector, we would have more than one PSD to handle. Thus it is better to have a single effective template bank which can be obtained by combining the PSDs of two or more GW detectors [31, 145, 83].

The choice of the waveform is going to be predominant in future GW detectors ET and CE. Being sensitive in lower frequencies in between 2-10 Hz and with increased detection rate, these detectors would be able to observe all three phases of a binary waveform, i.e. IMR phase, making it difficult to choose a waveform for an individual signal and further making it challenging to construct a waveform template bank to identify all the GWs signals. Further, it is demonstrated in [146] that by incorporating several optimizations to waveform template banks one can shrink the hybrid template banks by 34% for particular binary systems leading to the more accurate choice of a waveform to the GW signals. It is going to be a dominating factor in data challenges with third-generation GW detectors, and the effectiveness of the waveform template bank will optimize the future CBCs searches and will help us to improve our method.

The signals are generated and recovered with the "IMRPhenomPv2" waveform (see Appendix A). The waveform model provides simplicity to study the subtraction and the noise projection method, without considering the difficult choice of the waveform (i.e. models with reduced parameter space, e.g. surrogate waveform models, models including higher modes, eccentricity and spin parameters). Besides, most of the waveform models used by LVC members are not good enough to be used below the lowest sensitive frequency value (~ 20 Hz) of aLIGO and AdV detectors.

3.5 Sources of confusion noise

The question is, what can contribute to the confusion noise in ET and CE, which can further make SCGWB searches more difficult? With the increase in sensitivity by a factor of 10 in comparison to current GW detectors, third-generation GW detectors will detect all the binaries up to redshift $z \geq 10$. In addition to resolvable signal (non-overlapping and separable both in time or frequency domain, very high SNR signals) there would be signals which are weak and unresolvable sources (low SNR signals, challenging to identify individually, difficult to estimate the source parameters) leading to the first type of confusion noise. Besides this, even identified BBH would also contribute to the second type of noise due to subtraction error referred to residual noise. To answer the question, I will discuss the contribution to confusion noise in detail in next sections.

3.5.1 Overlapping in binary signals

As discussed in Section 3.2 non-Gaussian and non-stationary BBH does not contribute to overlapping in the chirps in the same data segment of duration 4096 s. However, the overlap is unlikely but certainly possible for BBH detection in the ET and CE frequency band. Besides, if BBH has eccentricity and quasi-normal modes which are going to be accessible with third-generation GW detectors, we will see an overlap between the different BBH signals. If GW signals have sufficiently high SNR to be detected with negligible influence on their parameter estimation from other signals potentially present at the same time then overlapping between binary signals can be taken care off. I will focus on how BBH mergers can lead to substantial overlap. For a given GW detector with overall output $s(t)$, a sum of instrumental noise $n(t)$ and the sum over all BBH signals $h_j(t)$ (where index j gives the total number of BBH signals), is given as

$$s(t) = n(t) + \sum_j h_j(t). \quad (3.8)$$

Then optimal matched filtering of data for a signal waveform $h_k(t)$ is equivalent to the inner product (Equation (3.3)), which can be written as

$$\langle s|h_k \rangle = \langle n|h_k \rangle + \sum_{j \neq k} \langle h_j|h_k \rangle + \langle h_k|h_k \rangle. \quad (3.9)$$

From Equation (3.9), the waveform overlap happens when two signals h_j and h_k have same frequency, i.e. $f_j(t_0) = f_k(t_0)$ for a particular time interval t_0 of a GW detector. Consequently, while performing signal detection analysis, these two GW signals can resemble each other, i.e. they are indistinguishable in the presence of detectors instrumental noise, thus contributing to confusion noise [73, 91]. To detect various signals and differentiate between them in the data stream of a GW detector the root-mean-square value of the third term on right-hand-side of Equation (3.9) should be greater than the first two terms on the right-hand side.

3.5.2 Overlapping in waveform

The choice of the waveform template can further affect the subtraction-noise projection method and contribute to residual noise due to degeneracy in the parameters space of binary signal. Since the template bank consists of a large number of waveform models, during the signal detection, two waveforms resembling each other are difficult to distinguish in presence of instrumental noise. Therefore, GW signals can be mutually degenerate, i.e. different source parameters conjunction can describe the same waveform model (and vice-versa), This can cause an enormous uncertainty level in the best-fit parameter estimation,

consequently increasing the residual noise [34, 126]. Various methods are being developed to increase the effectiveness of the waveform template bank, which will help us overcome this issue [145]. Being sensitive in the low-frequency regime, in third-generation GW detectors ET and CE, this issue will also pose a challenge not only for BBH but also for BNS signal detection.

3.5.3 Subtraction of best-fit waveforms

Before applying the subtraction-noise projection method to search for an SCGWB, we need to individually identify all the BBH signals in the data stream of the detector. However, the best-fit parameter estimation for each binary will be different from the true source parameters due to the instrumental noise. Therefore, the estimated best-fit waveform will differ from the actual source waveform [74].

In reality, a GW detector measured the data $s = h(\lambda^\alpha) + n$. To find a best-fit waveform $h(\hat{\lambda}^\alpha)$ corresponding to the GW signal h in the detector's data stream, I calculate the best-fit parameters $\hat{\lambda}^\alpha$ which can be represented by drawing a normal from s to the manifold of the best-fit estimated waveform $h(\hat{\lambda}^\alpha)$ (which corresponds to the shortest normal between the best-fit and the S on the manifold.) (see Figure 3.7).

The size of the mismatch (or errors) between the true source parameters λ^α and the best-fit estimated parameters $\hat{\lambda}^\alpha$ are calculated by using a simple approach. Consider a GW signal waveform h in the detector's data stream which depends upon N_P , the total number of parameters λ^α (where index $\alpha = 1, 2, \dots, N_P$) going into the waveform model. The best-fit parameters satisfy the following relation [74]

$$\langle \partial_\alpha h(\hat{\lambda}^\alpha) | s - h(\hat{\lambda}^\alpha) \rangle = 0. \quad (3.10)$$

The scalar product in Equation (3.10) can also be used to define the SNR of a signal

$$SNR = \sqrt{\langle h|h \rangle}. \quad (3.11)$$

The leading order terms of SNR^{-1} expansion of the covariance of parameter estimation errors is given by Equation (3.7). It is also possible to express the leading order parameter estimation errors $\delta\lambda$ (difference between true and best-fit parameters $\delta\lambda \equiv \hat{\lambda} - \lambda$) in terms of specific instrumental-noise realization, thus we will have

$$\delta\lambda^\alpha \equiv \hat{\lambda}^\alpha - \lambda^\alpha \approx \Gamma^{\alpha\beta} \langle n | \partial_\beta \hat{h} \rangle, \quad (3.12)$$

where $\delta\lambda^\alpha$ is the sum of all statistical contributions $\delta_n \lambda^\alpha$ due to the detector's noise and a contribution from template inaccuracy $\delta_{temp} \lambda^\alpha$. [74] provides a more detailed approach to study the parameter estimation error due to inaccurate waveform template defined in Equation (3.12). [65] also addresses the issue of waveform errors in parameter estimation. The uncertainty in $\delta\lambda^\alpha$ is proportional to SNR^{-1} . In a similar manner, the estimated best-fit waveform \hat{h} will differ from the true waveform h as follows

$$\delta h \equiv \hat{h} - h = \partial_\alpha h \delta\lambda^\alpha + \mathcal{O}(\delta\lambda)^2. \quad (3.13)$$

With the use of Equations (3.1), (3.12) and (3.13), one can calculate the norm-squared subtraction residuals averaged over noise realizations, given by

$$\overline{\langle \delta h | \delta h \rangle} = \langle \partial_\alpha h | \partial_\beta h \rangle \overline{\delta\lambda^\alpha \delta\lambda^\beta} = \Gamma_{\alpha\beta} \Gamma^{\alpha\beta} = N_P. \quad (3.14)$$

From Equation (3.14), it is easy to realize that norm-squared of subtraction residuals is independent of SNR but depends only on the number of physical parameters used to define a GW signal waveform. Together with Equation (3.11), Equation (3.14) tells us that on average, the amplitude of signal after the subtraction of its estimated best-fit waveform is reduced by a factor given by

$$\frac{\delta h}{h} \equiv \frac{\sqrt{N_P}}{SNR}, \quad (3.15)$$

which also means that residuals are independent of the SNR of signal (again, in the approximation of large SNR). How accurately we are subtracting best-fit estimated waveform from the data stream of a detector δh depends upon the choice of the waveform template and parameters used to describe the signal.

After the subtraction of the estimated best-fit waveform from the data stream, the sum of amplitude of detector's noise and the residual noise is smaller than that of detector's noise alone. To visualize this one can proceed as, for a GW detector sensitive in a particular frequency band $[f_{min}, f_{max}]$ running over an observation period T_{obs} , the noise will have a squared magnitude given by

$$\overline{\langle n|n \rangle} = 2f_{max}T_{obs}, \quad (3.16)$$

which represents the total number of data points sampled at $2f_{max}$ (Nyquist frequency). Now to further understand the scenario after subtraction of data $s - \hat{h}$, by using Equations (3.16) and (3.13), one will have

$$\begin{aligned}
 \overline{\langle s - \hat{h} | s - \hat{h} \rangle} &= \overline{\langle n + h - \hat{h} | n + h - \hat{h} \rangle} \\
 &= \overline{\langle n - \delta h | n - \delta h \rangle} \\
 &= \overline{\langle n_{\perp} + n_{\parallel} - \delta h | n_{\perp} + n_{\parallel} - \delta h \rangle} \\
 &= \overline{\langle n_{\perp} | n_{\perp} \rangle} \\
 &= 2f_{max}T_{obs} - N_P,
 \end{aligned} \tag{3.17}$$

where $n = n_{\perp} + n_{\parallel}$ are the perpendicular and parallel component of noise to the template manifold (see Figure 3.7). From Equations (3.17) and (3.4) it is easy to understand that subtraction of an estimated best-fit waveform \hat{h} does not take only the signal part out of the data stream of a detector, but it reduces it below the level of what noise contributes alone. Which means, while subtracting the estimated best-fit waveform \hat{h} , with the signal, subtraction also takes out a portion of the noise Equation (3.13). That is, the subtraction takes out the n_{\parallel} part of instrumental noise which is on the tangent plane of the manifold at the point of best-fit (see Figure 3.7).

To put it into a geometrical understanding, consider N_P being the number of source parameters used to parameterize the parameter space of a given waveform $h(\lambda)$, thus it would be a $N = N_P$ -dimensional manifold. This manifold is embedded into the vector space of all possibly measured BBH signals in the data stream of a GW detector. For s being the overall data of the detector, the estimated best-fit waveform $h(\hat{\lambda}^{\alpha})$ will lie close to the data s on the waveform template manifold in accordance to $\langle s - h(\hat{\lambda}^{\alpha}) | s - h(\hat{\lambda}^{\alpha}) \rangle$, providing the distance between the overall data of the detector and the estimated best-fit waveform. The vector from s to $h(\hat{\lambda}^{\alpha})$ is a normal to waveform template manifold at the point of best-fit parameters $\hat{\lambda}^{\alpha}$. Whereas the residual errors in parameter estimation given in Equation (3.12) will lie on the tangent to the waveform manifold (see Figure 3.7).

With the future GW detectors ET and CE, we will be able to detect almost all the BBHs emitting within their observation bands. Thus the entire astrophysical foreground coming from N_S sources would be

$$H(t) = \sum_{l=1}^{N_S} h_l(t), \quad (3.18)$$

with each BBH signal $h_l(t)$ being described by N_P parameters, the parameter space of complete astrophysical foreground would have the dimension $N_P \times N_S$. Therefore the norm-squared of the residual of this foreground is

$$\overline{\langle \delta H | \delta H \rangle} = N_P \times N_S. \quad (3.19)$$

It is easy to show that on average

$$\frac{\delta H}{H} \approx \frac{\delta h}{h}, \quad (3.20)$$

which means that the fractional reduction in the amplitude of a BBH signal is same as that of the entire astrophysical foreground assuming that almost all signals are detected with sufficiently high SNR. Since the foreground consists of N_S number of sources which could be $10^5 - 10^6$ BBH, there would be overlapping in the BBH signals and degeneracies in the parameters of BBH. The possibility of the existence of degeneracies in the parameter space does not mean that it would be difficult to subtract the foreground of these sources. However, it implies that the dimensionality of parameter space will reduce in comparison to the original number of parameters which are used to define the parameter space. As a result, using a fewer number of parameters N'_P one can define a new parameterization which will lead to the following result from Equation (3.19)

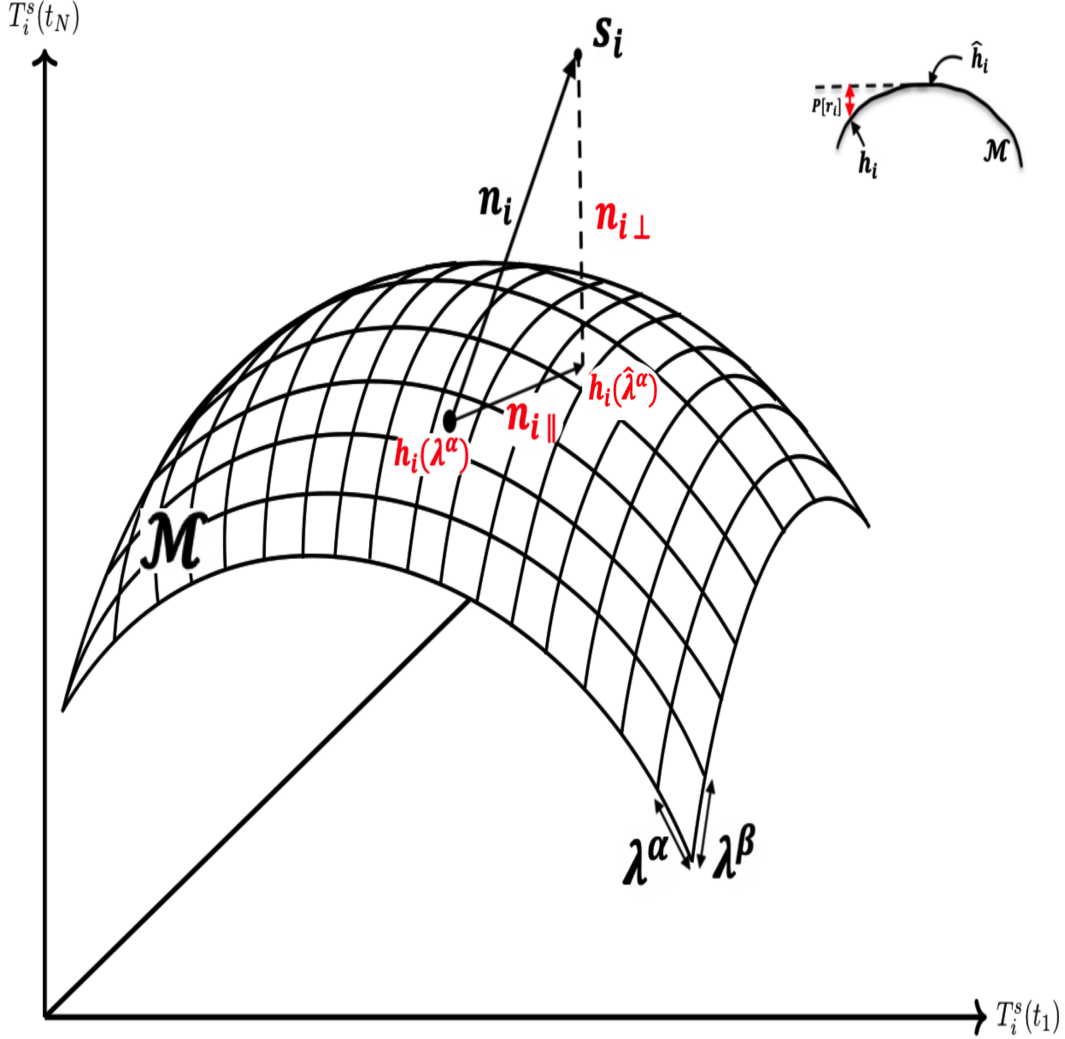


FIGURE 3.7: Figure showing the template manifold \mathcal{M} of all physical waveforms embedded into the vector space \mathcal{V}_i of all signals measured by GW detectors. The vector space is represented in two dimensional space by axis $T_i^s(t_1)$ which gives all the GW signals observed by GW detectors at time t_1 while axis $T_i^s(t_N)$ gives the total signals observed at different times t_N within the observation duration T_{obs} . The vector space S_i represent the output of i^{th} GW detector, n_i is the instrumental noise of the GW detector, $n_{i\perp}$ and $n_{i\parallel}$ are the component of residual noise remained after the subtraction of estimated best-fit waveforms. On the manifold \mathcal{M} , points $h_i(\lambda^\alpha)$ and $h_i(\hat{\lambda}^\alpha)$ give the location of true waveform and estimated best-fit waveform defined by their respective parameters. λ^α and λ^β are the binary source parameters provide with the parameter space for a waveform model and locate them on the manifold \mathcal{M} of all possible waveforms. The top right-hand side gives the enhanced view of projection residual on the curved manifold.

$$\overline{\langle \delta H | \delta H \rangle} = N'_P \times N_P. \quad (3.21)$$

3.5.4 Waveform model systematic

Source parameter extraction of a GW signal from a coalescing BBH requires a full Bayesian analysis over the parameter space. This includes evaluation of the multi-dimensional likelihood function; consequently, each waveform generated needs to be accurate to precisely extract the parameters. Currently, available waveform models for CBC signal searches are based on PN, NR or EOB methods. These waveform models are constructed with such an accuracy that systematic errors are less than the statistical errors for current GW detectors [110, 133]. However, with the upcoming upgrades to current GW detectors and the proposed future-generation ground-based detectors ET and CE, the sensitivity level for these detectors will increase. With this improvement the GW detections will also improve, and the SNR of local BBH will also increase reducing the statistical errors. As soon as these statistical uncertainties approach systematic uncertainties of the GW signal biasing in source parameters will appear making future GW observation unreliable. Consequently, we need new and improved waveform models to achieve the detection accuracy.

Since different waveform models differ from each other in their approach to treat BBH signals, there would be possible systematic uncertainties in the estimation of source parameters, i.e. in addition to parameter estimation errors Equation (3.12) there would be a contribution coming from the choice of waveform [74, 127, 113]. For testing such systematic errors due to waveform model, one can repeat the Bayesian analysis for a different choice of waveforms which can provide with the detailed and robust best-fit parameters, statistical errors in SNR, the response of detector network and the comparison of the estimated parameters between waveform models. Such an analysis was followed by using

IMRPhenomPv2 waveform in addition to other waveform models for GW150914 observation to understand the impact of waveform model systematic [11] and how they can impact the GW signal observation. The waveform model difference can be sufficient enough to significantly bias the parameter inference for any astrophysical binary object of interest [170]. These systematic differences between waveform models can be analyzed by identifying the regions of disagreement in parameter space. The biasing in waveform models can make an impact in multiple CBC events parameter inference. A similar study has been done for NS-BH [60, 98] and BNS [148, 149].

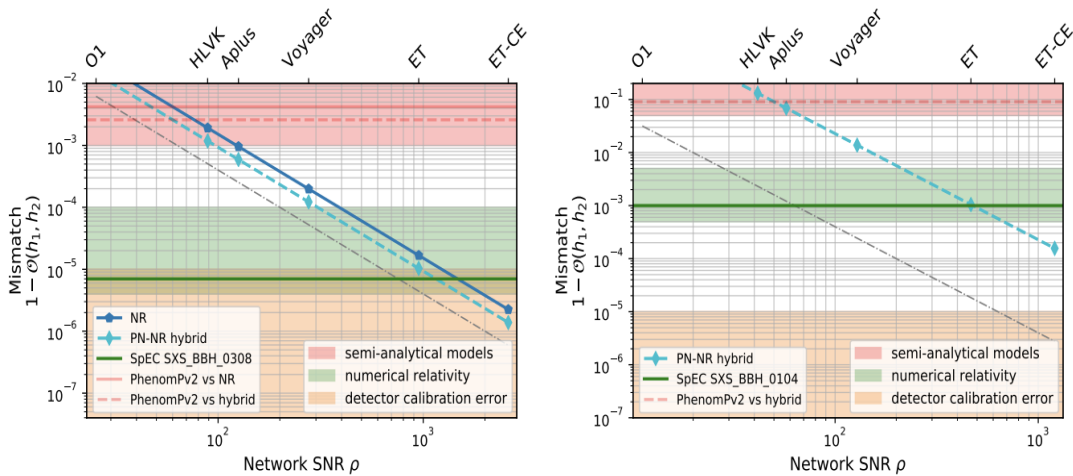


FIGURE 3.8: Predicted waveform accuracy for current GW detectors, their future upgrades (Aplus and Voyager) and proposed GW detectors (ET and CE) for two binaries *left: SXS BBH 0308*, and *right: SXS BBH 0104*. Each panel shows the mismatch in SNR for a GW detector. The solid line represents the NR signals, and dash lines give hybridized PN-NR signals in the inspiral phase. The blue lines with data points show the mismatch, which falls with the rise in SNR of the binary signal. The dashed-dotted grey line shows the systematic errors from waveform inaccuracy which are smaller than statistical errors (Figure from [133]).

Now for third-generation detectors, the mismatch errors between waveform models can be reduced by a magnitude of three whereas for NR waveform it can be reduced by order of one (see Figure 3.8). As a result, the residuals left after the subtraction of estimated signal, best-fit waveform template with significant SNR leads to a Bayes factor of 10^{11} [133], furthermore to imprecise deviations.

For two indistinguishable waveform models h_1 and h_2 with a given PSD and SNR, the mismatch is given as

$$1 - \mathcal{O}(h_1, h_2) < \frac{D}{2SNR^2}, \quad (3.22)$$

where $\mathcal{O}(h_1, h_2)$ is the maximized overlap function used to maximize the inner product between waveform models h_1 and h_2 (inner product depends upon the time and phase shift between two waveforms) and measures the correlation between given waveform models

$$\mathcal{O}(h_1, h_2) = \max \frac{\langle h_1 | h_2 \rangle}{\sqrt{\langle h_1 | h_1 \rangle \langle h_2 | h_2 \rangle}}. \quad (3.23)$$

In Equation (3.22) D is an unknown pre-factor given by

$$D = 2\rho_{eff}^2 [1 - \mathcal{O}(h_{bf}, h_{true})(\lambda)], \quad (3.24)$$

$$\rho_{eff} = \frac{1}{\sqrt{2(1 - \mathcal{O}(h_{bf}, h_{true}))}}, \quad (3.25)$$

where ρ_{eff} is the SNR of detector network at which systematic and statistical errors become comparable, i.e. below this SNR level, it would not be easy to distinguish between the true and modeled waveform. Equation (3.22) and (3.24) provide us with the SNR beyond which the parameter estimation leads to biased posterior distribution for a BBH signal. Thus from Equation (3.14), if $\langle \delta h | \delta h \rangle < 1$, the systematic errors from the mismatch would be smaller than $1 - \sigma$ statistical errors.

Since the pre-factor D is unknown, it can be calculated from biased parameters of a BBH signal. In a similar manner to the Fisher matrix, pre-factor D

is also limited to high SNR signals. Therefore to evaluate D and enhance the efficiency of the method, the following steps can be followed

1. Calculate the posterior distribution for a sequence of detector networks for BBH signals (which I followed while performing the parameter estimation).
2. Compute the systematic and statistical errors from the posterior distribution,
3. SNR ρ_{eff} estimation,
4. Compute Equation (3.22),
5. Calculate for Equation (3.24) .

3.6 Projection of subtraction residuals

In this section, I define a projection operator which is used to clean the detector's data stream from the subtraction residuals, remained after the subtraction of the BBH foreground. The results of Section 3.3 and 3.5 form the base for projection method. As shown in Equation (3.10), the residual noise is not completely random but lies at the point of best-fit and is tangent to the waveform manifold. The strategy of the projection method is to apply a projection operator to the residual data $r = s - \hat{h}$ removing all of its components. To understand further how the projection method works, I used the concept of differential geometry (see Subsection 3.6.2) to the projection method for the projection of residual noise.

3.6.1 Projection operator and residual noise

This subsection follows the strategy to effectively project out the residual errors remained after the subtraction of the best-fit waveform of BBH signals

from the detector's data stream. Matched filtering helps to define the vector space \mathcal{V} of all detectors output while all physically possible waveforms form the waveform template manifold \mathcal{M} , which is a sub-manifold within the vector space \mathcal{V} .

If we consider a waveform template manifold of all physically possible GW waveforms, embedded into the vector space of all possible measured signals by a GW detector, the residual noise in overall foreground $\delta H(t)$ is confined on the vector space of all signals which is tangential to the waveform manifold at the point of best-fits. Therefore the residual errors after subtracting the estimated best-fit waveforms can be expanded according to Taylor Series expansion given by

$$\delta H(t) = \partial_\alpha H(t) \delta \lambda^\alpha + \frac{1}{2} \partial_\alpha \partial_\beta H(t) \delta \lambda^\alpha \delta \lambda^\beta + \dots, \quad (3.26)$$

where $\alpha, \beta = 1, 2, \dots, N_P$ are the total number of parameters defining the parameter space for the overall foreground of BBH signals. The first term on the right-hand-side $\partial_\alpha H(t)$ is a linear combination of N_P wavefunctions. $\partial_\alpha H(t)$ has an unknown coefficient which can be determined by noise only (i.e. mismatch between the parameters values $\delta \lambda^\alpha$) and needs to be projected out of the detector's data stream. The projection needs to be done for all the signals in the data. Thus, the projection operator can be written as

$$P \equiv 1 - \Gamma^{\alpha\beta} |\partial_\alpha H\rangle \langle \partial_\beta H|. \quad (3.27)$$

The projection operator defined in Equation (3.27) has the properties of a quantum mechanical operator such as $P^2 = P$, which implies that the projection operator will eliminate all wavefunctions like $\partial_\alpha H(t) \delta \lambda^\alpha$. Furthermore, it is also crucial to understand how much of the detector data will be thrown away while

projecting out the residuals. To roughly estimate the loss in the detector data, consider that ET and CE will observe around 10^5 GW signals, where each signal is characterized by a set of 15 parameters. Then $N_P = 15 \times 10^5 \approx 10^6$ would be the parameter space, sampled at 2048 Hz with one year (10^7 s) of data observation, the fractional loss would be $10^6/10^{10} \approx 10^{-4}$, is a negligible fraction of detector data.

The dependence of uncertainties on the parameters $\delta\lambda^\alpha$ (on SNR^{-1}) can provide the information about how the amplitude of residual errors is SNR dependent. For a waveform template h at expected parameter estimation error $\langle\delta\lambda\rangle$, by using Taylor expansion around true signal $h(\lambda_0)$ with true source parameters λ_0 , we will have

$$h(\langle\delta\lambda\rangle) = h(\lambda_0) + \partial_\alpha h(\lambda_0)\langle\delta\lambda^\alpha\rangle + \partial_\alpha h(\lambda_0)\partial_\beta h(\lambda_0)\langle\delta\lambda^\alpha\rangle\langle\delta\lambda^\beta\rangle + \mathcal{O}(\text{SNR}^{-2}). \quad (3.28)$$

The first term on the right-hand side of Equation (3.28) is linear in SNR, the second term is independent of SNR, which is a combination of two variations in SNR. The first part of the second term is linear in SNR (i.e. derivative of waveform template $\partial h(\lambda_0)$) while the second part ($\langle\delta\lambda^\alpha\rangle$) is inversely proportional to SNR, thus making it SNR independent term. In contrast, the third term is proportional to the inverse of SNR. If we eliminate the first term and the second term of Equation (3.28) by subtracting and projecting out respectively from the detector data stream, we can reduce the signal strength by SNR^{-2} . By following Equation (3.14) one can see that norm-square of the third term in Equation (3.28) is independent of SNR but depends only on the total number of parameters used to describe a binary signal, which can also be subtracted from the data stream.

When applying the projection to the residual data of a detector i , from Equation (3.27) one obtains [154]

$$P[r_i](t) = r_i(t) - \Gamma_i^{\alpha\beta} \langle \partial_\beta \hat{h}_i | r_i \rangle \partial_\alpha \hat{h}_i(t), \quad (3.29)$$

which is written in the time domain, but it can also be applied in the Fourier domain. The residual $P[r_i]$ after projection corresponds to the instrument noise perpendicular to the template manifold plus a potential component of the true signal h_i that does not lie in the tangent space of the best-fit \hat{h}_i (see Figure 3.7 for a small doodle on the top right-hand side). This residual of the signal is non-vanishing only for curved manifolds and is suppressed by SNR^{-2} relative to the original signal. Comparing with Equation (3.5), it seems that the projection operator should not have any effect on the residual data $r_i = s_i - \hat{h}_i$ since the vector $|r_i\rangle$ is normal to the tangent space of the template manifold at the best-fit. However, this is not necessarily correct for various reasons.

First, the maximum-likelihood parameter estimates $\hat{\lambda}^\alpha$ are obtained using data from all detectors in the network. These parameter values determine the best-fit waveforms $h_i(\hat{\lambda}^\alpha)$ of each detector i in the network. These waveforms, however, are *not* the results of a normal projection of data vectors $|s_i\rangle$ onto the respective template manifolds. This will only be the case if maximum-likelihood estimates $\hat{\lambda}_i^\alpha$ are calculated for each detector separately. This means that subtracting $h_i(\hat{\lambda}^\alpha)$ from the data of all detectors leaves residuals in the tangent spaces, which can be projected out. Further, it also means that one needs to distinguish between the Fisher matrices $\Gamma_{i,\alpha\beta}(\hat{\lambda}_i^\mu)$ and $\Gamma_{i,\alpha\beta}(\hat{\lambda}^\mu)$, where the latter is obtained using the parameter estimates from coherent network analysis.

Let us consider the case where the maximum-likelihood estimations are done for each detector separately producing different best-fit parameters $\hat{\lambda}_i^\alpha$ for each detector i . Then, subtracting $h_i(\hat{\lambda}_i^\alpha)$ for all signals in the data reduces the astrophysical foreground by SNR^{-2} instead of SNR^{-1} . One might wonder where the subtraction residuals at order SNR^{-1} are, since clearly the misfit δh_i is still only suppressed by SNR^{-1} compared to the true signal $h_i(\lambda_0^\alpha)$. Here, the critical point

is that when subtracting a signal, the residual δh_i is already precisely cancelled by the component n_{\parallel} of the instrument noise that lies in the tangent space, which can be understood from Equation (3.10) when using $n = n_{\perp} + n_{\parallel}$. Therefore the perpendicular component of noise $r = n_{\perp}$ plus the residual noise from the astrophysical foreground are suppressed by $1/\text{SNR}^2$ and higher order terms. Another reason why best-fit residuals can be in tangent spaces of a template manifold, even if the best-fits are calculated for each detector individually, is that they are typically not the result of a likelihood maximization, but of a maximization of the posterior distribution, which depends on priors. In this case, the residual δh does not fulfil Equation (3.10), and residuals in tangent spaces remain to be projected out.

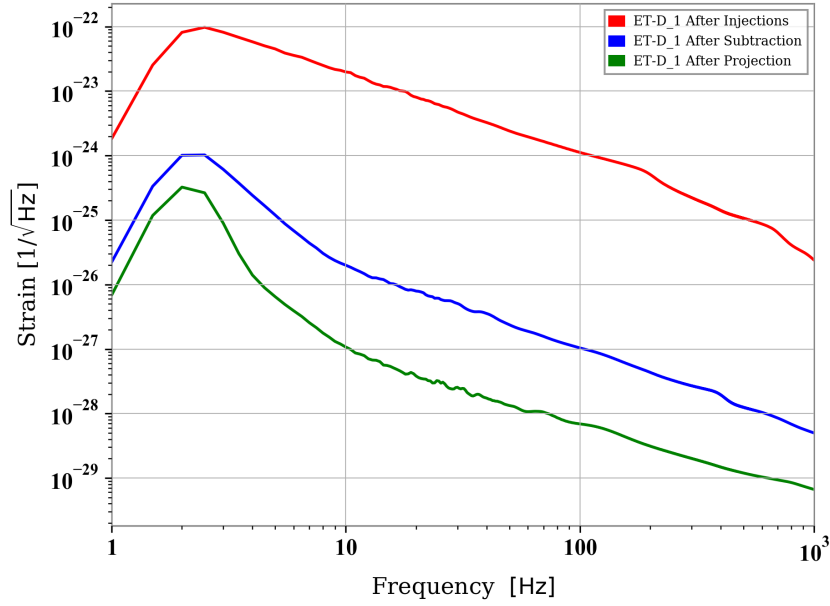
Finally, technical choices of a simulation can lead to additional residuals in tangent spaces. Often, parameter estimation by posterior sampling is computationally too expensive for studies with a large population of signals. In this case, past work made use of Equation (3.7) to define a Gaussian error distribution, from which parameter errors are drawn and added to the true signal parameters to obtain the maximum-likelihood parameters [91, 147]. The issue here is that the parameter errors are not consistent with a specific realization of the instrument noise. The best-fit waveform obtained in this way would not maximize the likelihood, and this leads to excess residual noise in tangent spaces, which is projected out [91]. This artefact can be avoided by using Equation (3.12) to obtain parameter errors, which is still under the assumption of a Gaussian likelihood, but at least consistent with a specific noise realization.

The quantity remained after subtracting the best-fit waveform from the data stream of a detector is

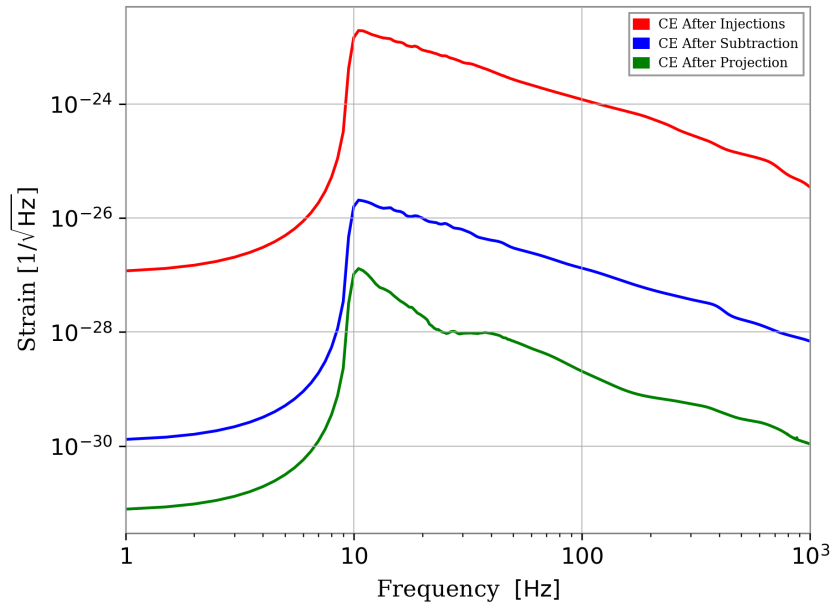
$$P[r_i] = n_{i\perp} + b_{i\perp} + \mathcal{O}\left(\frac{h_i}{\text{SNR}^2}\right), \quad (3.30)$$

represents a combination of intrinsic noise n_{\perp} of the detector and a SCGWB $b_{i\perp}$ (background is not defined on the Figure 3.7). Further by cross-correlation the data stream of two detectors we can remove the instrumental noise.

Now focusing back on the effect of the projection method on the foreground of BBHs injected into the detector data stream for each case as mentioned in Section 3.2, Figure 3.9a, 3.10a (for ET detector considering Case1 and Case 2) and Figure 3.9b , 3.10b (for CE detector in Case1 and Case2) shows the square root of PSD (i.e. amplitude spectral density) of the astrophysical foreground averaged over 1.3 years for Case1 and Case2, its subtraction residual, and the spectrum after the projection of the residual noise. The difference between the plots for CE (10 Hz as lowest frequency value) and ET (2 Hz as lowest frequency value) below 10 Hz is due to the difference between lowest frequency values. In these plots, the time series is simulated without instrument noise to demonstrate the full potential of the projection method. The posterior sampling was of course done including instrument noise, and included data from CE and the full ET triangle. In Case1 for ET and CE detector, the simulated astrophysical foreground have sufficiently high SNR BBH signals (see Section 3.2 Case1) to be able to neglect residuals at order SNR^{-2} . While in Case2, I have BBH signals with the SNR threshold $SNR > 10$ to check the effectiveness of projection method. Furthermore, one needs to consider the possibility that some low-SNR signals are not detected by ET, which gives rise to additional contributions to residual noise that I do not consider in this study (see [137, 147] instead). However, still, studies are undergoing to test the effectiveness of the subtraction-noise projection method for the extreme low SNR ($SNR < 2, 3, 5$) BBH signals. These studies will provides us with the minimum value on the SNR of BBH signals beyond which it would be impossible to use the subtraction-noise projection method. It is interesting to observe that the spectra change their shape after applying the subtraction and projection (check the spectra in Figure 3.9a, 3.10a 3.9b and

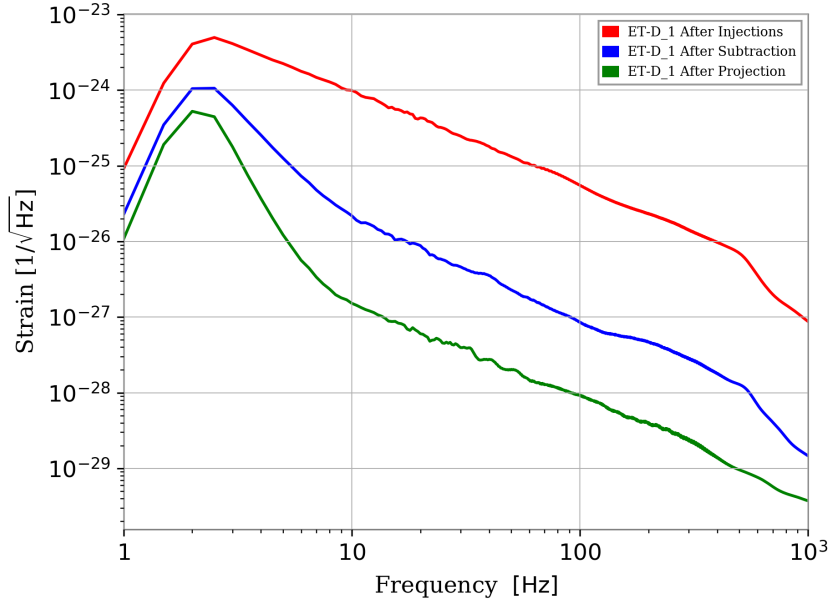


(A) Plot is shown for one ET-D.1 detector.

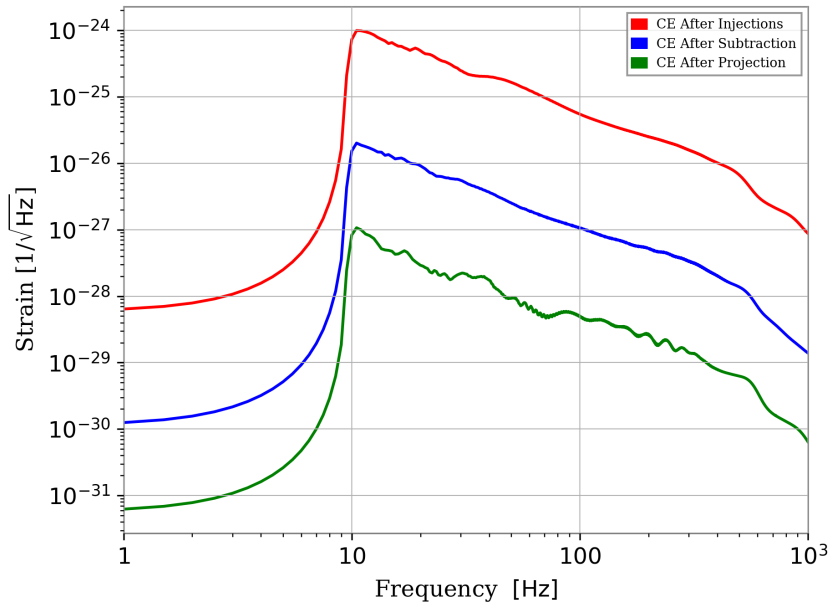


(B) Plot is shown for CE detector.

FIGURE 3.9: Plots are for **Case1** without detector noise. Simulated spectrum (i.e. square root of PSDs) of astrophysical foreground after injecting 100 BBH signals (in red), subtraction residuals after subtracting the best-fit signals (in blue), and residual spectrum after projecting out the subtraction residuals (in blue) for ET and CE detector is shown in Figure 3.9a and 3.9b respectively. The change in the curve for ET-D.1 and CE detectors are due to the difference in their sensitivity at low frequencies.



(A) Plot is shown for one ET-D.1 detector.



(B) Plot is shown for CE detector.

FIGURE 3.10: Plots are for **Case2** without detector noise. Simulated spectrum (i.e. square root of PSDs) of astrophysical foreground after injecting 100 BBH signals (in red), subtraction residuals after subtracting the best-fit signals (in blue), and residual spectrum after projecting out the subtraction residuals (in blue) for ET and CE detector is shown in Figure 3.10a and 3.10b respectively. The change in the curve for ET-D.1 and CE detectors are due to the difference in their sensitivity at low frequencies.

3.10b), for which I cannot provide an explanation since these plots only predict residuals integrated over all frequencies. As observed from the studies, the change in the spectra can vary in each time segment of the whole observation period of 1.3 years and further requires the studies associated with the waveform systematic and the choice of the waveform model.

3.6.2 Geometrical interpretation of projection method

In Subsection 3.6.1, I discussed the projection operator and its geometrical interpretation for the projection of residual noise. Here I will use a differential geometry approach which further helps us to clarify the concept of residual noise projection analysis. The idea behind this approach is to use parameters from a posterior probability distribution to define the co-ordinates on the waveform template manifold in the vector space of all detectors output.

The output data streams of the GW detectors are also vectors as each BBH signal is described by a set of λ^α parameters, representing a real parameter space. The whole data stream formed by $10^5 - 10^6$ BBH will be parameterized by $N_p = 10^5 - 10^7$ parameters (giving the dimensionality of parameter space) lying on a submanifold \mathcal{M} in vector space \mathcal{V}_i . These parameters λ^α define the co-ordinates on the waveform template manifold (Figure 3.7).

For a Gaussian and stationary noise, an inner product of two signals on a vector space \mathcal{V}_i is

$$\langle \vec{g} | \vec{h} \rangle \equiv \sum_i \int_0^\infty df \frac{g_i^*(f)h_i(f) + g_i(f)h_i^*(f)}{S_i^n(f)}. \quad (3.31)$$

$$\langle \tilde{n}(f) | \tilde{n}^*(f) \rangle = \frac{1}{2} S_n(f) \delta(f - f^*), \quad (3.32)$$

where the sign $*$ denotes the complex conjugate and S_n is one-sided PSD. The optimal SNR given by Equation (3.11) provides information about the length in Euclidean space. The inner product between vectors leads to a scalar quantity with linear and positive definite properties as similar to that of Euclidean vector space. Therefore, the scalar quantity can be used to define the norm, measure distances and angles on vector space \mathcal{V}_i . Consequently, the inner product led us to define the geometrical description for the filtering method.

In Figure 3.7, \mathcal{M} represents the manifold of all possible signals in the data stream of a detector with the true signal $h_i(\lambda^\alpha)$, the estimated best-fit signal $h_i(\hat{\lambda}^\alpha)$, detectors intrinsic noise n_i , total output of the GW detectors S_i and components of noise: parallel and perpendicular to the manifold at the point of best-fit. The parallel component of the noise is the residual noise, and the perpendicular part is the intrinsic noise of the detector. Further, intrinsic noise is not affected by the projection method.

As discussed in subsection 3.5.3, If we consider manifold \mathcal{M} of all possible physical waveforms, embedded into the vector space \mathcal{V} of almost all signals detected (i.e. extremely low SNR signal would not be detected by CE and ET) by a GW detector, we can see that after the subtraction of estimated best-fit waveforms from the detector data, residual noise will be at the point of best-fit $h(\hat{\lambda}^\alpha)$, tangent to the physical waveform as shown in Figure 3.7. If the data vector of all signals, tangential to the waveform template manifold \mathcal{M} at the true source parameters λ^α , $\delta\lambda^\alpha$ varies as SNR^{-1} , we can see for infinitesimal uncertainties two tangential planes at the point of best-fit and at the true source signal can be regarded as identical. However, in reality, this is not the case, the uncertainties in the parameter estimation depend upon many factors like, how strong is the signal measured by a detector, SNR value and the precision of the methods used to estimate the best-fit parameters of the binary signal. Consequently, uncertainties in λ^α vary, making the subtraction-noise projection method the optimal

choice for the projection of residual noise.

The projection method solely depends upon the SNR and precision of best-fit parameter estimation. The higher the SNR of a GW in the detector, the better the best-fit parameter estimation, implying that the projection method will work effectively. Whereas in lower SNR GW signals, the projection method can lose its potential due to the inaccurate parameter estimation leading to a large difference between the true source parameters and the best-fit parameters. In terms of the geometrical meaning, if we put these two vectors on the manifold \mathcal{M} , the tangent planes at the point of best-fit and true source parameters will not coincide leading to substandard performance of the subtraction-noise projection method for low SNR signals.

As I mentioned in subsection 3.6.1, the residual noise perpendicular to waveform template manifold is non-vanishing in the curved manifold, but that is not the case if we consider a flat manifold. In a flat manifold, the accuracy on the parameter estimation is less crucial because there is no separation between the tangential vector plane and manifold itself. The only quantity which is required to implement the projection method would be all possible signals detected with the GW detectors.

3.7 SCGWB and detection

The fractional energy-density spectrum of an isotropic stochastic background is defined as (details in Chapter 2)

$$\Omega_{GW}(f) = \frac{1}{\rho_c} \cdot \frac{d\rho_{GW}}{d \ln f}, \quad (3.33)$$

where $\rho_c = 3H_0^2 c^2 / (8\pi G)$ is the critical energy density required for a flat universe, H_0 is the Hubble constant ($H_0 = 67.9 \text{ km s}^{-1} \text{ Mpc}^{-1}$, [30]) and ρ_{GW} is the energy

density of GWs contained in the frequency band f to $f + df$ [35]. The current limit on the gravitational-wave energy density spectrum is $\Omega_{GW} < 4.8 \times 10^{-8}$ with 95% confidence, in the band 20 Hz - 100 Hz [20]. In this work, I simulate searches optimized for an unpolarized, isotropic, stationary and Gaussian stochastic background. In reality, stochastic signals do not necessarily have these properties [35] except for stationarity, which is simply a consequence of short observation time compared to time scales characteristic for the evolution of GW distributions.

3.7.1 Cross-correlation between detectors

Cross-correlating the output of two or more GW detectors, is the optimal strategy to detect isotropic, Gaussian, stationary SGWB (for in-depth details check in Appendix C.5). Since the analysis is performed in frequency domain, the cross-correlation is expressed as cross power-spectral density (CPSD) $C_{ij}(f)$ between two detectors i, j . I briefly review the steps to calculate the contribution of the isotropic SGWB to $C_{ij}(f)$ and how to calculate the statistical error due to instrument noise.

From Equation (B.1), an SGWB can be described as a plane-wave expansion of a metric perturbation. The CPSD can now be calculated between two detectors at locations \vec{x}_i, \vec{x}_j and antenna patterns from Equation (B.7); we can rewrite as following

$$F_i^A(\hat{\Omega}) = e_{\mu\nu}^A d_i^{\mu\nu} = e_{\mu\nu}^A \frac{1}{2} (\hat{X}_i^\mu \hat{X}_i^\nu - \hat{Y}_i^\mu \hat{Y}_i^\nu), \quad (3.34)$$

where X_i^μ, Y_i^μ are components of the unit vectors, along the two arms of detector i , which define the components of the response tensor $d_i^{\mu\nu}$ of the detector. Even though the notation X, Y suggests that arms are perpendicular to each other,

this does not need to be the case (as for ET). Assuming that plane-wave contributions to the metric in Equation (B.1) at different frequencies, from different directions, and different polarizations are uncorrelated, the CPSD can be calculated straightforwardly. The dependence of the CPSD on detector positions and orientations is summarized in the so-called ORF (see Appendix B).

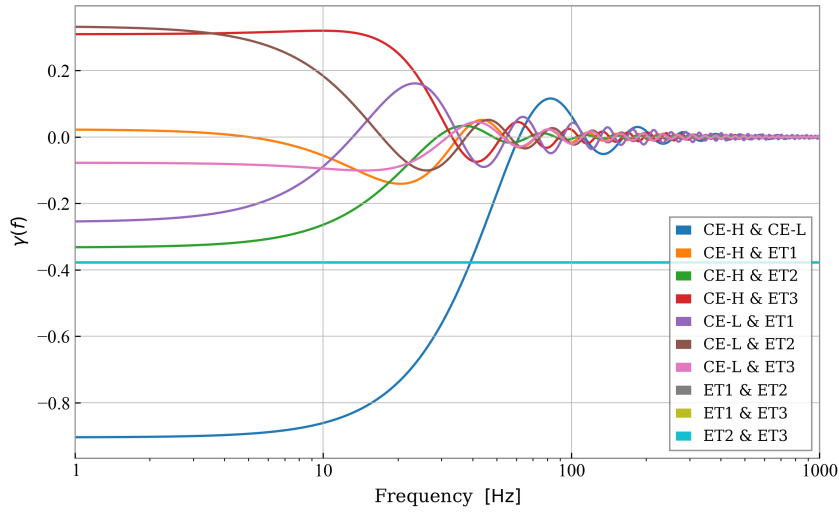


FIGURE 3.11: Plot showing the ORF $\gamma(f)$ between Cosmic Explorer at aLIGO Hanford location (CE-H), Cosmic Explorer at aLIGO Livingston location (CE-L) and Einstein Telescope (ET) at AdV location. The CE-H and CE-L are L-shape detectors, and ET is a triangular shape detector. The ORFs is shown in logarithmic frequency axis. Note that the ORF between different detectors of the ET triangle is constant with a value of about -0.38. For the subtraction-noise projection method and analysis, I used CE-H (CE as used) and ET detector network pair.

The ORFs between CE and ET are shown in Figure 3.11. While correlation measurements between detectors of the ET triangle are sensitive to SGWB over ET’s entire observation band, correlation measurements between CE and ET are most sensitive only up to about 20 Hz. However, correlating between ET detectors bears a much greater risk that other than GW signals, e.g., local magnetic and seismic disturbances, cause additional correlated contributions, which might limit ET’s sensitivity as a stand-alone observatory of SGWB. The ET-only

sensitivity will significantly depend on cancellation techniques for environmental noise as proposed in [59, 69], or the inclusion of ET's GW null-stream [136].

With the definition of ORF in Equation (C.48), the CPSDs between two detectors due to the SGWB S_{GW} can be written as [121]

$$C_{ij}(f) = S_{GW}(f)\gamma_{ij}(f), \quad S_{GW}(f) = \frac{3H_0^2}{10\pi^2} \cdot \frac{\Omega_{GW}(f)}{f^3}. \quad (3.35)$$

This value needs to be compared to the average statistical error of the CPSD from uncorrelated instrument noise,

$$\sigma_{ij}(f) = \sqrt{\frac{S_i^n(f)S_j^n(f)}{N}}, \quad (3.36)$$

where $S_i^n(f)$ is the instrument noise PSD, and N is the total number of averages going into the estimate of the CPSD. For example, if the total time-stretch of data is T , then the CPSD is calculated using segments of length τ for the fast Fourier transforms (FFTs). The CPSD calculation foresees the application of spectral windows (anti-leakage), which means that something like 50% overlap between FFT segments is recommended to make full use of all the information in the data, then we have $N \approx 2T/\tau$.

3.7.2 Optimal filtering of CPSDs

The optimal search for an SCGWB with known (unknown) or modeled (unmodeled) spectral shape involves the integral of CPSDs over frequency (details in Appendix B). However, since the relative contributions of the SCGWB and instrument noise to the CPSD vary over frequency, the optimal integration should use a filter $\tilde{Q}_{ij}(f)$, which emphasizes some parts of the spectrum over others.

The SNR of a filtered search is determined by the mean value of the integrated CPSD signals [35]

$$\begin{aligned}\langle \mathcal{C}_{ij} \rangle &= \int_0^{\infty} df \langle C_{ij}(f) \rangle \tilde{Q}_{ij}(f), \\ &= \int_0^{\infty} df \gamma_{ij}(f) S_{GW}(f) \tilde{Q}_{ij}(f),\end{aligned}\tag{3.37}$$

and their variances

$$\langle (\mathcal{C}_{ij})^2 \rangle = \frac{1}{2T} \int_0^{\infty} df S_i(f) S_j(f) |\tilde{Q}_{ij}(f)|^2.\tag{3.38}$$

The averages are over many independent estimates of CPSDs. It is straightforward to show that the optimal filter function is given by Equation (C.46). The form of the optimal filters (in arbitrary, but consistent normalization) is shown in Figure 3.12.

In all cases, the optimal filter emphasizes contributions from low frequencies near the lower bound of the observation band of the GW detectors. Inserting the optimal filter from Equation (C.46) into the Equations (3.37) and (3.38) we obtain

$$SNR^2 = \frac{\langle \mathcal{C}_{ij} \rangle^2}{\langle (\mathcal{C}_{ij})^2 \rangle} = 2T \int_0^{\infty} df \frac{|\gamma_{ij}(f)|^2 S_{GW}^2(f)}{S_1(f) S_2(f)}.\tag{3.39}$$

In a discrete version of Equation (3.39), the integral becomes the sum over all positive frequency bins, and the df needs to be replaced by $1/\tau$.

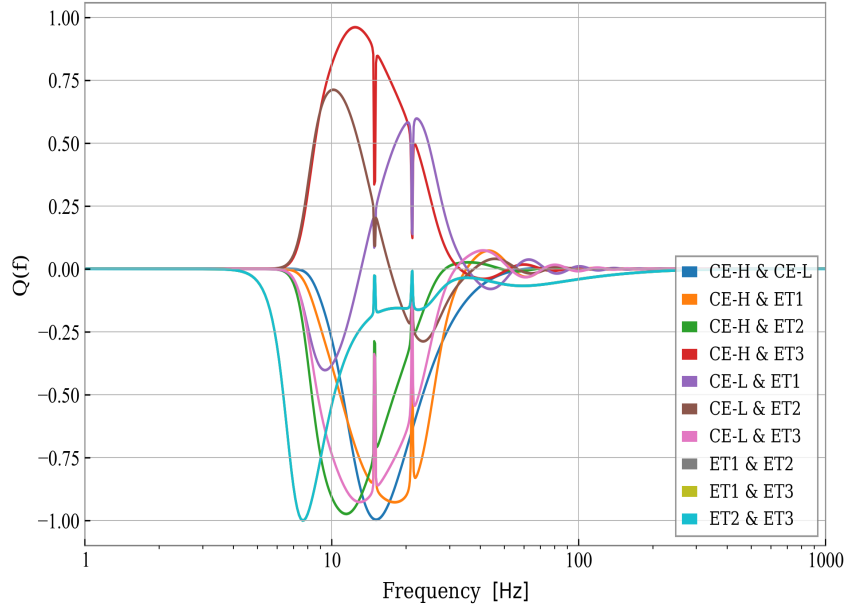


FIGURE 3.12: Plot showing the Optimal filter function $\tilde{Q}(f)$ between Cosmic Explorer at aLIGO Hanford location (CE-H), Cosmic Explorer at aLIGO Livingston location (CE-L) and Einstein Telescope (ET) at AdV location. The CE-H and CE-L are L-shape detectors, and ET is a triangular shape detector. The optimal filters between detectors of the ET triangle are all identical. For the subtraction-noise projection method and analysis, I used CE-H (CE as used) and ET detector network pair.

Figure 3.13 shows the SNR of a flat- $\Omega = 2 \cdot 10^{-12}$ stochastic background observed over 1.3 years with CE and ET detectors. The curves represent the SNRs accumulated from high to low frequencies, such that the lowest frequency values shown in the plot correspond to the SNR of the correlation measurements making use of all three detectors of an ET triangle. In this way, it is possible to see at which frequencies most of the SNR is accumulated. CE correlated with ET is most sensitive to a flat background between 8 Hz and 30 Hz, while ET by itself accumulates its SNR over a slightly broader band. The total SNR achieved by ET, in this case, is 5.2, while CE correlated with ET achieves an SNR of 3.9.

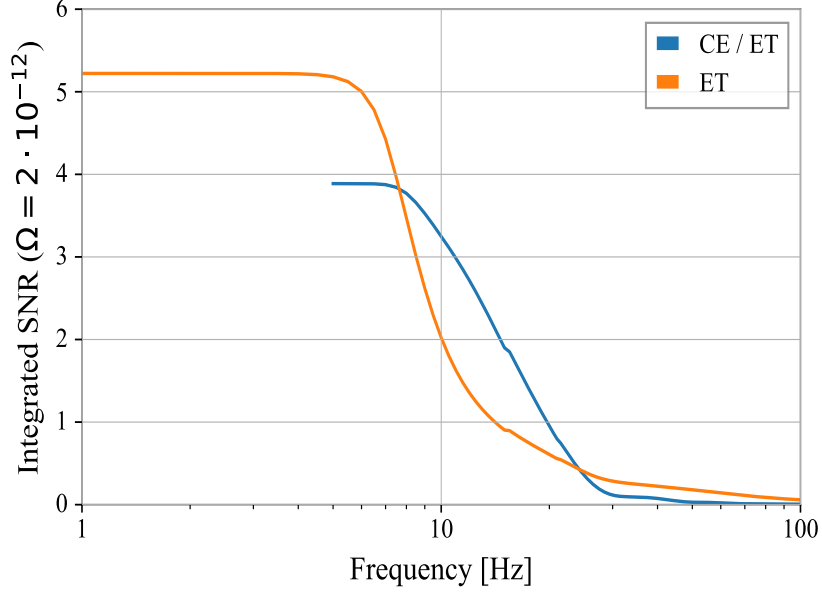


FIGURE 3.13: SNR of a flat $\Omega_{GW} = 2 \cdot 10^{-12}$ stochastic background. The curves are the SNRs accumulated from high to low frequencies. Total observation time is 1.3 years. The ORF between CE and ET is used with triangular shape ET detector and L shape CE detector.

3.8 Projection results

The goal is to demonstrate that subtraction residuals can limit the sensitivity of 3G detectors to an SCGWB search and that the subtraction-noise projection method can remove subtraction residuals. In other words, subtraction residuals can lie above the instrument-noise contribution of Equation (3.36), and that projection suppresses residuals to a level significantly below the instrument noise.

I focus this analysis on the ET and CE detector network. As stated before, the total simulated time is 1.3 years or $T = 4 \times 10^7$ s. For these studies, I chose 100 BBH signals from a cosmological distribution of 10^6 BBH signal (see Section 3.2) and performed the parameter estimation to estimate the corresponding best-fit signals. I injected these 100 BBH signals into the detector network to create the astrophysical foreground of BBH signals, i.e. 100 BBH signals are injected into each time segment (total 10000-time segments) of duration 4096 s with

and without the instrument noise. Consequently, making a 1.3-year average with a total 10^6 injected BBH signals. The CPSDs are calculated from $\tau = 2$ s discrete Fourier transforms using the Welch method with 50% overlap between time segments. For the ET case, the CPSDs are averaged over all three ET detector pairs

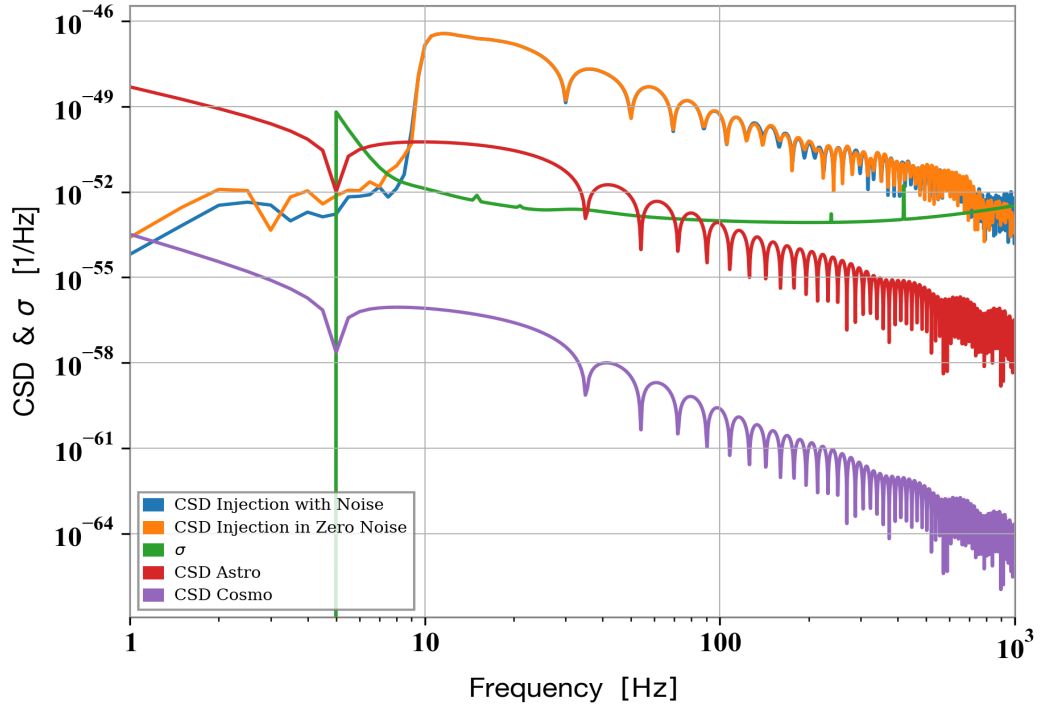
Now I will discuss the details about astrophysical and cosmological CPSD curves in Figure 3.14 and in the next figures. The red curve which represents the CPSD of astrophysical foreground is calculated by using Equation (3.35), where I used $\Omega_{GW} = 7 \times 10^{-10} \times (f/10\text{Hz})^{2/3}$, which approximates the past estimates [137]. This astrophysical foreground does not contribute to the instrumental noise. While the purple curve is CPSD of cosmological background again calculated by using Equation (3.35) with frequency-independent $\Omega_{GW} = 10^{-15}$. In all plots, the orange curves are the CPSDs of detector network time series after injecting 100 BBH signals in each time segment of duration 4096 s (total 10000 time segments) without the instrument noise. In contrast, blue curve follows the same approach as that of orange curve but 100 BBH signals, in each time segment of duration 4096 s, are injected into the instrument noise. Since the BBHs distribution I used for case1 and case 2 studies is highly anisotropic, therefore the orange curve and red curve in all plots does not have zero at same frequencies, and the mismatch in peaks. The instrument noise of the CPSD (green curve), which is the variance defined over the Gaussian PSDs and normalized over the number of FFT samples in each time segment and the total number of time segments, is calculated by using Equation (3.36). The subtraction of best-fit estimated BBH signals and projection of residual noise is also performed with the instrument noise.

Case 1: Here, I will present the results for the Case1 study when high-SNR BBH signals are injected into a detector network. And how the subtraction-noise projection method impacts the sensitivity towards SCGWB searches [154].

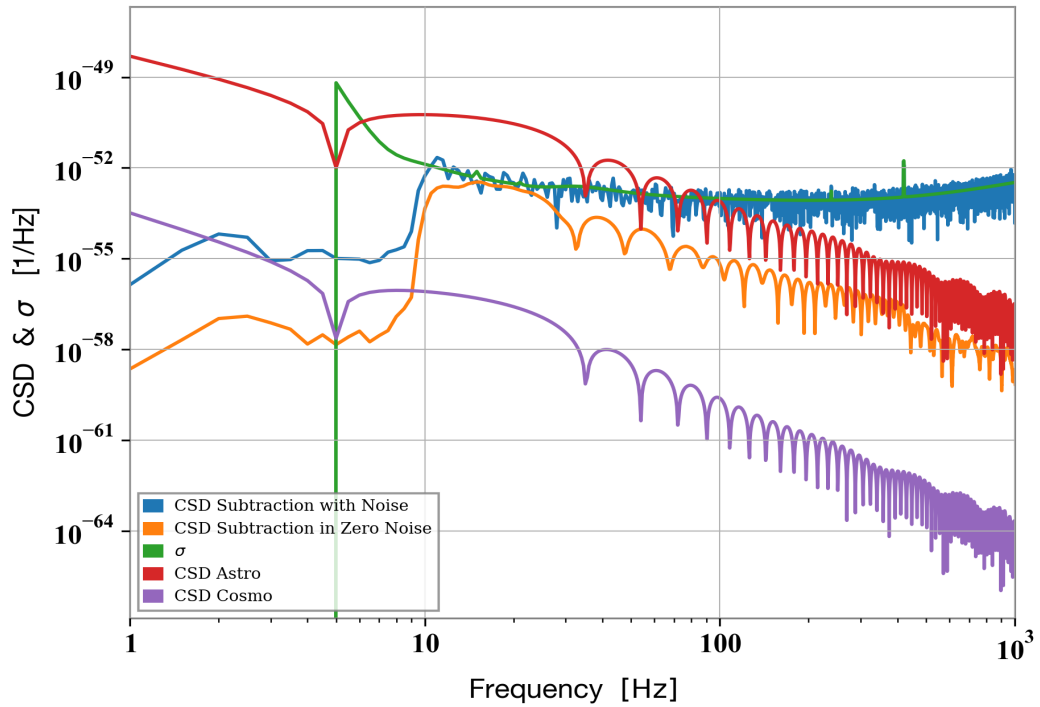
The astrophysical BBH foreground shown in the Figures 3.14a and 3.15a (blue curve, hidden behind the orange curve) exceeds past predictions (red curve). This is mostly because I selected higher-SNR members of the BBH population, and expect a Fisher-matrix based projection method to work efficiently. The subtraction residuals in 3.15b lie above the instrument noise below 10 Hz. It confirms that subtraction residuals can limit the sensitivity of ET detector to SCGWB searches. redBut this is not true for CE-ET-D_1 detector pair as the subtraction residuals in Figure 3.14b lie below the instrumental noise. The possible reason behind this could be that instead of using whole ET detector network (i.e. three ET triangular shape detectors) I used only one triangle of ET detector. This is true for 1.3 years of observation time and remains true for longer observation times (increasing observation time lowers the instrument noise in these plots, and leaves all other curves the same).

Case 2: These results in Figure 3.16 and Figure 3.17 shows the injection of BBH signals, subtraction of estimated best-fit BBH signal waveforms and projection of subtraction residuals remained after the subtraction in case2 where I used a set of 100 BBH signals with $\text{SNR} > 10$ [153].

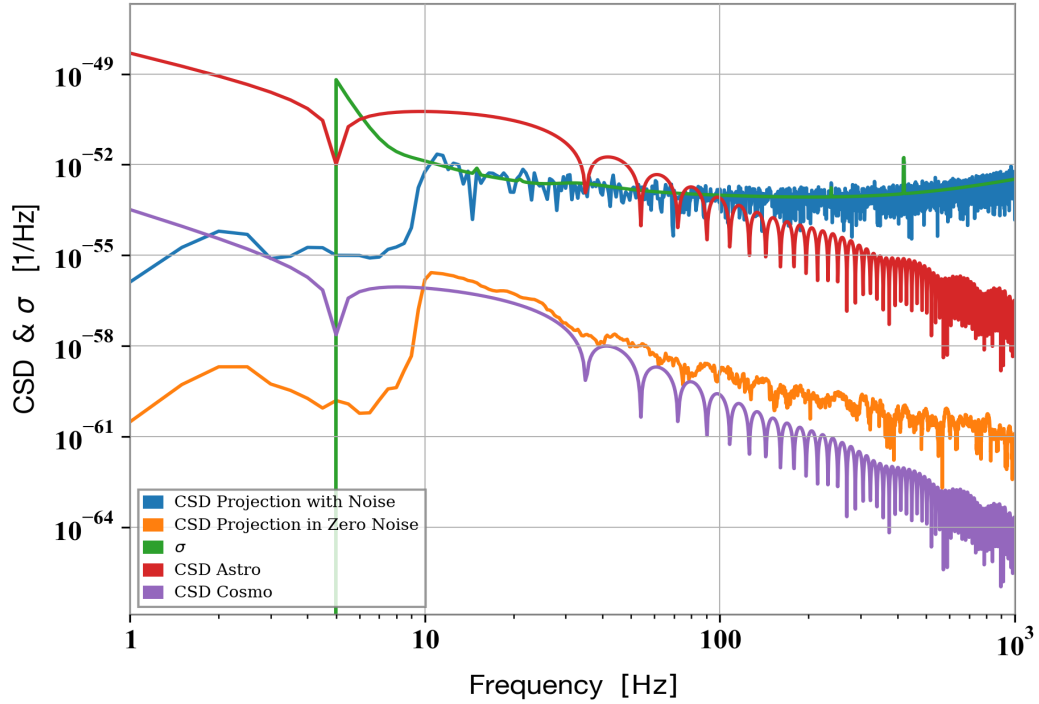
The impact of low SNR signals ($\text{SNR} > 10$), which are included as sub-threshold signal candidates in the subtraction, a projection procedure is investigated here. The projected residuals (blue curve) in the bottom plot are entirely consistent with the instrument-noise model, which means that subtraction residuals were successfully reduced even for the low SNR ($\text{SNR} > 10$) BBH signals. The full potential of an SCGWB search with CE and ET is restored for a BBH population.



(A) CSD plot after injecting BBH signals into detector network (CE and three ET), with and without instrumental noise. The plot is shown for CE and ET-D_1

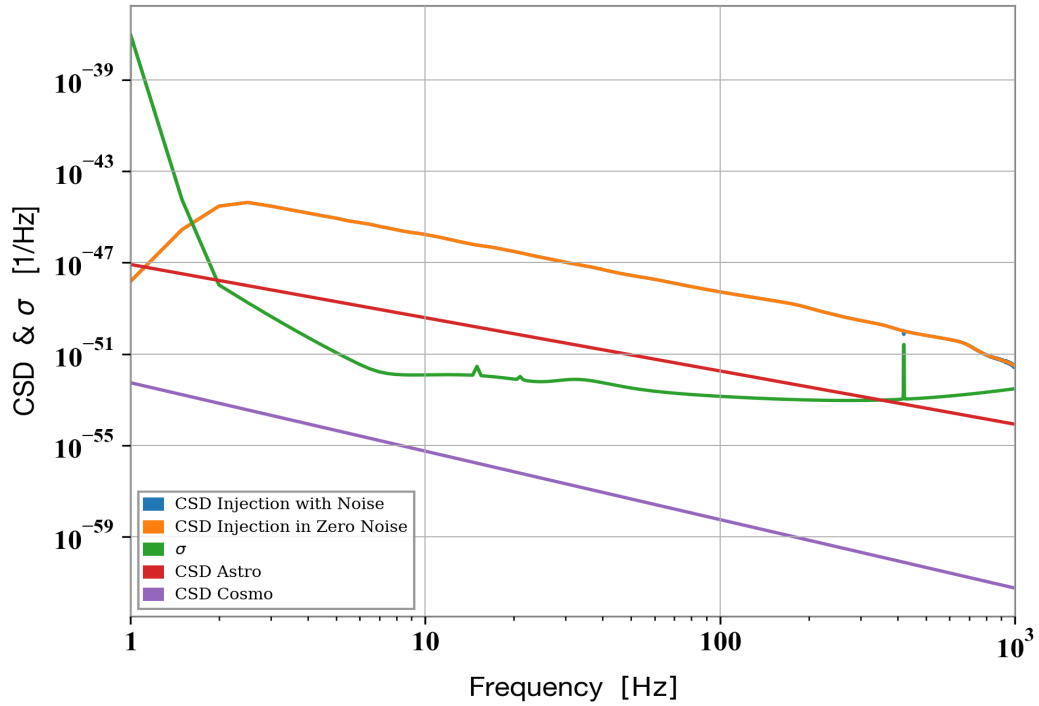


(B) CSD plot after subtracting best-fit estimated BBH signals from the detector network (CE and three ET), with and without instrumental noise. The plot is shown for CE and ET-D_1

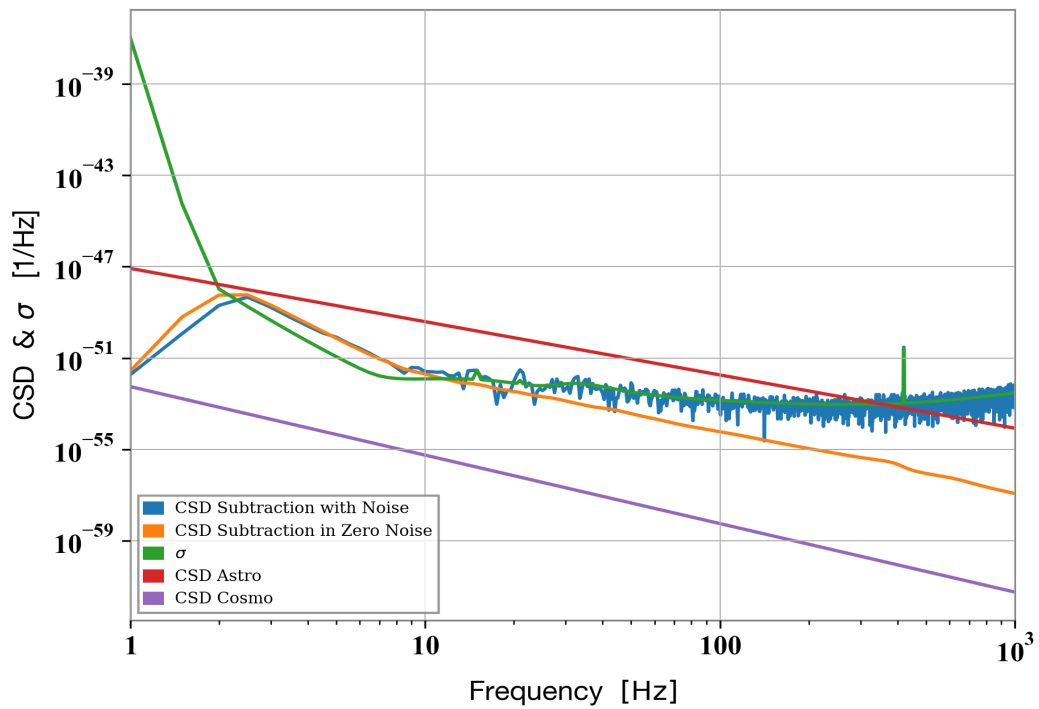


(c) CSD plot after the projection of residual noise, remained after subtraction of best-fit, shown for CE and ET-D_1 detector network.

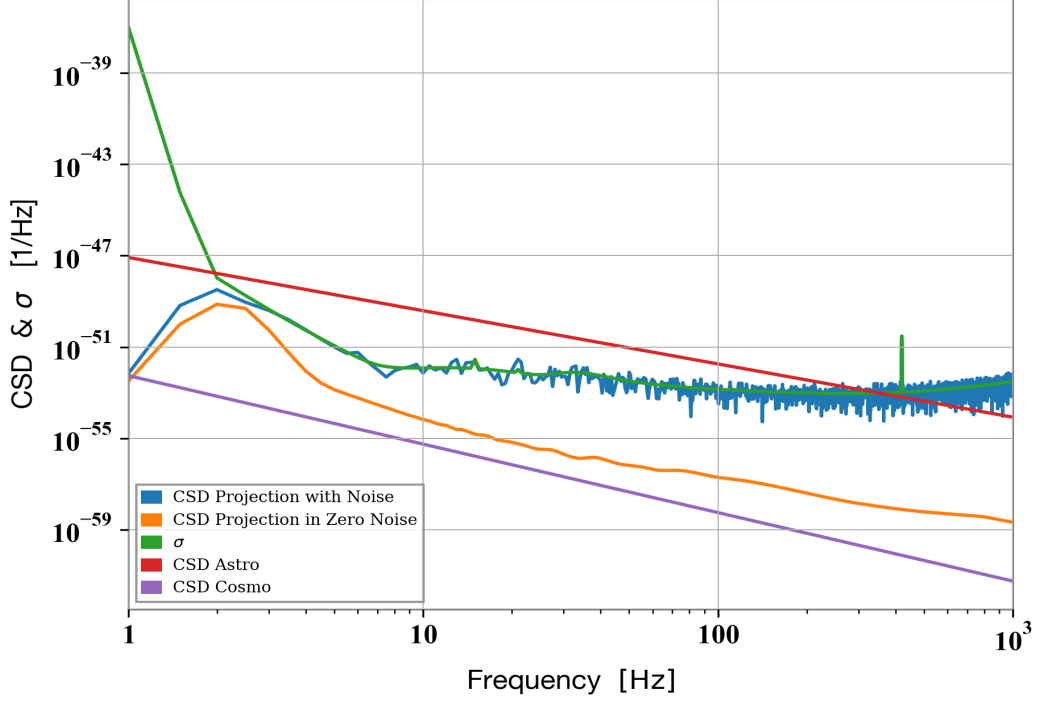
FIGURE 3.14: **Plots are for Case1.** Plots of CSDs for CE and ET-D_1 detector pair with a BBH foreground 3.14a, after best-fit subtraction 3.14b, and after noise projection 3.14c. The CPSDs are 1.3-year averages with a total of 10^6 injected BBHs. The astrophysical reference model (red curve) is only an approximation valid below about 100 Hz since it is predicted to fall more strongly above 100 Hz. The purple curve represents an SCGWB with frequency-independent $\Omega_{GW} = 10^{-15}$. The blue curves are the simulated CPSD measurements. The green curve is the predicted instrument noise. The orange curves show the CPSD for simulations without instrument noise.



(A) CSD plot after injecting BBH signals into ET detector, with and without instrumental noise. The plot is shown for the complete ET detector, averaged over the three individual detectors of ET.

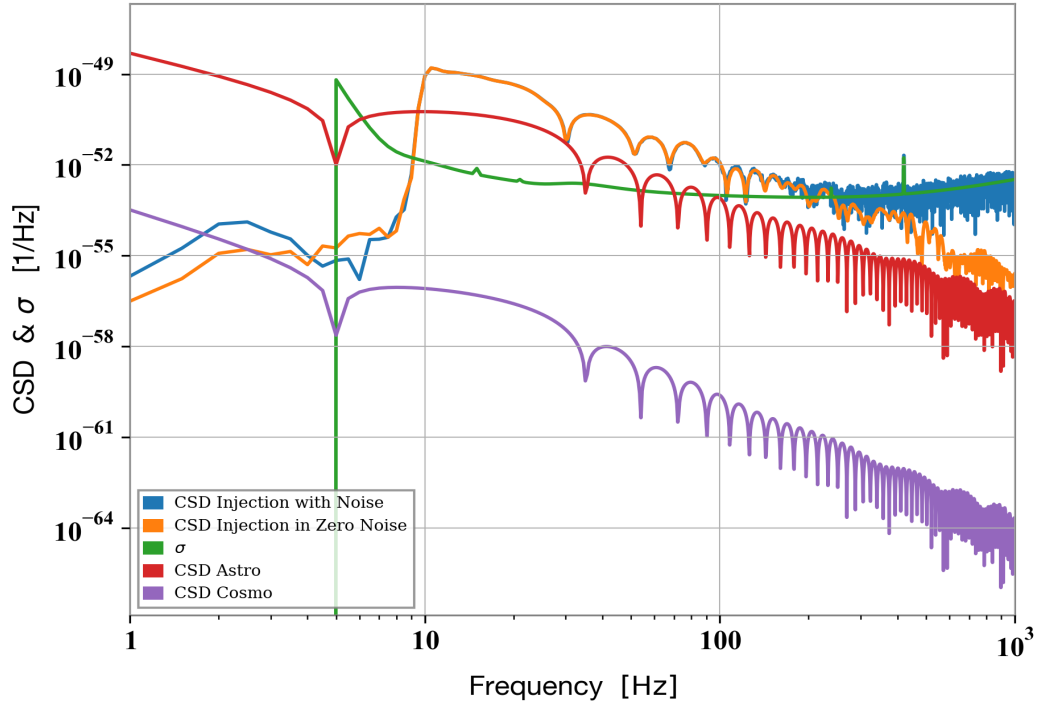


(B) CSD plot after subtraction of estimated best-fit BBH signals from ET detector, with and without instrumental noise. The plot is shown for averaged ET detector.

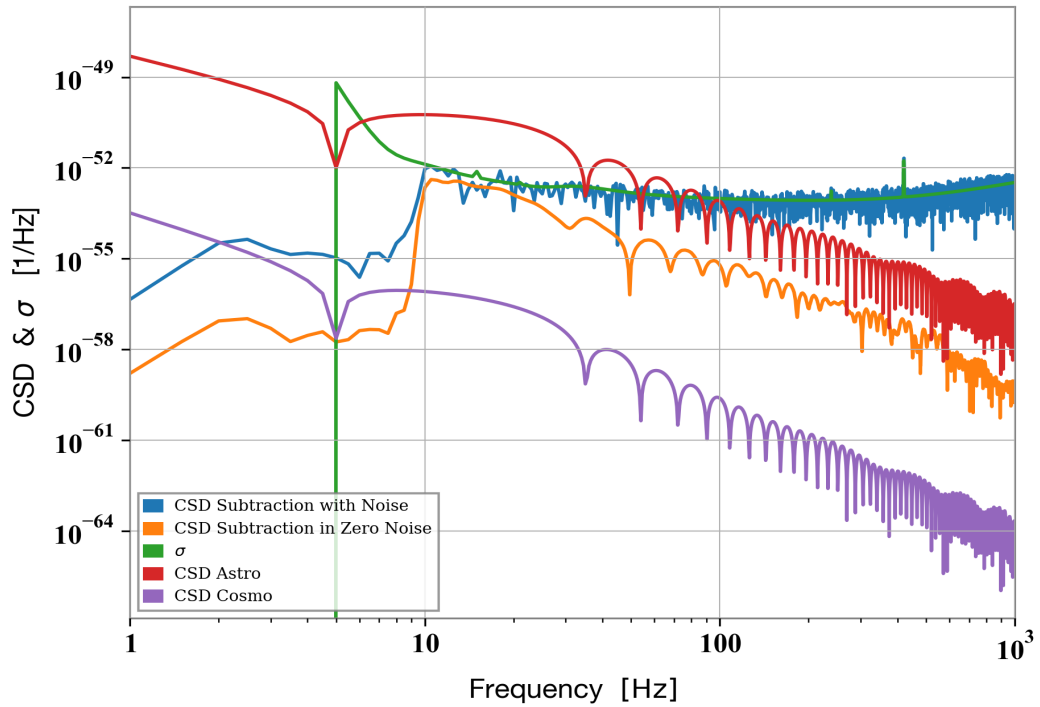


(c) CSD plot after the projection of subtraction residuals, shown for averaged ET detector.

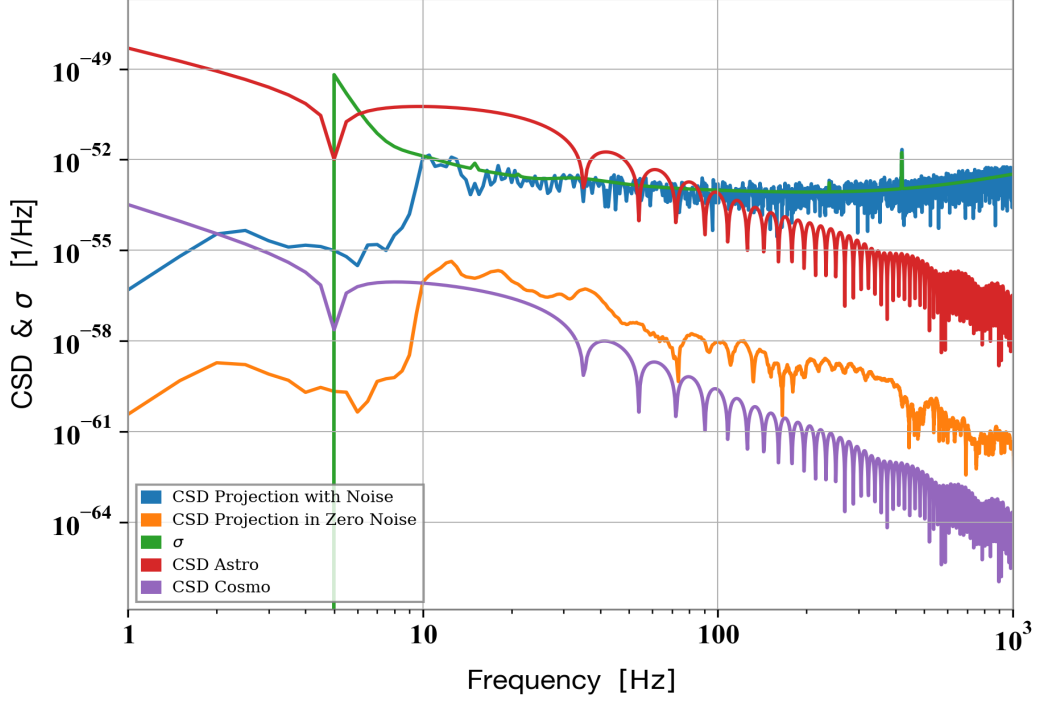
FIGURE 3.15: **Plots are for Case1.** Plots of residual CSDs averaged over all ET detector pairs with BBH foreground Figure 3.15a, after estimated best-fit BBH signals subtraction Figure 3.15b, and after subtraction residuals projection Figure 3.15c. The CPSDs are 1.3-year averages and also averaged over all detector pairs of the ET triangle with a total of 10^6 injected BBHs. The astrophysical reference model (red curve) is only an approximation valid below about 100 Hz since it is predicted to fall more strongly above 100 Hz. The purple curve represents an SCGWB with frequency-independent $\Omega_{GW} = 10^{-15}$. The blue curves are the simulated CPSD measurements. The green curve is the predicted instrument noise. The orange curves show the CPSD for simulations without instrument noise.



(A) CSD plot after injecting BBH signals into detector network with and without instrumental noise. The plot is shown for CE and ET-D.1

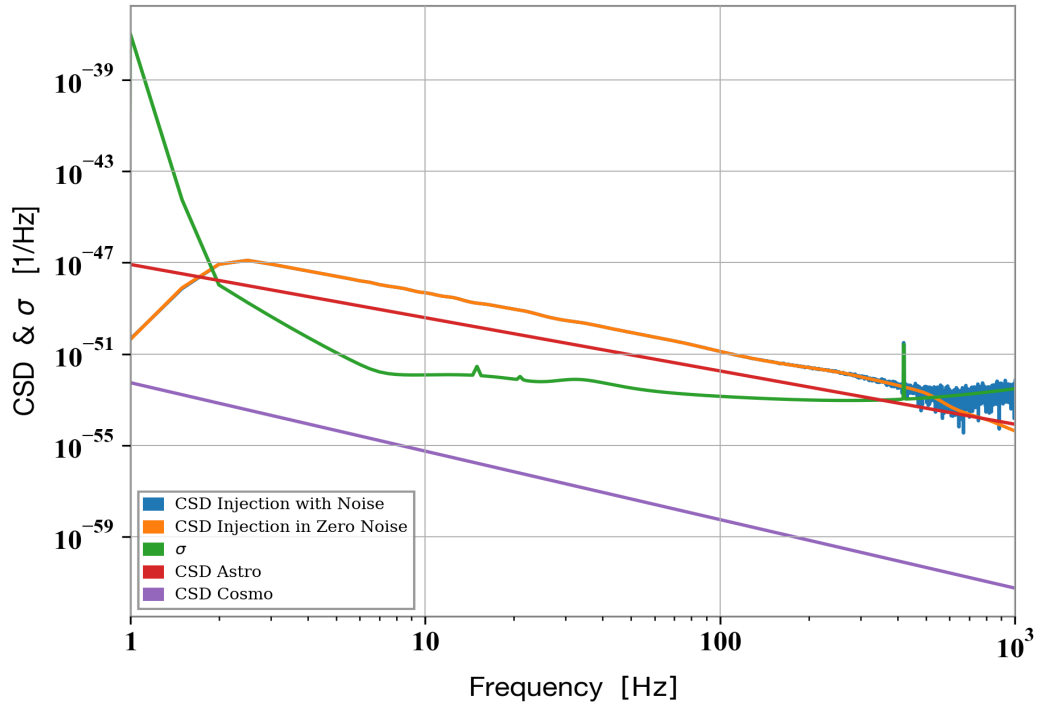


(B) CSD plot after subtracting estimated best-fit BBH signals from the detector network with and without instrumental noise. The plot is shown for CE and ET-D.1

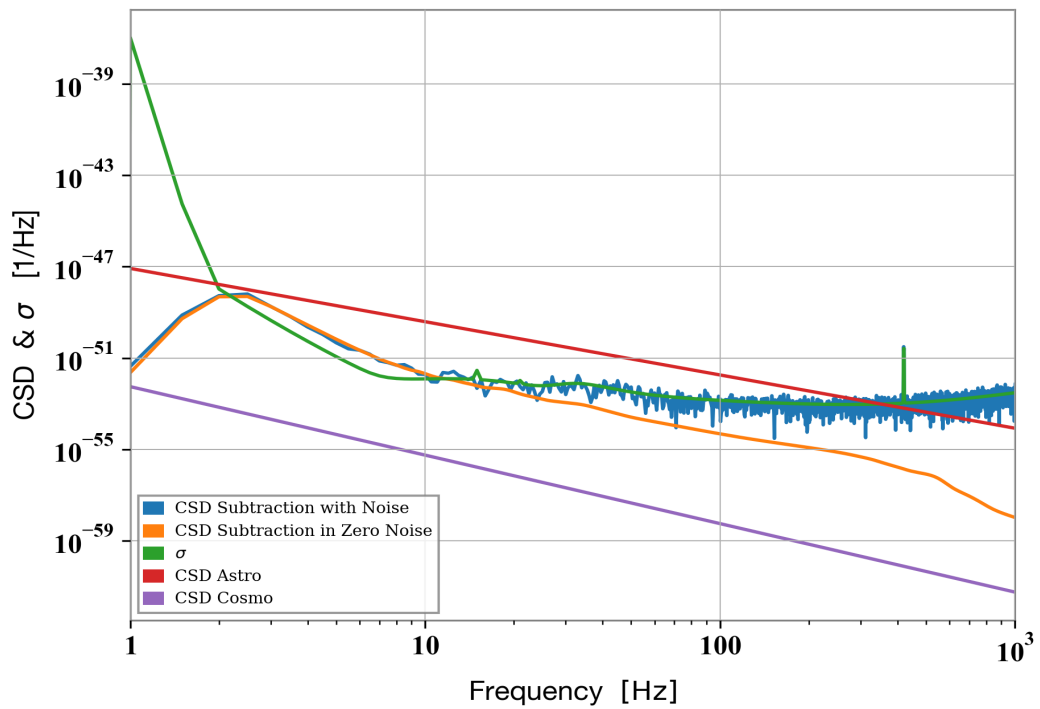


(c) CSD plot after the projection of subtraction residuals, shown for CE and ET-D_1 detector network.

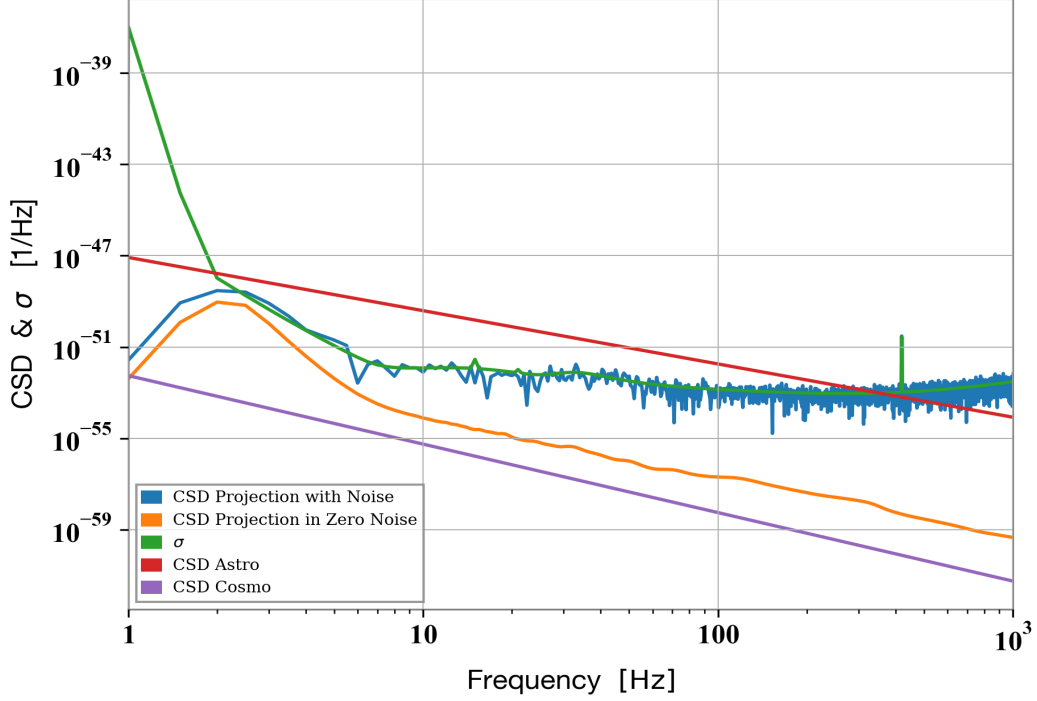
FIGURE 3.16: **Plots are for Case2.** Plots of residual CSDs for CE and ET-D_1 detector pair with BBH foreground Figure 3.16a, after best-fit subtraction Figure 3.16b, and after residual noise projection Figure 3.16c for **Case2**. The CPSDs are 1.3-year averages with a total of 10^6 injected BBHs. The astrophysical reference model (red curve) is only an approximation valid below about 100 Hz since it is predicted to fall more strongly above 100 Hz. The purple curve represents an SCGWB with frequency-independent $\Omega_{GW} = 10^{-15}$. The blue curves are the simulated CPSD measurements. The green curve is the predicted instrument noise. The orange curves show the CPSD for simulations without instrument noise.



(A) CSD plot after Injecting BBH signals into ET detector, with and without instrumental noise. The plot is shown for the complete ET detector, averaged over the three individual detectors of ET.



(B) CSD plot after subtraction of best-fit estimated BBH signals from ET detector, with and without instrumental noise. The plot is shown for averaged ET detector.



(c) CSD plot after the projection of subtraction residuals, shown for averaged ET detector.

FIGURE 3.17: **Plots are for Case2.** Plots of residual CSDs averaged over all ET detector pairs with BBH foreground Figure 3.17a, after best-fit subtraction Figure 3.17b, and after noise projection Figure 3.17c. The CPSDs are 1.3-year averages and also averaged over all detector pairs of the ET triangle with a total of 10^6 injected BBHs. The astrophysical reference model (red curve) is only an approximation valid below about 100 Hz since it is predicted to fall more strongly above 100 Hz. The purple curve represents an SCGWB with frequency-independent $\Omega_{GW} = 10^{-15}$. The blue curves are the simulated CPSD measurements. The green curve is the predicted instrument noise. The orange curves show the CPSD for simulations without instrument noise.

3.9 Conclusion

In this work, I presented an analysis of a noise-projection method based on a higher-order geometrical analysis of matched-filter GW searches to mitigate subtraction residuals of an astrophysical foreground in the proposed third-generation detectors ET and CE. I showed that the projection method could improve the

sensitivity to an SCGWB. I provided insight into why the projection method is expected to work, and tested the method with a time-domain simulation of a future GW detector network. The decisive first step of the analyses, i.e., the estimation of BBH parameters, was carried out with state-of-the-art parameter-estimation software (Bilby) by posterior sampling. The presented results are a proof-of-principle since more simulation of the astrophysical foreground had to be done (if all the CBC sources are observed by ET and CE detectors, If not then their implications in SCGWB searches with the subtraction-noise projection method). The results indicate that the projection method can lower the subtraction residuals from BBHs to a level below the statistical errors of a one-year long observation of the SCGWB.

Chapter 4

O3 Analysis : Upper limits on SGWB

We have seen how primordial GW backgrounds are produced by early-universe phenomena, and how crucial they are to probe the fundamental physics of the early universe. In this chapter, I will present my contribution to detector characterization of AdV during the second period of the third observation run and to the searches of a SCGWB with data from the entire science run O3 from aLIGO and AdV detectors.

4.1 AdV Characterization

Characterization of a GW signal in the presence of detector noise is a challenging task, which requires specific expertise and tools. The output of a GW detector is dominated by its noise, which can be stationary and Gaussian in addition to non-Gaussian noise contribution, termed as glitches. The instrumental glitches in the detector data can resemble the burst GW signal, and generally contribute to a non-stationary noise background impeding all GW searches. Hence,

the characterization and possible subtraction of glitches is of great importance. The catalogs for glitch identification have been formed by the aLIGO and AdV collaboration based on their observational studies and identification process.

This part includes the results from the contribution I made towards AdV DetChar as a part of research work with Virgo group at Pisa. My contribution to AdV characterization consists of

1. Study and analyze the data, glitches and observations made by AdV detector during the period of study.
2. Investigate the detector and environmental noise in the AdV detector.
3. Review continuous noise analysis using online monitoring and data quality analysis.
4. Collaborate with data quality analysis group and commissioning group to improve the overall detector sensitivity.

These observations are of great importance in stochastic signal searches as glitches can limit the sensitivity to a stochastic background, hence requiring a better understanding of detector working and efficiency during the data observation period. I will discuss the observations made and how these are related to noise sources we discussed in Subsection 1.3.3.

Flicker Noise: Flicker Noise is caused by random fluctuations in electronic devices and varies inversely proportional to the frequency. In AdV detector, flicker noise is not of a great importance as the detector is already dominated by other noise sources in the lower frequency range below 30 Hz (see Figure 1.4). Figure 4.1 and 4.2 shows the flicker noise contribution to the intrinsic noise of AdV detector below 50 Hz. Flicker noise reported to be high in comparison to other noise contributions during the observation period.

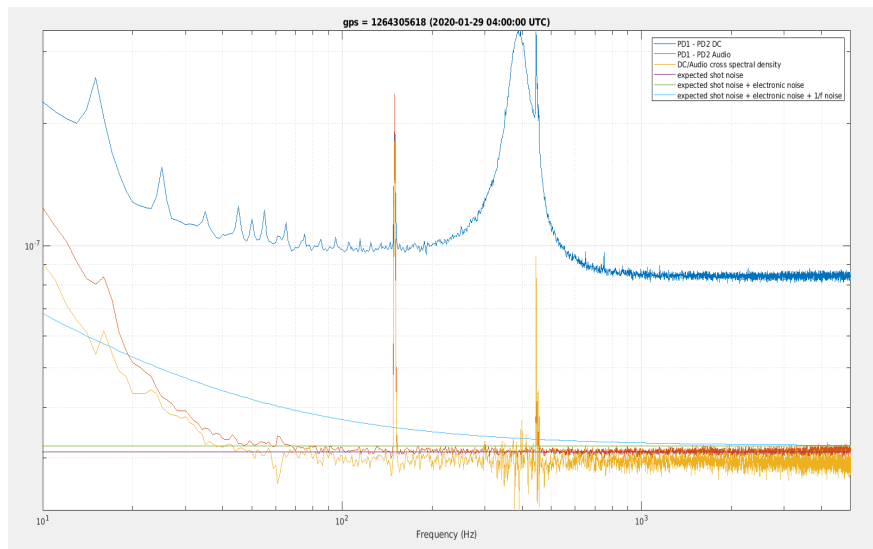


FIGURE 4.1: Flicker noise (in cyan color) after the replacement of photodiodes which is altogether constant above 50 Hz. The red curve shows the difference between the audio channels.

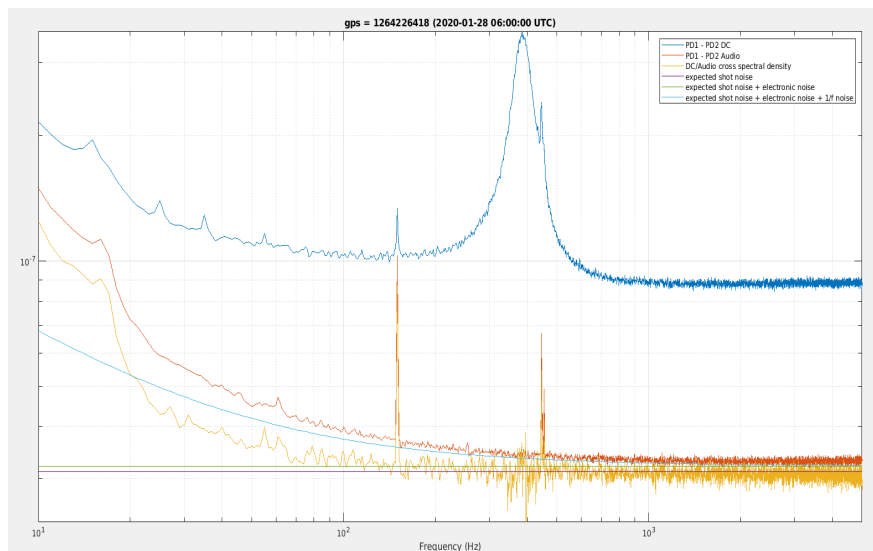


FIGURE 4.2: An increase in flicker noise (in cyan color) a night before the observation (see Figure 4.1). The red curve shows the difference between the audio channels.

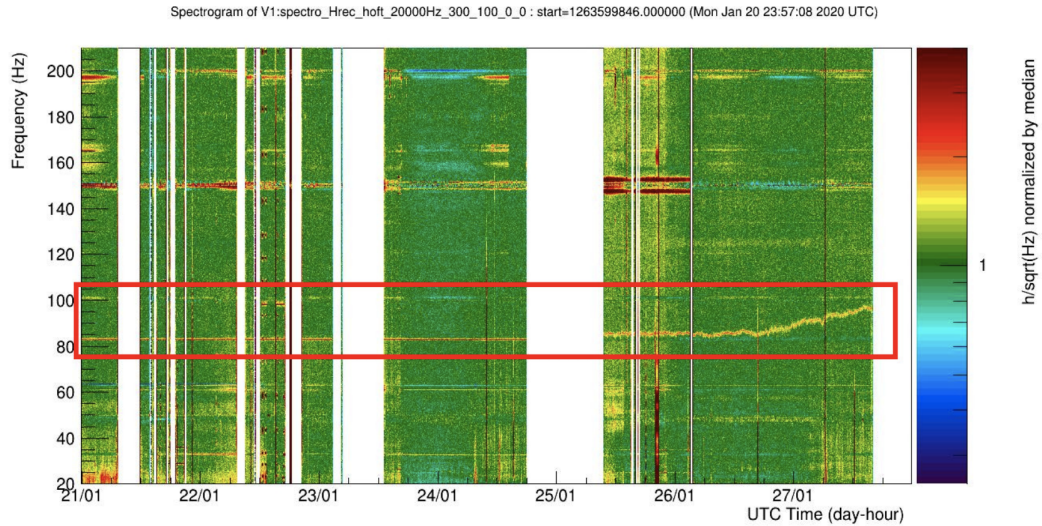


FIGURE 4.3: The frequency line at 80 Hz starts to rise in the AdV spectrum from January 26, 2020, onwards.

Fluctuations in Frequency Lines: The coupling between the environment and the detector data can lead to noise in the observation band. It was found in the AdV spectrum, for example, the 80 Hz frequency line started to move in frequency band (Figure 4.3) due to very high correlation between the environment channels on the North East Side of the detector building (NEB) "ENV_NE_CT_ACC_Z" (see Figure 4.4). An analysis was performed by using NonNA cross-correlation (line tracker tool to investigate the non-stationary behaviour of target signal correlating with auxiliary channels) and "brute-force" coherence tool (BruCo, computes the coherence between all channels and searches for noise correlations) to cross-correlate the wandering frequency line with time series to track the evolution of frequency line in the observed frequency band, see Figure 4.4.

Excitation of 48 Hz Line: The excitation in the 48 Hz frequency line caused by some electronics interference between detector data and the leading environmental channels in Central East Building (CEB), West-East Building (WEB), and North East Building (NEB). Figures 4.5, 4.6 and 4.7 show the different contributions of coherence due to environmental noise. These low-frequency lines

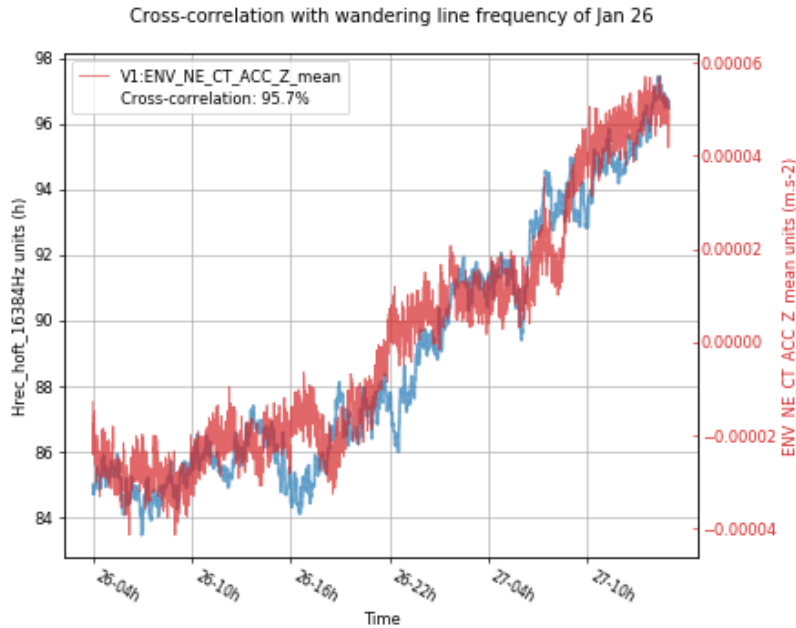


FIGURE 4.4: Plot showing high correlation between the 80 Hz frequency line and ENV_NE_CT_ACC_Z.

play a crucial role in detector data analysis for SCGWB searches as they can lead to deviation in the detector data, leading to false observations.

These frequencies (Table 4.2) then can be notched out during the SCGWB searches while calculating the point estimates and corresponding error values.(see Section 4.2).

Maximum BNS Range: The BNS range of the AdV detector reached up to 59 Mpc in one of time bin, as shown in Figure 4.8 making AdV most sensitive during the whole O3.

Glitch Due to Excitation of Test Mass: Beside the stationary detector noise, GW detectors also need to deal with non-Gaussian noise events referred to as glitches. Transient noise or glitches can originate from, detector malfunction, technical faults, environmental process, and other various sources. These signals can be of short duration or can exist for several seconds in the detector data. The identification and study of these transient noises depend upon instrumental

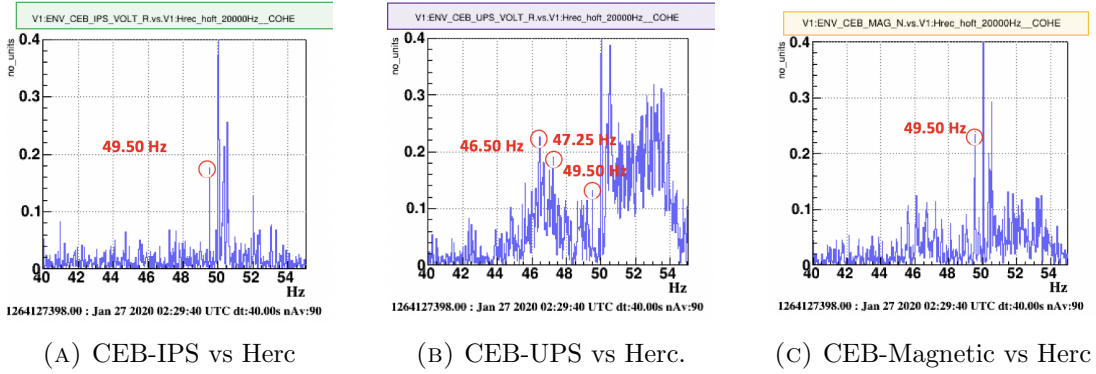


FIGURE 4.5: Plot showing the coherence investigation between Herc and the main environmental channel (CEB-IPS, CEB-UPS and CEB-Magnetic) of the AdV detector site. The Coherence value in the frequency range (46 - 48) Hz is in range (0.10-0.24), while coherence in frequency range (50-54) Hz is in range (0.20-0.40).

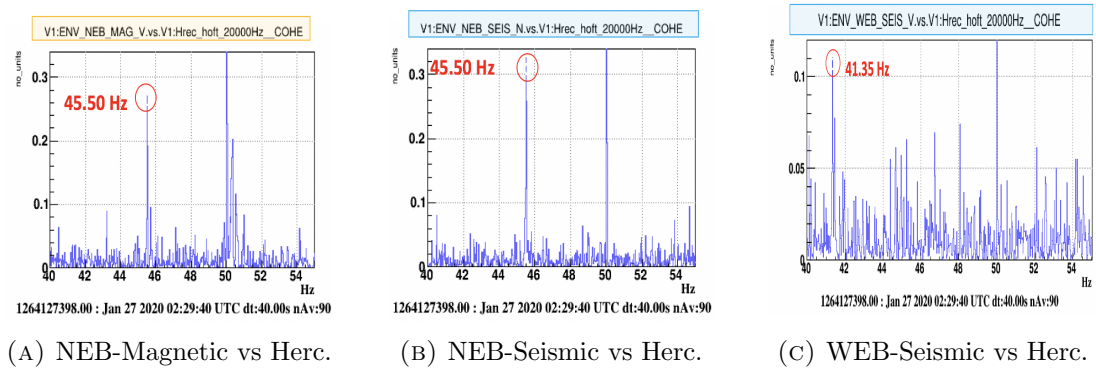


FIGURE 4.6: Plot showing the coherence investigation between Herc and the main environmental channel (NEB-Mangetic, NEB-Seismic and WEB-Seismic) of the AdV detector site.

and environmental monitoring. Hence, thousands of various sensors associated with auxiliary channels are placed at the AdV detector location to study these transient signals. Due to the transient nature, it is challenging to perform data analysis techniques to study and identify the source of glitches. Based on their properties, these glitches are categorized in separate glitch families. Three such prominent glitch families originate from technical challenges (i.e. when the detector is under commissioning phase or small changes in instrumentation are performed), environment, or controls.

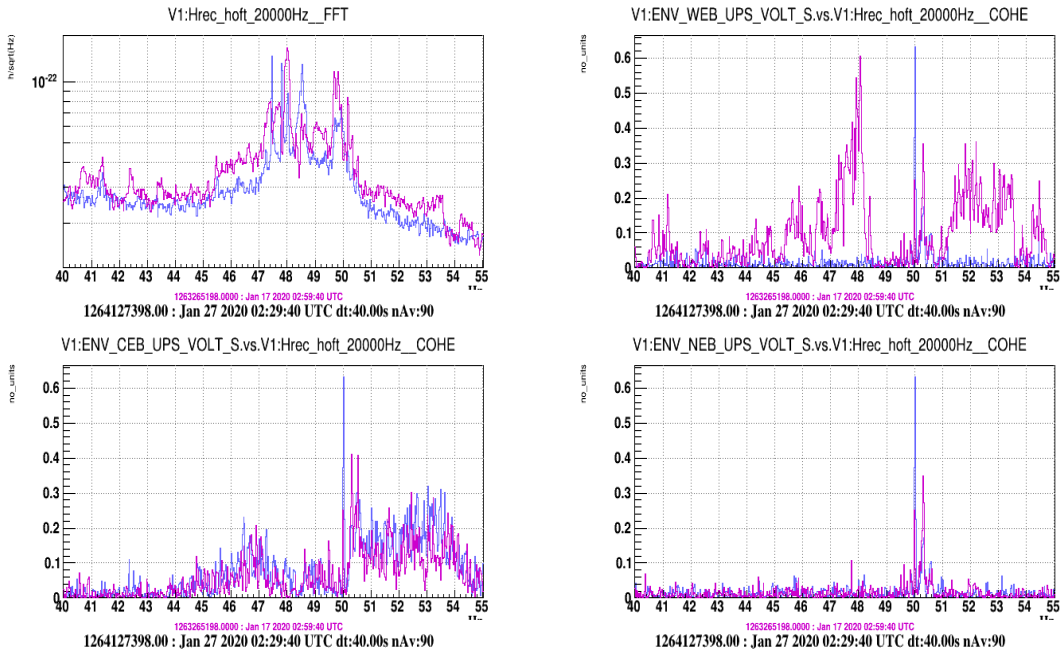


FIGURE 4.7: Plot showing the acoustic coherence between Herc and the CEB_UPS, WEB_UPS and NEB_UPS of the AdV detector site. The coherence with UPS lines before mitigating 48 Hz in WEB_UPS (purple color line) and after that (blue color line) shows an apparent reduction in the coherence level.

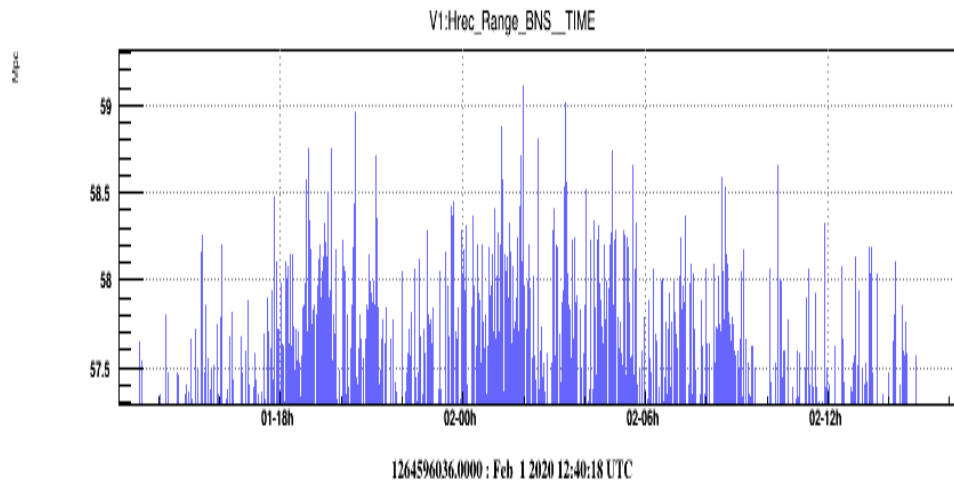


FIGURE 4.8: Plot showing that AdV reached 59 Mpc BNS range during O3 observational run. Plot was produced by AdV group. Y-axis is in Mpc.

The primary tool used for the detection and characterization of glitches with accuracy is an algorithm named as **Omicron**, (more details in [140]). Figure 4.9 shows the distribution of glitches in the time-frequency domain obtained with **Omicron** for one day during the shift.

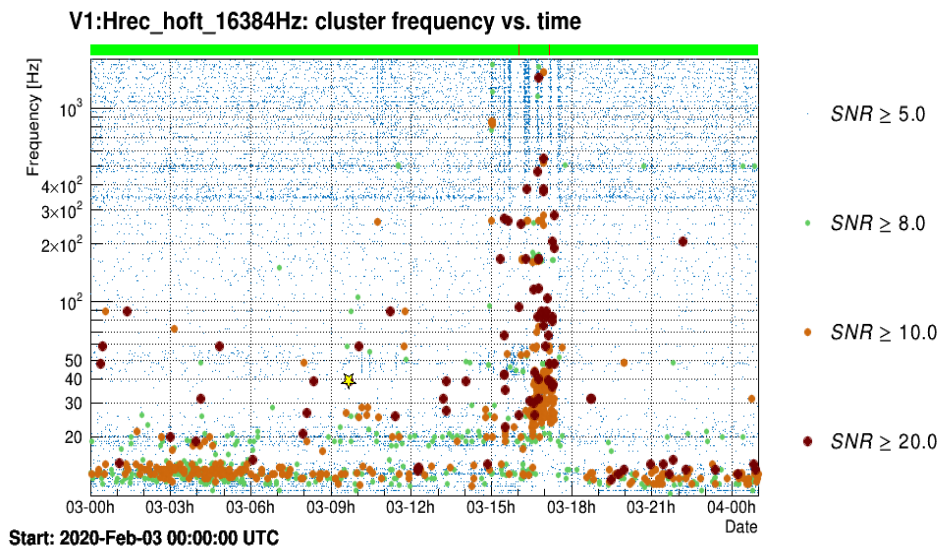


FIGURE 4.9: Time Frequency distribution of transient noise detected by **Omicron** on February 3, 2020 in AdV data.

The dots above 100 Hz in Figure 4.9 correspond to technical glitches due to the scattering of light through vibrations in the optical system. The other types of glitches are due to photodiodes used to measure the dark fringe. The low-frequency contribution to these glitches comes from microseismic activities due to the environment. Dots in the vertical line between 03-15h to 03-18h correspond to the glitches due to the commissioning of the AdV detector. Below 30 Hz lie the high SNR glitches coming from human activities at the detector site (red dots in low-frequency regime).

A glitch due to excitation of a test mass observed at $gps = 1264554506$ is shown in Figure 4.10, observed on February 1, 2020. The glitch occurred due to the slight sliding or adjustment between the suspension fibre edge and the mirror itself leading to the excitation of all violin and bulk modes (see Figure 4.11).

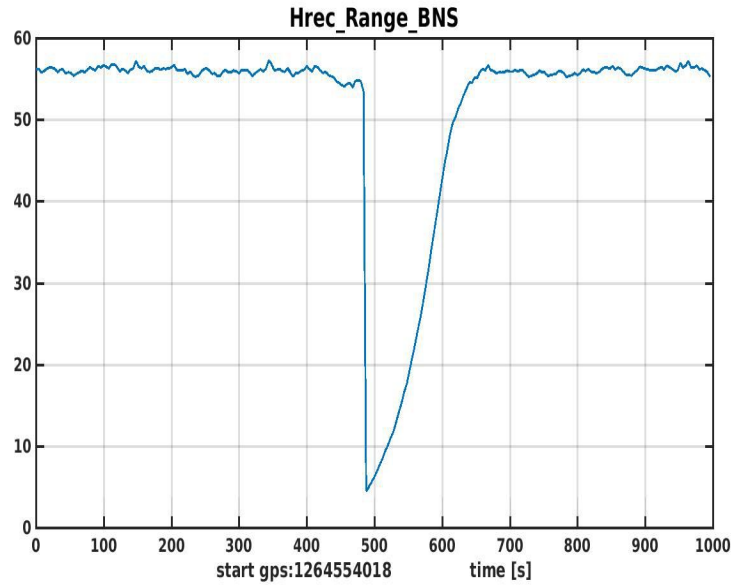


FIGURE 4.10: The glitch occurred due to the movement between the suspension fibre edge and the mirror.

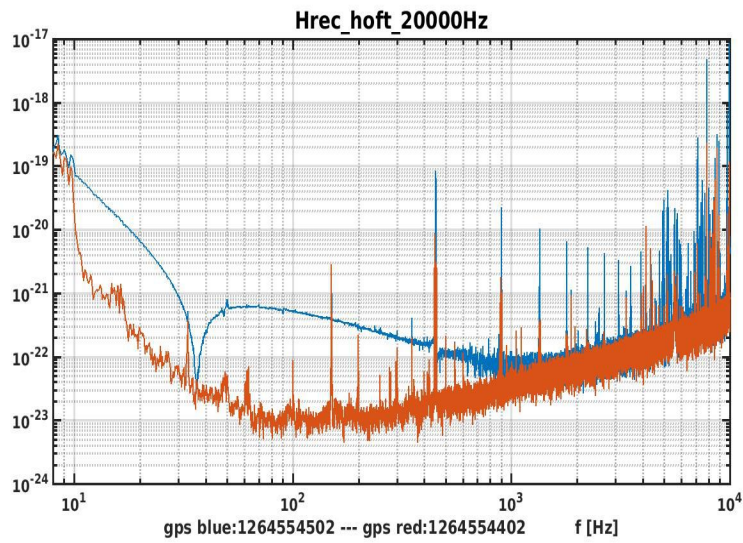


FIGURE 4.11: Spectrum observed during the glitch in Figure 4.10 providing information about the event dynamics.

4.2 SGWB searches in O3 data

The limits on SGWBs obtained with GW detectors set constraints on the evolution of the universe till now and the associated GW spectrum, which further constrain the cosmological parameters. This section presents the results from the stochastic analysis I performed using the stochastic pipeline with the whole third observation run data of aLIGO and AdV detectors, including the current upper limits on SGWB from O3 run [26].

4.2.1 Optimal filtering of data

The GW detectors record data as time series which include a contribution from various noise sources (see Subsection 1.3.3) alongside a GW signal. The observed data is then sampled and cleaned before the analysis.

The GW detectors aLIGO (two aLIGO, one at Hanford (H1) and one at Livingston (L1)) and AdV (V1) form three detector baselines, which we denote as H1L1, H1V1 and L1V1. In each baseline, the data from two detectors are cross-correlated using the relation in Equation (C.40) and then optimally filtered by using Equation (C.46) to maximize the signal strength for the SGWB searches.

Here, I will present the method used for SGWB searches in aLIGO and AdV detectors. For a GW detector with N independent measurements (running over different data samples), the output is given by $s_i = h + n_i$ with $i = 1, \dots, N$, where h is an SGWB and n is the instrumental noise of the detector. By considering that the noise has zero mean and Gaussian distribution with a known variance σ_i^2 , we want to find the quantity \hat{h} with minimum variance such that [143]

$$\hat{h} \equiv \sum_i \lambda_i s_i, \quad (4.1)$$

is the unbiased estimator of a true signal h with condition $\langle \hat{h} \rangle = h$, implying that $\sum_i \lambda_i = 1$ and must hold for the minimum variance (i.e. minimum value unbiased estimator is unique). Thus the minimum variance in \hat{h} is

$$\sigma_h^2 = \sum_i \lambda_i^2 \sigma_i^2 = \text{minimum}. \quad (4.2)$$

If condition $\sum_i \lambda_i = 1$ does not hold for minimum variance unbiased estimator, it can be minimized by using Lagrange's method as [143]

$$f(\lambda_i, \Lambda) \equiv \sum_i \lambda_i^2 \sigma_i^2 + \Lambda \left(1 - \sum_i \lambda_i \right), \quad (4.3)$$

with respect to λ_i and Λ , giving λ_i

$$\lambda_i = \left(\sum_j \frac{1}{\sigma_j^2} \right)^{-1} \frac{1}{\sigma_i^2}, \quad (4.4)$$

where $\left(\sum_j \frac{1}{\sigma_j^2} \right)^{-1}$ represents the linear combination of weighted average, giving less weight to the noise measurements which have large variance. Hence, it is the variance of the optimal combination σ_h^2 . Therefore, the linear combination is defined as

$$\hat{h} = \left(\sum_j \frac{1}{\sigma_j^2} \right)^{-1} \sum_i \frac{s_i}{\sigma_i^2}, \quad (4.5)$$

giving less weights to the noisier measurements. The covariance matrix gives the correlated measurement between s_i with non-zero values (if s_i are correlated)

$$C_{ij} = \langle s_i s_j \rangle - \langle s_i \rangle \langle s_j \rangle, \quad (4.6)$$

for $i \neq j$, where $i, j = 1, \dots, N$ measurements of a detector (running over different data samples). Thus the linear combination of the data with the minimum variance from Equation (4.1) is

$$\hat{h} \equiv \sum_i \sum_j \lambda_i \lambda_j C_{ij}. \quad (4.7)$$

4.2.2 Cross correlation spectrum

For a stationary, Gaussian, unpolarized and isotropic SGWB, the cross-correlation in every frequency bin of the detector data with a frequency resolution Δf centred at f , is given by [20, 26]

$$\hat{C}_{ij}(f) = \frac{2 \Re[\tilde{s}_i^*(f) \tilde{s}_j(f)]}{T \gamma_{ij}(f) S_{GW}(f)}, \quad (4.8)$$

where \tilde{s}_i is the Fourier transform of the time series data, T is the time segment duration of the data for Fourier transformation, γ_{ij} is the normalized ORF and $S_{GW}(f)$ (see Equation (3.35)) is the spectral shape of Ω_{GW} [91, 121]

Equation (4.8) is normalized such that $\langle \hat{C} \rangle = \Omega_{GW}(f)$, which is the energy density of the SGWB in each frequency bin [20]. The variance of $\hat{C}_{ij}(f)$ is

$$\sigma_{ij}^2(f) \approx \frac{1}{2T\Delta f} \frac{P_i(f)P_j(f)}{\gamma_{ij}^2(f)S_{GW}^2(f)}. \quad (4.9)$$

where P_i is the one-sided PSD of detector i . A GW detector data in a specific frequency band can consist of multiple frequency bins of width Δf . Thus the optimal estimator is the overall sum of all individual estimators in each frequency bin with a weighted average of the cross-correlation across frequency bins f_k

$$\begin{aligned}\hat{C}_{ij} &= \frac{\sum_k w(f_k) \hat{C}_{ij}(f_k) \sigma_{ij}^{-2}(f_k)}{\sum_k w(f_k)^2 \sigma_{ij}^{-2}(f_k)}, \\ \sigma_{ij}^{-2} &= \sum_k w(f_k)^2 \sigma_{ij}^{-2}(f_k),\end{aligned}\tag{4.10}$$

where w is the optimal weights for Ω_{GW}

$$w(f) = \frac{\Omega_{GW}(f)}{\Omega_{GW}(f_{ref})}.\tag{4.11}$$

The reference frequency used in the stochastic analysis is $f_{ref} = 25$ Hz, which is the most sensitive frequency to start with the stochastic analysis in aLIGO and AdV detectors. This stochastic analysis can be applied to SGWB of any spectral shape, by using following relation

$$\Omega_{GW}(f) = \Omega_{ref} \left(\frac{f}{f_{ref}} \right)^\alpha.\tag{4.12}$$

The final optimal estimator from all the baselines can be calculated by taking the sum over all independent baselines ij as given by

$$\hat{C} = \frac{\sum_{ij} \hat{C}_{ij} \sigma_{ij}^{-2}}{\sum_{ij} \sigma_{ij}^{-2}},\tag{4.13}$$

with variance

$$\sigma^{-2} = \sum_{ij} \sigma_{ij}^{-2}.\tag{4.14}$$

4.2.3 O3 data set

The data observed by aLIGO and AdV detectors is divided into two sets referred as O3A (first half of third observation run) and O3B (second half of

Data Set	Start Time	End Time
O3A	April 1, 2019 UTC 15:00	October 1, 2019 UTC 15:00
O3B	November 1, 2019 UTC 15:00	March 27, 2020 UTC 15:00

TABLE 4.1: Timeline of the O3 data set for aLIGO and AdV detectors. These observation time periods are defined as livetime as both aLIGO and AdV detectors were operating simultaneously.

third observation run) resulting in total of eleven months (approx) of data. The stochastic analysis is first performed for each dataset and baseline as it depends on the cross-correlating the outputs of two detectors, within the frequency range 20-1726 Hz, and then combining them in an optimal way.

Since O3 data consist of two datasets and their are three baselines, I will constraint myself to discuss only L1V1 baseline results (i.e. plots corresponding to the analysis for L1V1 baseline) for the detailed discussion about point estimates and σ value errors. Later I will use the overall results of the O3 run and the combination of O1, O2 and O3 to discuss the upper limits on SGWB.

The stochastic pipeline used the calibrated gated data L1_CWGATE_01 for L1 and V1Online for V1 detector of L1V1 baseline. To deal with the non-stationarity of the data stream each detector baseline data are divided into several time segments of 192 s duration. The 192 s intervals provides sufficient frequency resolution and are suitable to remove the sharp lines from the data. The data in each time segment are decimated from the original sampling rate 16384 Hz to 4096 Hz and high-pass filtered with a 11 Hz corner frequency. To avoid the spectral leakage from the strong line present in the data, time segments are Hann-windowed with an overlap of 50% to recover SNR, and then compute a discrete Fourier transform on each of the time segments resulting in a spectrum with frequency resolution (Δf) of 1/32 Hz. To run the stochastic search [3], a public algorithm library *MATLAB* [4] has been used.

4.2.4 Data quality cuts

Data quality cuts are highly important for the estimation of the cross-correlation between detectors to overcome sensitivity limitations due to the excess statistical errors from the non-stationary features in the data.

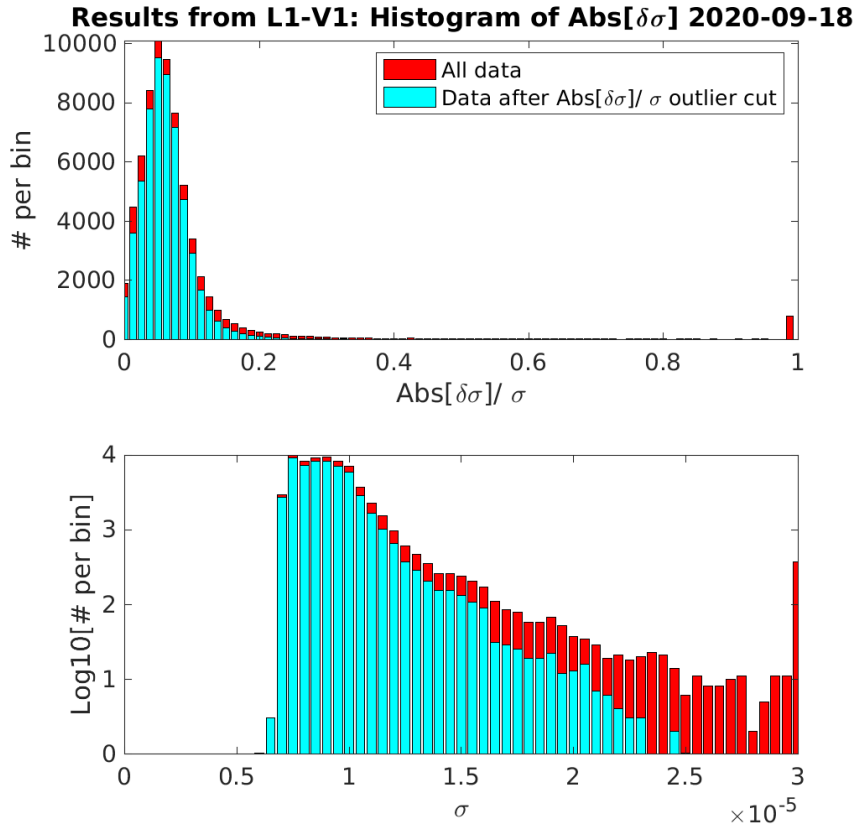


FIGURE 4.12: Histogram showing the total O3B data and data after applying the $\delta\sigma$ cut for L1V1 baseline.

Due to higher rate of loud glitches present in the O3 data (particularly in H1 and L1), the non-stationary cuts led to loss of $>50\%$ of the data while running for the data segments with duration 192 s. Specifically, these so-called delta sigma cuts remove all segments with $\delta\sigma = |\sigma - \sigma'|/\sigma = 0.2$ (see Figure 4.12) (σ is calculated from two neighbouring time intervals whereas σ' is calculated using only one time segment). These data cuts remove the outliers from the excess residual noise distribution (see Figure 4.16), consequently, making the

data more stationary. To check for the Gaussianity of the data set after the cuts, the Kolmogorov-Smirnov test can be performed for each baseline during the analysis (Figure 4.13).

Further, to encounter for the loss of data and then to improve the sensitivity of the SGWB searches, a gating procedure is applied [1]. This procedure was not necessary for AdV detector due to lower number of glitches.

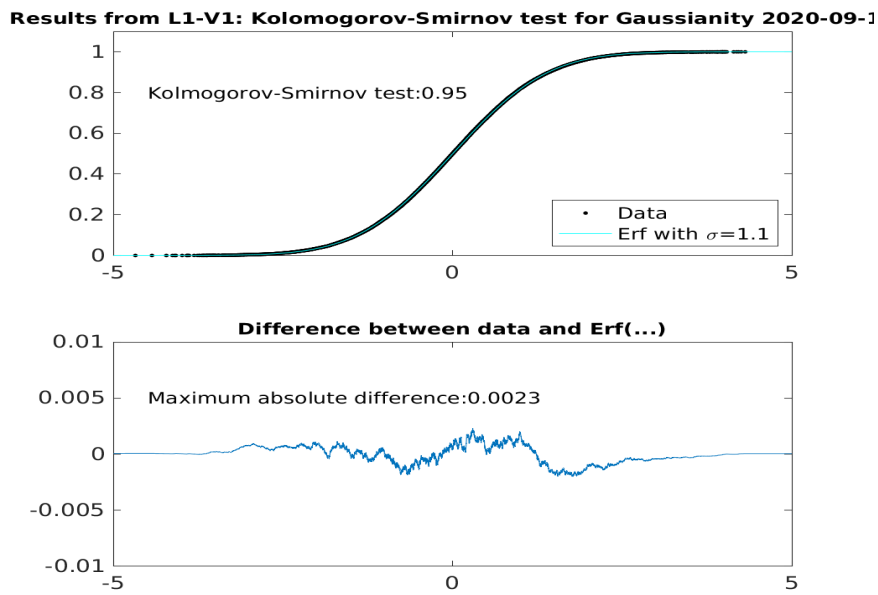


FIGURE 4.13: Kolmogorov-Smirnov test for L1V1 baseline to check for the Gaussianity of dataset after the data quality cuts applied.

4.2.5 Point estimates and sigma errors

To identify and eliminate all the contaminated frequency bins, an estimate of the coherence level between the detectors of a baseline is performed. The coherence is defined as

$$\Gamma(f) = \frac{|\langle P_{ij}(f) \rangle|^2}{\langle P_i(f) \rangle \langle P_j(f) \rangle}, \quad (4.15)$$

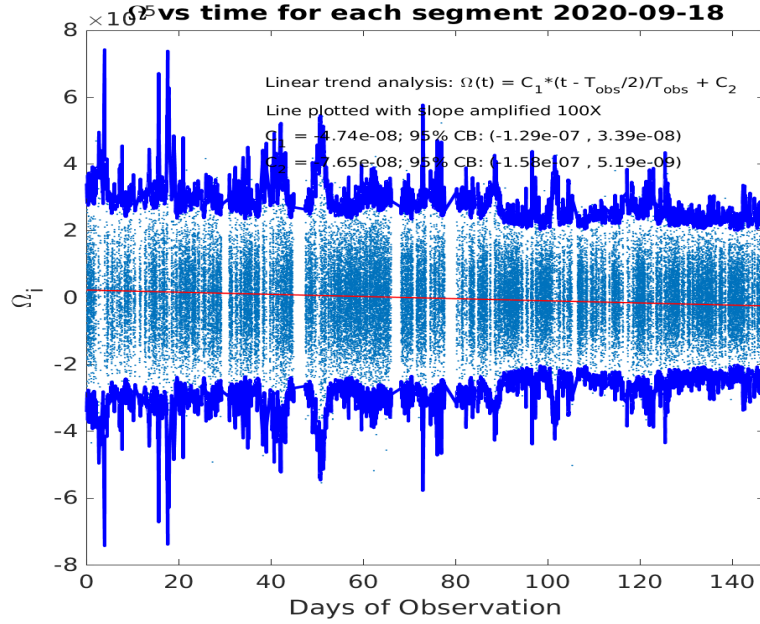


FIGURE 4.14: Plot showing the optimal estimator Ω for L1V1 baseline over the number of observation days for O3B data.

where $\langle P_{ij}(f) \rangle$ is the average CSD between the two detectors of a baseline and $\langle P_i(f) \rangle$ is the average PSD of detector i . The coherence revealed several correlated lines between each pair of detectors (H1L1, H1V1, L1V1). A list of all correlated frequency lines are given in Table 4.2 and are excluded from the final analysis to calculate the point estimates and corresponding sigma errors for each baseline.

After having all the time segments and frequency bins for the search of a SGWB in the detector data, the optimal estimator Ω and the standard errors σ are calculated by using Equation (4.10) to search for SGWB of any spectral shape by combining the cross-correlations spectra (Equation (4.8)) from different time segments using the optimal weights (Equation (4.11)). The optimal estimator and standard errors are calculated by using a frequency resolution $\Delta f = 1/32$. The optimal weighted average with σ^{-2} over all time segments and frequency bins accounts for the proper overlapping.

Baseline	Frequencies (Hz)
	20.21875, 20.25, 20.34375
H1L1	174.5625, 331.90625, 409.9375, 410.3125, 434.90625, 1083.6875, 1083.09375
H1V1	26.1875, 46-51, 87.09375, 331.90625, 410.3125, 1083.6875
L1V1	46-51, 71.25, 434.90625, 1083.09375

TABLE 4.2: Table showing the notch frequency list witnessed in both detectors of each baseline during the O3B. Notch frequencies 46-51 Hz during the O3B are due to the active damping mechanical mode around 48 Hz which were observed during the period I was contributing to AdV detector characterization (Figure 4.5 and 4.6).

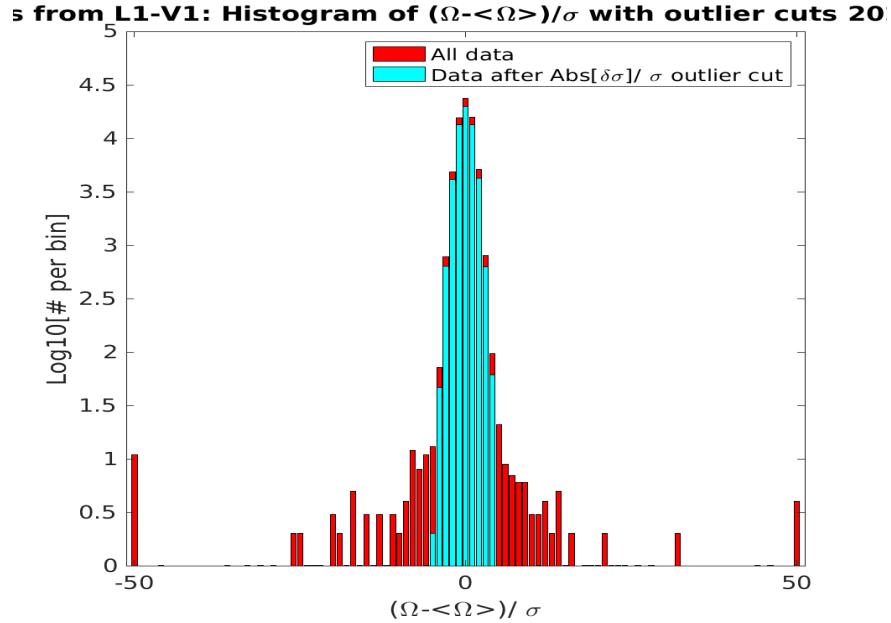


FIGURE 4.15: Histogram showing the distribution of excess residual correlated noise (i.e. ratio between standard deviation Ω and the corresponding statistical uncertainty σ_Ω) for L1V1 baseline data with 192 s segment before and after the data quality cuts.

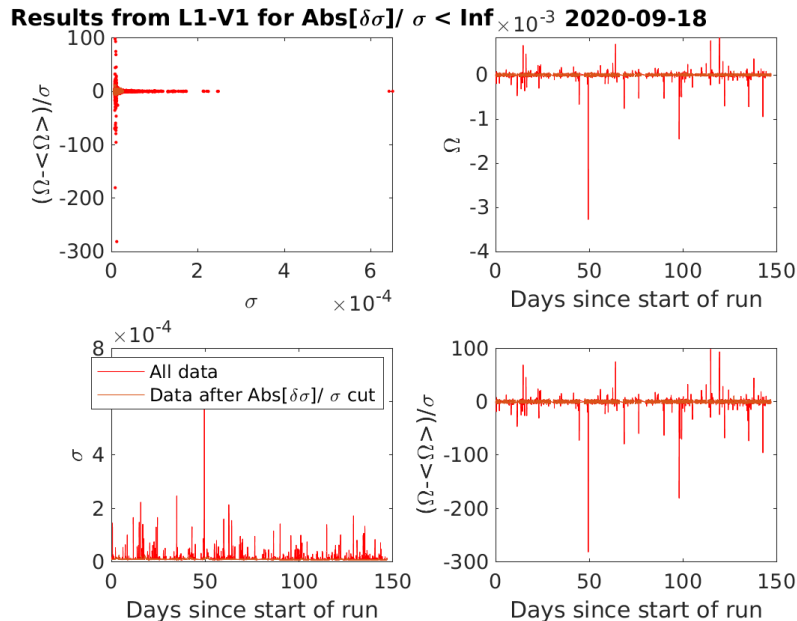


FIGURE 4.16: Plots showing the trend of optimal estimator Ω (top right), σ (bottom left), ratio of standard deviation of Ω with σ (bottom right) over the whole O3B run for L1V1 baseline.

To calculate the point estimates for a given time interval the Fourier transform of data are rebinned to the frequency resolution of the optimal filter (Equation (C.40)). These time intervals are then combined using a weighted average $1/\sigma^2$ (Equation (C.43)) to maximize the SNR (Equation (C.45)), thus accounting for the 50% overlap. A bias factor of value 1.0504 with Hubble constant 67.9 km/s/Mpc is used for the calculation of point estimates and error bars (Figure 4.17 and 4.18). The point estimates and σ error bars are then used to set upper limits on the Ω_{GW} .

4.2.6 Upper limits on SGWB

Once the point estimates are calculated, the posterior distribution point estimates and corresponding σ errors can be used to set upper limits on Ω_{GW} for a power-law spectrum with different realizations of spectral index $\alpha = 0, 2/3, 3$.

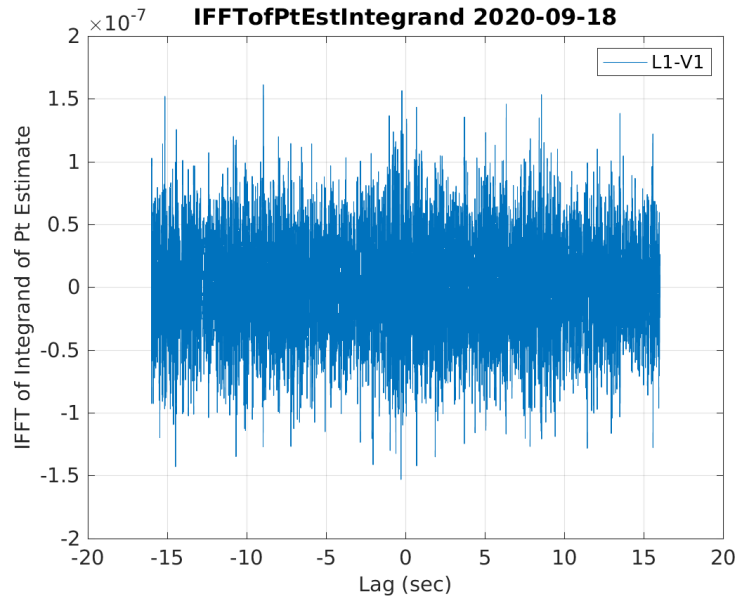


FIGURE 4.17: IFFT spectrum of point estimates for L1V1 baseline. If spectrum has a sharp features near zero lag, it could be the signature of the stochastic signal in the dataset.

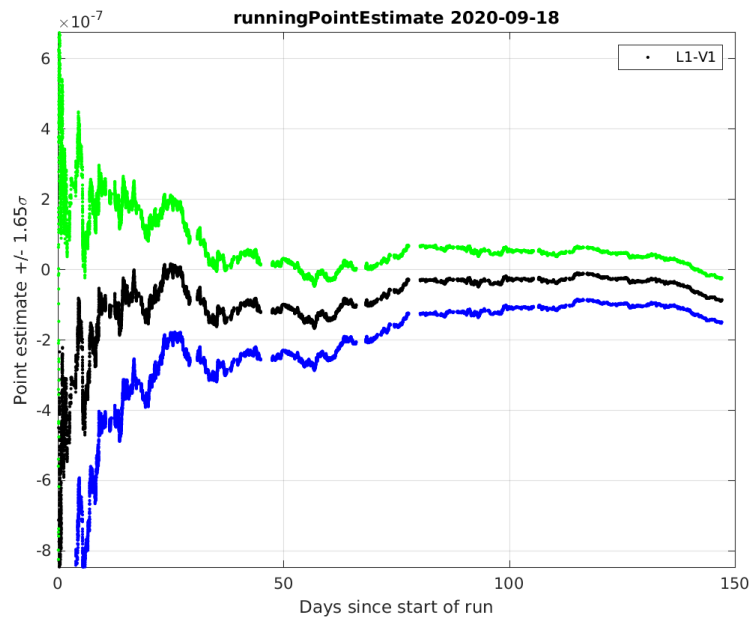


FIGURE 4.18: Running point estimates Ω are shown over the course of the run for the L1V1 baseline. In the presence of a signal the spectrum will be smooth towards the observed value. The data quality cuts have been applied for the analysis.

For a power law with index $\alpha = 0, 2/3$ ($\alpha = 0$ is for SCGWB and $\alpha = 2/3$ is astrophysical SGWB), I presented the point estimates with $\pm 1\sigma$ uncertainty from cross-correlation for each baseline (H1L1, H1V1, L1V1) in Table 4.3. Besides, I have also presented the upper limits on point estimates from all science runs (O1, O2 and O3) and a combined results (O1+O2+O3) in Table 4.4. The cross-correlation plots with $\pm 1\sigma$ uncertainty from O3 SGWB analysis for $\alpha = 0, 2/3$ are in Figure 4.19 and Figure 4.20, and a combined O1, O2 and O3 data plots for $\alpha = 0, 2/3$ are in Figure 4.21 and Figure 4.22. From Figure 4.21, one can observe that point estimates fluctuates around zero and are roughly symmetric, which is consistent with the Gaussian nature of the noise. The lines at 64 Hz in Figure 4.21 and Figure 4.22 are due to zero in ORF of H1L1 baseline.

From O1 run

The O1 run of aLIGO set a limit $\Omega_{GW} < 1.7 \times 10^{-7}$ on the energy density of SCGWB, i.e. for a flat background signal with a power-law index $\alpha = 0$ [15]. Whereas the limit on astrophysical SGWB at reference frequency $f_{ref} = 25$ Hz is $\Omega_{GW} = 1.8_{-1.3}^{+2.7} \times 10^{-9}$ with a power-law index $\alpha = 2/3$ [17].

From O2 run

The upper limit on an SCGWB in terms of the normalized energy density from aLIGO and AdV O2 run [20] is $\Omega_{GW} < 6.0 \times 10^{-8}$ with 95% credible level, i.e. for a flat background signal with a power-law index $\alpha = 0$. Whereas the upper limit on the energy density of an astrophysical SGWB is $\Omega_{GW} < 4.8 \times 10^{-8}$ at $f_{ref} = 25$ Hz with a power-law index $\alpha = 2/3$ in the frequency band 20Hz - 100 Hz [20]. On comparing O1 and O2 limits, Ω_{GW} is improved by a factor of 2.8.

Power-law Index α	$f_{99\%}^{HLL1}$ [Hz]	$\hat{C}^{HLL1}/10^{-9}$	$f_{99\%}^{HIV1}$ [Hz]	$\hat{C}^{HIV1}/10^{-9}$	$f_{99\%}^{L1V1}$	$\hat{C}^{L1V1}/10^{-9}$
0	76.1	-2.1 \pm 8.2	97.7	229 \pm 98	88.0	-134 \pm 63
2/3	90.2	-3.4 \pm 6.1	117.8	145 \pm 60	107.3	-82 \pm 40
3	282.8	-1.3 \pm 0.9	375.8	9.1 \pm 4.1	388.0	-4.9 \pm 3.1

TABLE 4.3: Isotropic SGWB searches with O3 data for power law $\alpha = 0, 2/3, 3$. For all three baselines (HLL1, HIV1, L1V1), I present the point estimates with $\pm 1\sigma$ uncertainty for cross-correlation estimates \hat{C}_{ij} . Each baseline contains 99% of the sensitivity in frequency band from 20 Hz to respective frequency level $f_{99\%}$. From the table, it is easy to see that HLL1 baseline is the most sensitive towards SGWB searches. In contrast, HIV1 and L1V1 are sensitive to SGWB searches on higher frequencies due to the longer baseline [26].

Power-law Index α	O1 [20]	O2 [20]	O3	O1+O2+O3 [26]
0	(4.4 \pm 6.0) $\times 10^{-8}$	(2.2 \pm 2.2) $\times 10^{-8}$	(-2.7 \pm 8.1) $\times 10^{-9}$	(1.1 \pm 7.5) $\times 10^{-9}$
2/3	(3.5 \pm 4.4) $\times 10^{-8}$	(2.0 \pm 1.6) $\times 10^{-8}$	(-3.7 \pm 6.0) $\times 10^{-9}$	(-0.2 \pm 5.6) $\times 10^{-9}$
3	(3.7 \pm 6.6) $\times 10^{-9}$	(3.5 \pm 2.8) $\times 10^{-9}$	(-1.1 \pm 0.9) $\times 10^{-9}$	(-0.6 \pm 0.8) $\times 10^{-9}$

TABLE 4.4: Isotropic SGWB searches with O1, O2, O3 and combined data using optimal filtering for GWs with various power-law distribution choices $\alpha = 0, 2/3, 3$. The values corresponding to α in O1, O2, O3 and O1+O2+O3 shows the point estimates and the corresponding 1σ error values for the cross-correlation estimates \hat{C}_{ij} .

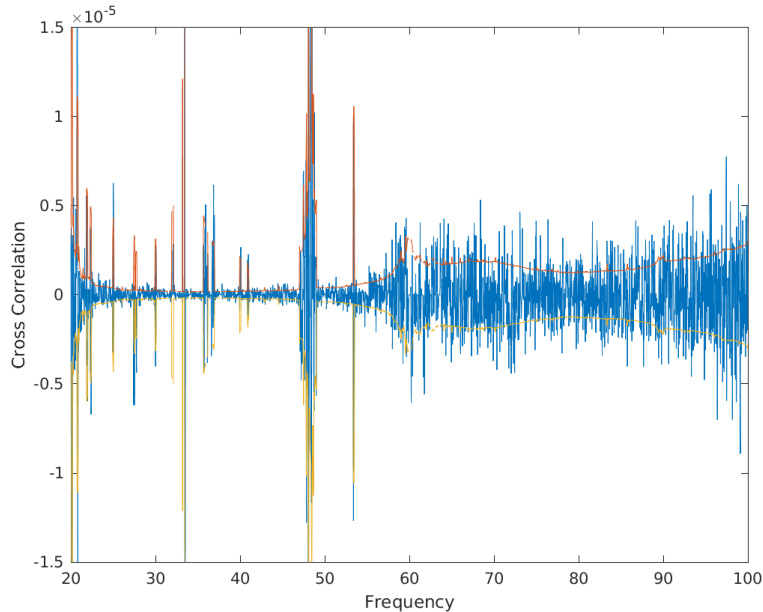


FIGURE 4.19: The cross-correlation spectrum obtained after combining the O3 run data from all baselines (H1L1, H1V1, L1V1) with a power-law index $\alpha = 0$ and $\pm 1\sigma$ uncertainty level in the red and yellow line.

from O3 run

Since there was no evidence of a SGWB in the O3 data, upper limits have been placed on Ω_{GW} at reference frequency $f_{ref} = 25$ Hz using log-uniform and uniform priors [26]. At 95% credible level, the upper limit with log-uniform (uniform) prior is $\Omega_{GW} < 5.8 \times 10^{-9}$ ($\Omega_{GW} < 1.7 \times 10^{-8}$) for power-law spectral index $\alpha = 0$. On the other hand, for power-law spectral index $\alpha = 2/3$, the upper limit with log-uniform (uniform) prior is $\Omega_{GW} = 3.4 \times 10^{-9}$ ($\Omega_{GW} = 1.2 \times 10^{-8}$). For $\alpha = 3$, log-uniform (uniform) prior sets an upper limit $\Omega_{GW} = 3.9 \times 10^{-10}$ ($\Omega_{GW} = 1.3 \times 10^{-9}$). The stochastic analysis with O3 data improves the upper limit on Ω_{GW} with log-uniform (uniform) prior by a factor of 6.0 (3.6) for $\alpha = 0$, 8.8 (4.0) for $\alpha = 2/3$ and 13.1 (5.9) for $\alpha = 3$. These improvements in the upper limits in comparison to previous runs are due to the improvement in the sensitivity of aLIGO and AdV detectors. The posterior distribution in $\Omega_{ref} - \alpha$ plane is shown in Figure 4.23.

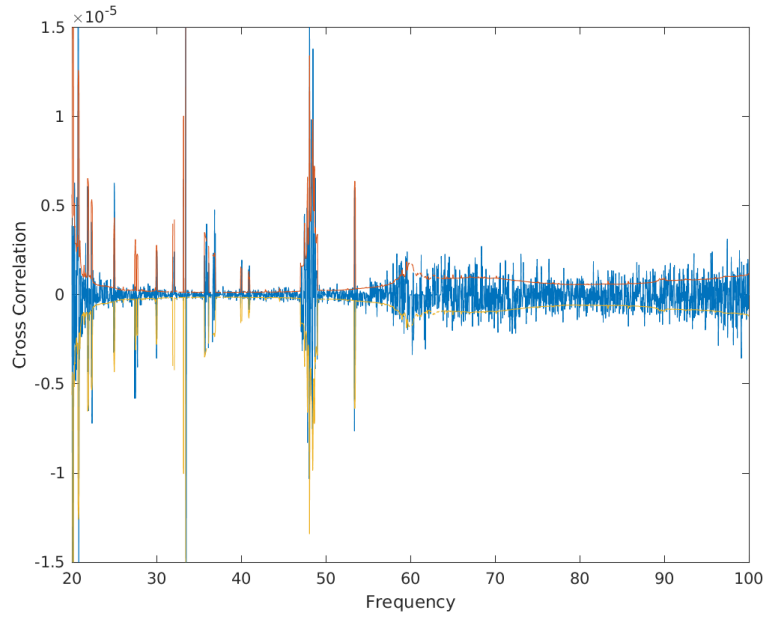


FIGURE 4.20: The cross-correlation spectrum obtained after combining the O3 run data from all baselines (H1L1, H1V1, L1V1) with a power-law index $\alpha = 2/3$ and $\pm 1\sigma$ uncertainty level in the red and yellow line.

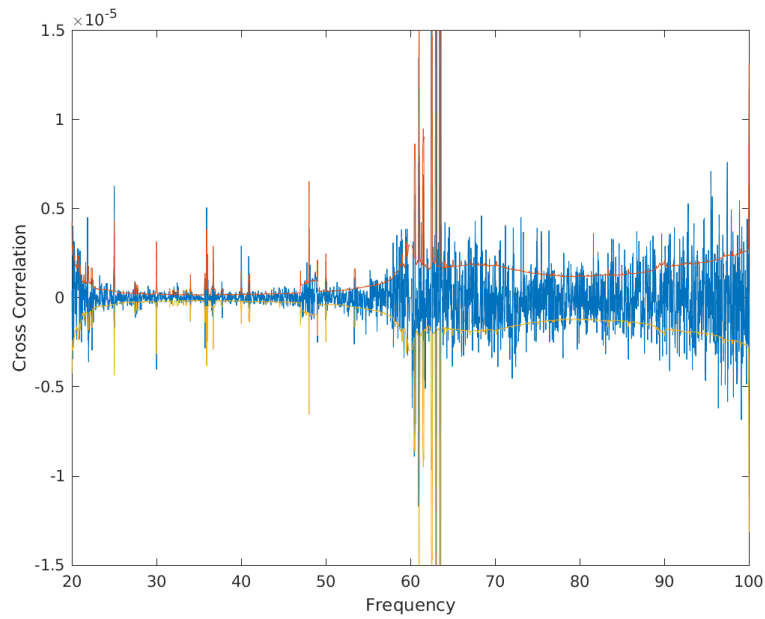


FIGURE 4.21: The cross-correlation spectrum after combining the data from H1L1 baseline in O1 and O2 run, and from all baselines (H1L1, H1V1, L1V1) in O3 run with a power-law index $\alpha = 0$. $\pm 1\sigma$ uncertainty level in shown in red and yellow line [26].

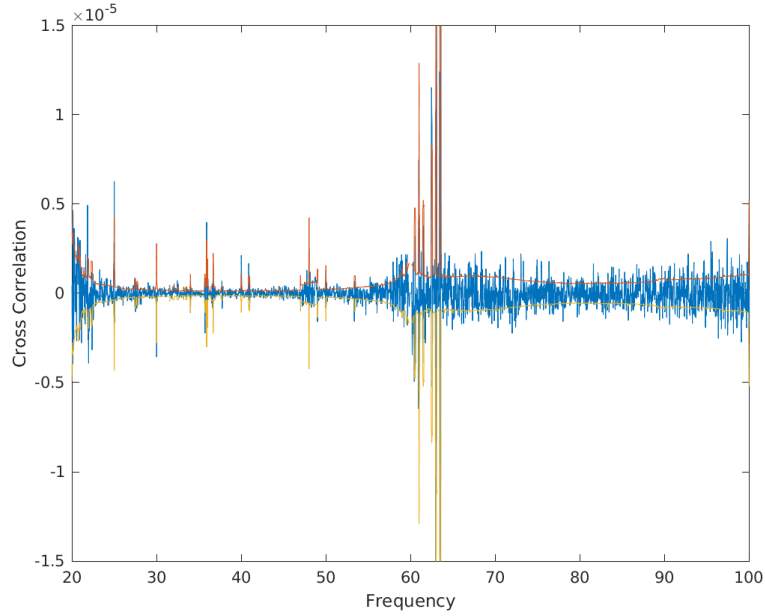


FIGURE 4.22: The cross-correlation spectrum after combining the data from H1L1 baseline in O1 and O2 run, and from all baselines (H1L1, H1V1, L1V1) in O3 run with a power-law index $\alpha = 2/3$. $\pm 1\sigma$ uncertainty level is shown in red and yellow line.

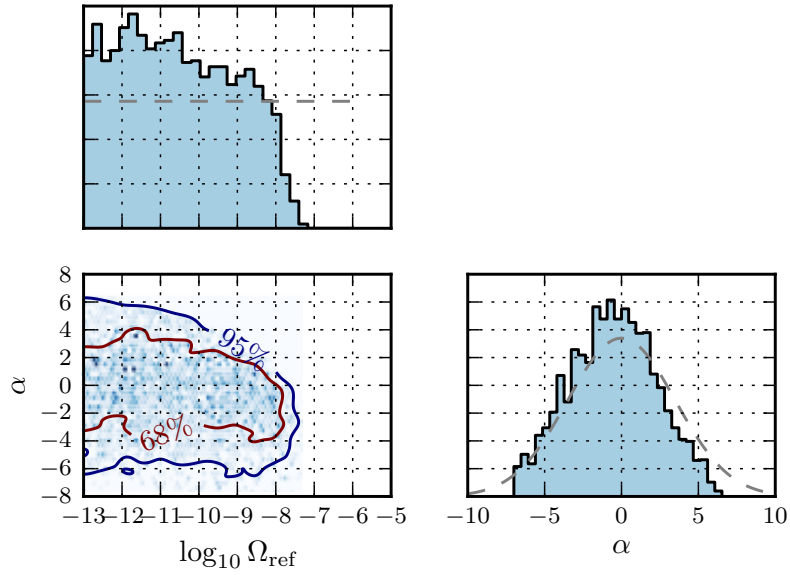


FIGURE 4.23: Corner plot for the posterior distribution for Ω_{ref} and slope α of a SGWB with a prior uniform in log of Ω_{GW} . The top and right plots show marginalized posterior for Ω_{ref} and α . While the center plot shows the 2D posterior density [26].

4.3 Conclusion

The stochastic analysis from third observation run put limits on the SGWB searches which are improved by a huge factor in comparison to previous SGWB analysis. But till now, there is no success in the detection of SGWB with current GW detectors. However, in future, with a combined search and analysis with CMB, PTA, space-borne and ground-based GW detectors, we can have the direct or statistical evidence of the SCGWB. The CMB experiments are sensitive in frequency range 10^{-20} Hz - 10^{-16} Hz, while PTAs are sensitive in 10^{-9} Hz - 10^{-7} Hz. On the other hand, space-borne GW detector will operate in frequency range 10^{-4} Hz - 1 Hz with ground-based GW detectors being sensitive in 2 Hz - 4×10^3 Hz range. With the availability of such a broad frequency spectrum in near future, we would be able observe the SGWB, to study them and set constraints on the associated parameters of the signal sources [120, 111].

Chapter 5

Conclusion and future prospects

The second-generation ground-based GW detectors finished their O3 run (from April 2019 to April 2020) with some astonishing observations [22, 21, 23, 24]. These GW observations provide us with information about the dynamics and nature of astrophysical sources, their formation rate and stellar evolution and the merger processes. Studies of these GW events will further help us to understand the nature of the SGWB formed by astrophysical sources. In addition to these astrophysical sources, various other GW signals from known and unknown sources can be detected. The GW signals from the early universe processes are among the most exciting signals. They are so faint that it would be difficult to have strong evidence in the current GW detectors.

To search for the Gaussian, isotropic, unpolarized and stationary SGWBs and their statistical evidence in the aLIGO and AdV data, since November 2018, I have been working with the stochastic group of LVC and contributed towards the data analysis. I analyzed the entire O3 dataset with the time-shifted and zero-lag runs to search for the SCGWBs. The main part of my contribution is to analyze the detector data and look for the variations in the signal (i.e. coherence variation) between the different baselines of aLIGO and AdV detector network,

using the cross-correlation method in an optimal way. I then use a stochastic energy density spectrum with a power-law distribution to search for the SGWB either from astrophysical or cosmological sources based on a power-law index which helps to put the upper limits on the respective SGWB.

A GW detector's noise limits the sensitivity of the SGWB analysis and can trigger a false SGWB. Therefore, it is crucial to study and analyze the types of sources contributing to the noise of a GW detector. These noise sources can be characterized and sometimes eliminated during the detector's observation period. For this purpose, I contributed to the DetChar group of AdV as an analysis shifter during the second half of the O3 run. During this period, I analyzed and monitored the AdV detector data (with AdV Pisa group) for the studies of glitches, a study of coherence level, improvement in the sensitivity and the number of GW events detected.

The SGWBs from the early universe (SCGWB) contain information about the processes, and the evolution of the universe occurred a few seconds after the big-bang. The future-generation GW detectors provide us with the tool to look towards the future of GW physics and their cosmological implication. For this purpose, we already have two proposed future-generation ground-based detectors ET and CE. With these future-generation GW detectors having a much better sensitivity level, than the current GW detectors, therefore, the detection of an SCGWB might become possible. Even if an SCGWB exceeds the instrument noise in correlation measurements, it would be a challenge to extract the signal and the information it is carrying because the SCGWB would be masked by a foreground of $10^5 - 10^6$ CBC signals.

This thesis presents a data analysis technique to search for the SCGWBs within the detector data in the frame of the ET and CE detector network. The data analysis model, the subtraction-noise projection method, provides us with a facility for the SCGWB searches. The method first requires to identify all the

foreground signals within the detector data stream, followed by the parameter estimation of all identified binary signals, estimating the best-fit waveforms of all identified signals. Assuming that all signals above some threshold of SNR can be detected, all the observable BBH signals present in the data stream of ET and CE detector are identified. I used *Bilby* library to performed the parameter estimation for all detected compact binary signals to estimate the best-fit waveform templates.

The estimated best-fit waveforms are then subtracted from the detector data stream in order to reduce the CBC foreground contribution, which due to mismatch between estimated and true parameters gives rise to the residual noise. On the other hand, all the unresolved sources will contribute to a confusion noise. To be able to search for an SCGWB, these residuals need to be projected out from the detector data stream and can be projected out with the use of a projection operator. I implemented projection method in a numerical way such that it does not require analytical expressions for the waveform models to calculate the projection operators (i.e. any waveform model can be used for the study of the subtraction-noise projection method without facing any difficulties). This numerical approach in the subtraction-noise projection method can be used to study and understand the role of waveform systematics associated with signal waveform models.

As a result, I demonstrated that a subtraction-noise projection method is an important approach towards the SCGWB searches, leading to the sensitivity improvement of SCGWB searches. I also conclude that with the subtraction-noise projection method, the ultimate sensitivity of SCGWB searches will not be limited by the residuals left when subtracting the estimated BBH foreground. But the fraction of the astrophysical foreground signals which cannot be detected by even with the third-generation instruments, or possibly by other signals which are not included in the analysis can limit the sensitivity towards SCGWB searches.

However, critical aspects need to be addressed in future work. First, the impact of low-SNR signals ($\text{SNR} < 10$) in the astrophysical foreground on the effectiveness of subtraction-noise projection method and then on the sensitivity of SCGWB searches needs to be investigated. Some of these signals will be visible as low threshold signals; others completely hidden in instrumental noise. Their contribution to the astrophysical foreground must be sufficiently low not to pose a fundamental limit to the capacity ET and CE have for SCGWB observations. Besides this, the second main goal is to analyze the waveform systematics. Since the foreground removal requires signal models, the dependence of the residuals on the choices of waveform models needs to be assessed, i.e. how the choice of the waveform model can impact the subtraction-noise projection method. In the future generation GW detectors, matched-filter based analyses will also face a challenge with the increase in detection rate and computationally expensive parameter estimation. Therefore, I would like to investigate our analysis concerning waveforms, their systematics and how these challenges can be overcome.

Appendix A

IMRPhenomPv2 waveform model

The coalescing BBHs are categorized into different types, namely spinning (or no-spin), aligned-spin (non-aligned spin) and precessing (non-precessing), depending upon their orientation with respect to the individual BBH spin. Most of BBH studies are focused on the GW signal from spin-zero or aligned spin BBHs, i.e. spin is aligned to the orbital angular momentum of the BBH. These simpler BBH models in aligned spin (or the precessing BBH models) accurately approximate the waveforms for further studies. These waveform includes the inspiral phase (where two BBHs are separated enough for the PN theory to be valid), the merger of BBH (where the NR part plays a role) and then the ringdown phase (a post-merger process to form the final object). During the past decade, studies to understand the BBH signals led to the construction of various waveforms which are now being used for the GW signal searches. At present, there are two leading families of the GW waveforms for BBHs namely IMR phenomenological (IMR-Phenom) and surrogate waveforms (SEOBNR) [158, 128, 95, 164, 46, 67], and are under continuous development. In here, I will focus mainly on the IMRPhenom family of the BBH waveforms.

The IMRPhenom waveforms are constructed for the BBH system by joining the analytical PN and the EOB for the inspiral part with the NR results to construct a complete IMRPhenom waveform in the frequency domain. In IMRPhenom waveform family, we have a set of the IMRPhenom waveforms depending upon the spin or the higher modes (special harmonic modes) of BBH [32, 150, 151], and the EOB [49, 50] waveforms to describe the full spectrum from the inspiral to the merger phase. With the help of NR waveforms, unknown EOB coefficients are calibrated to describe the merger-ringdown processes.

In this subsection, without carrying out full extensive calculations in the PN and the NR part, the combining process of these two parts for the generation of IMRPhenom waveforms is presented.

A.1 PN and NR waveforms

PN part

In the weak field approximation of Einstein Field equation, the PN approach can be used to construct the waveforms accurately. The GW signal we observe with a GW detector is characterized by binaries individual masses (m_1 and m_2) and the total mass as given

$$\begin{aligned}\eta &= \frac{m_1 m_2}{M^2}, \\ \mathcal{M}_c &= \eta^{3/5} M,\end{aligned}\tag{A.1}$$

where η is symmetric mass ratio, $M = m_1 + m_2$ is total mass and \mathcal{M}_c is the chirp mass. The magnitude of the spin of a BBH is

$$S_i = |\chi_i| m_i^2, \quad i = 1, 2, \quad (\text{A.2})$$

where χ_i is a dimensionless parameter whose magnitude and sign depend upon the sign of $\mathbf{L} \cdot \mathbf{S}_i$ (\mathbf{L} is the orbital angular momentum) telling us about the alignment of the spin of binaries. If χ has a positive value, the BBH is aligned-spin and if χ has negative value, BBH is non-aligned spin. Now in case of aligned spin or non-precessing binary system, χ is written as

$$\chi_i = \frac{\mathbf{S}_i \cdot \mathbf{L}}{m_i^2}, \quad \chi_i \in [-1, 1]. \quad (\text{A.3})$$

In Phenom models, spin dependence of a model can be parameterized by using a single effective spin parameter [105]

$$\chi_{eff} = \frac{m_1 \chi_1 + m_2 \chi_2}{M}, \quad (\text{A.4})$$

where χ_{eff} is an effective spin parameter used to parametrize the spin of the waveform. In the PN approximation, the leading-order effect of spin on the binary's inspiral phasing is [31, 105] given by

$$\chi_{PN} = \chi_{eff} - \frac{38\eta}{113}(\chi_1 + \chi_2), \quad (\text{A.5})$$

and is a better approximation to be used in IMR models [132].

NR part

In order to estimate spin, η and χ_{PN} need to be drawn from a wide range of these parameters. The NR part of a waveform is calculated in Newman-Penrose scalar Ψ_4 , a complex function encoding the two polarizations of GW perturbation through the relation [151]

$$\begin{aligned}\Psi_4 &= \frac{d^2 h(t)}{dt^2}, \\ &= \frac{d^2}{dt^2} [h_+(t) - ih_\times(t)].\end{aligned}\tag{A.6}$$

To move from Ψ_4 to the GW term, h needs to be integrated two times. In frequency domain, the GW strain is

$$h = h_+ - ih_\times.\tag{A.7}$$

Hence from Equation (A.6), we have [151]

$$\tilde{h}_{NR} = -\frac{\tilde{\Psi}_4(f)}{4\pi^2 f^2} = A_{NR}(f)e^{i\Phi_{NR}(f)},\tag{A.8}$$

where terms with \sim sign denotes the Fourier transformation and A_{NR} gives the amplitude of the NR waveform.

A.2 Phenom waveform

By matching the PN and the NR parts over time and phase shift, one can formulate a hybrid waveform with a scale factor a , which reduces the amplitude difference between these two parts. Thus the combined waveform is given by [31]

$$h(t) = a\tau(t) h_{NR}(t) + (1 - \tau(t)) h_{PN}(t) < \tau, \quad \tau \in [0, 1],\tag{A.9}$$

where τ is a weighting factor and a is a scale factor. To understand the various IMRPhenom waveforms for BBHs, one can use

$$h(f) = A_{eff}(f)e^{\Psi_{eff}(f)}, \quad (\text{A.10})$$

where A_{eff} and Ψ_{eff} are the effective amplitude and the effective phase, using Equation (A.10) one can see how the values of A_{eff} and Ψ_{eff} change with the choice of a BBH system.

PhenomA

The PhenomA waveform consist of the merger and the ringdown phase with corresponding frequencies, f_{merger} and f_{ring} , and a cut off frequency f_{cut} . Thus, A_{eff} is [31]

$$A_{eff} = \mathcal{A}f_{merger}^{-7/6} \begin{cases} \left(\frac{f}{f_{merger}}\right)^{-7/6} & \text{if } f < f_{merger} \\ \left(\frac{f}{f_{merger}}\right)^{-2/3} & \text{if } f_{merger} \leq f \leq f_{ring} \\ (w\mathcal{L}(f, f_{ring}, \bar{\sigma})) & \text{if } f_{ring} \leq f \leq f_{cut}, \end{cases} \quad (\text{A.11})$$

where \mathcal{A} is a numerical constant and depends upon the BBHs individual masses, sky-localization and the BBH orientation. w is normalization constant chosen such that A_{eff} is continuous across f_{ring} and $\mathcal{L}(f, f_{ring}, \bar{\sigma})$ is a Lorentzian function centred around f_{ring} with a width $\bar{\sigma}$. f_{merger} is the transition frequency at which power-law changes. Parameters f_{ring} , f_{merger} , f_{cut} and $\bar{\sigma}$ can be obtained during the matching of PN and NR parts. Thus, the effective phase is [31]

$$\Psi_{eff}(f) = 2\pi ft_c + \phi_c + \frac{1}{\eta} \sum_{k=0}^7 (x_k \eta^2 + y_k \eta + z_k) (\pi M f)^{(k-5)/3}, \quad (\text{A.12})$$

where t_c and ϕ_c are the coalescence time and the phase of the coalescence. The accuracy of PhenomA waveform can be parameterized by using $m_1/m_2 \equiv q \leq 4$ and $50 \leq M/M_\odot \leq 200$ [31].

PhenomB

PhenomB waveform is the extension of PhenomA waveform for non-precessing spinning (aligned spin) BBH with a single spin factor χ . The effective amplitude A_{eff} can be written as (for more information see [32])

$$A_{eff}(f) = \mathcal{A}f_1^{-7/6} \begin{cases} (f/f_1)^{-7/6} (1 + \sum_{i=2}^3 \alpha_i v^i) & \text{if } f < f_1 \\ w_m (f/f_1)^{-2/3} (1 + \sum_{i=1}^2 \epsilon_i v^i) & \text{if } f_1 \leq f \leq f_2 \\ w_r \mathcal{L}(f, f_2, \bar{\sigma}) & \text{if } f_2 \leq f \leq f_{cut}, \end{cases} \quad (\text{A.13})$$

where f_1, f_2 are transition frequencies respectively and $v = (\pi M f)^{1/3}$, α_i are the PN corrections to the waveform, expressed in terms of η and χ . The term ϵ_i can be estimated from the waveform and depends on the spin parameter χ . w_m and w_r are normalization constants chosen such that A_{eff} is continuous across f_2 and f_1 . Hence, the effective phase Ψ_{eff} is [32]

$$\Psi_{eff} = 2\pi f t_c + \phi_c + \frac{2}{128\eta v^5} \left(1 + \sum_{k=2}^7 \psi_k v^k \right). \quad (\text{A.14})$$

Coefficients in PhenomB waveform model are in the range $q \leq 10$ and $M \leq 400M_\odot$.

PhenomC

PhenomC waveform is developed for nonprecessing spinning BBHs (for more details see [151]) with more accuracy than PhenomB waveform. The effective amplitude is calculated by adding the amplitude from the pre-merger (PM) process and the ringdown amplitude (RD) as given

$$A_{eff} = A_{PM}(f)w_{f_0}^- + A_{RD}w_{f_0}^+, \quad (\text{A.15})$$

where A_{PM} and A_{RD} are the pre-merger and the ringdown amplitudes respectively with frequency f_0 . The + and - signs (at frequency f_0) represent the transition between different regimes of window function w to produce the full PhenomC waveform phase $\Phi_{eff}(f)$

$$w^\pm = \frac{1}{2} \left[1 \pm \tanh \left(\frac{4(f - f_0)}{d} \right) \right], \quad (\text{A.16})$$

f_0 can be determined by $f_0 = 0.98f_{RD}$ and $d = 0.0015$. The pre merger amplitude A_{PM} is calculated by combining the PN inspiral amplitude A_{PN} with a higher order term as follows

$$\begin{aligned} A_{PM}(f) &= A_{PN}(f) + \rho_1 f^{5/6}, \\ A_{PN}(f) &= C\Theta^{-7/6} \left(1 + \sum_{k=2}^5 \rho_k \Theta^{k/3} \right), \end{aligned} \quad (\text{A.17})$$

where ρ_1 is the coefficient for the pre-merger amplitude with $\Theta = \pi M f$. Now the amplitude during the ringdown phase is

$$A_{RD} = \delta_1 \mathcal{L}(f, f_{RD}(a, M), \delta_2 Q(a)) f^{-7/6}, \quad (\text{A.18})$$

where δ_1, δ_2 , accounts for the overall amplitude and errors in the fit of the pre-merger and the ringdown phase, $\mathcal{L}(f, f_0, \sigma)$ is Lorentzian function, Q is a quality factor and depends only on the BBH spin a . Thus the effective phase in terms of the inspiral phase ψ_{SPA} , the pre-merger phase ψ_{PM} and the ringdown phase ψ_{RD} given by

$$\begin{aligned}
 \Psi_{eff} &= \psi_{SPA} w_{f_1}^- + \psi_{PM} w_{f_1}^+ w_{f_2}^- + \psi_{RD} w_{f_2}^+, \\
 \psi_{PM} &= \frac{1}{\eta} (\alpha_1 f^{-5/3} + \alpha_2 f^{-1} + \alpha_3 f^{-1/3} + \alpha_4 + \alpha_5 f^{2/3} + \alpha_6 f), \\
 \psi_{RD} &= \beta_1 + \beta_2 f,
 \end{aligned} \tag{A.19}$$

where $f_1 = 0.1 f_{RD}$, $f_2 = f_{RD}$ and $d = 0.005$. The transition points in the frequency at f_1 and f_2 , where the NR part starts to play a role, provide the best match between the PN, PM and RD part. The coefficients α_i for $i = 1, 2, \dots, 6$ are used for fitting the PN and the NR waveform parts in the regions between frequencies f_1 and f_2 , and they depend upon the spin and masses of the BBHs, while $\beta_{1,2}$ are from the slope of the phase transition at point f_2 .

The Phenom waveform models PhenomA, PhenomB and PhenomC consider the dominance of the spin on the GW phase due to an individual spin of BBH. Hence, waveform relies only on two parameters: the symmetric mass ratio (Equation (A.1)) and the single effective spin parameter (Equation (A.4)). This simplification led to the extension of PhenomC to produce a non-precessing BBH PhenomP waveform. In comparison, the rest of all parameters can be chosen as per study requirements [89].

PhenomD

A pivotal part of the accurate waveform is to approximate the final masses and spin of a BBH with the least uncertainties. The Phenom waveforms use a Lorentzian function, which can lead to an incorrect behaviour at the high frequencies. Thus the numerical evaluations can be improved by incorporating a modification in Lorentzian, in the amplitude and in the phase of a waveform [100, 105], to improve the waveform accuracy.

A PhenomD waveform consists of simple-harmonic modes of GW $l = 2$ and $|m| = 2$. Since these modes are the dominating modes in the aligned-spin BBH system, the physical parameter space is given by $\chi \in [M, \eta, \chi_1, \chi_2]$. Thus the GW strain is

$$\tilde{h}_{22}(f; \chi) = A(f; \chi)e^{-i\Psi(f; \chi)}, \quad (\text{A.20})$$

The overall IMR phase for PhenomD waveform is

$$\Phi_{eff} = \phi_{Ins}(f)\vartheta_{f_1}^- + \vartheta_{f_1}^+\phi_{Int}(f)\vartheta_{f_2}^- + \vartheta_{f_2}^+\phi_{MR}(f), \quad (\text{A.21})$$

where ϑ is the step function which is given as

$$\vartheta_{f_0}^\pm = \frac{1}{2}[1 \pm \vartheta(f - f_0)], \quad (\text{A.22})$$

ϕ_{Ins} , ϕ_{Int} and ϕ_{MR} are the inspiral, the intermediate (between the inspiral and the merger-ringdown phase) and the merger-ringdown phases respectively, and defined as

$$\begin{aligned} \phi_{Ins} &= \phi_{TF2}(M, f; \chi) + \frac{1}{\eta} \left(\sigma_0 + \sigma_1 f + \frac{3}{4}\sigma_2 f^{3/4} + \frac{3}{5}\sigma_3 f^{5/3} + \frac{1}{2}\sigma_4 f^2 \right), \\ \phi_{TF2} &= 2\pi f t_c - \varphi - \frac{\pi}{4} + \frac{3}{128\eta} (\pi f M)^{-5/3} \sum_{i=0}^7 \varphi_i(\chi) (\pi f M)^{i/3}, \\ \phi_{Int} &= \frac{1}{\eta} \left(\beta_0 + \beta_1 f + \beta_2 \text{Log}(f) - \frac{\beta_3}{3} f^{-3} \right), \\ \phi_{MR} &= \frac{1}{\eta} \left(\alpha_0 + \alpha_1 f - \alpha_2 f^{-1} + \frac{4}{3}\alpha_3 f^{3/4} + \alpha_4 \tan^{-1} \left(\frac{f - \alpha_5 f_{RD}}{f_{damp}} \right) \right), \end{aligned} \quad (\text{A.23})$$

where α_i, β_i are the fitting parameters (phase coefficients) and σ_i are the phenomenological fitting coefficients over the frequency Mf , and $\varphi_i(\chi)$ are the PN expansion coefficients and are the functions of BBH parameters, ϕ_{TF2} is a TaylorF2 waveform phase term used to incorporate higher-order terms into the PN inspiral phase. f_{RD} is the final BBH ringdown frequency and f_{damp} is ringdown damping frequency. The amplitude is given as a sum of amplitudes for different regions

$$A_{eff} = A_{Ins}(f)\vartheta_{f_1}^- + \vartheta_{f_1}^+ A_{int}(f)\vartheta_{f_2}^- + \vartheta_{f_2}^+ A_{MR}(f), \quad (\text{A.24})$$

and the respective inspiral, intermediate and merger-ringdown amplitudes are

$$\begin{aligned} A_{Ins}(f) &= A_{PN} + A_0 \sum_{i=1}^3 \rho_i f^{6+i}/3, \\ A_{PN}(f) &= A_0 \sum_{i=0}^6 \mathcal{A}_i (\pi f)^{i/3}, \\ A_{Int}(f) &= A_0 (\delta_0 + \delta_1 f + \delta_2 f^2 + \delta_3 f^3 + \delta_4 f^4), \\ A_{MR}(f) &= A_0 \left(\gamma_1 \frac{\gamma_3 f_{damp}}{(f - f_{RD})^2 + (\gamma_3 f_{damp})} e^{-\frac{\gamma_2(f-f_{RD})}{\gamma_3 f_{damp}}} \right), \end{aligned} \quad (\text{A.25})$$

where A_{PN} is the PN amplitude for the PhenomD waveform, ρ_i is the amplitude coefficient, A_0 is the normalization factor $\sqrt{(2\eta)/(3\pi^{-1/3})}f^{-7/6}$ and \mathcal{A}_i are the expansion coefficients. δ_i provides the solution to a system of equations [105], γ_1 gives the overall amplitude of the ringdown phase and γ_2, γ_3 gives the decay rate and the increase in the width of a damping frequency f_{damp} .

Incorporating the waveforms IMRPhenomP and IMRPhenomD together, they can be used for the studies of BBH systems with higher mass ratio and higher spin components.

Appendix B

Detector's geometrical factors

The detector geometry plays an integral part in the detection of various features of a GW signal. Besides this, detector geometry is also crucial for the optimal sensitivity and the data analysis tools. In this section, I will focus on the critical geometrical factors of a GW detector and how they manifest themselves into the detector data playing an essential role in the GW detection and searches.

B.1 Antenna response function

To understand the effect of a detector geometry on the SGWB searches, consider a GW signal in TT gauge (check Equation (1.11)), then the amplitude of a plane wave is [35]

$$h_{ab}(t, \vec{x}) = \sum_A \int_{-\infty}^{+\infty} df \int_{S^2} d\hat{\Omega} h_A(f, \hat{\Omega}) e^{-2\pi i f(t - \hat{\Omega} \cdot \vec{x}/c)} e_{ab}^A(\hat{\Omega}), \quad (\text{B.1})$$

where $\hat{\Omega}$ is the unit vector pointing along the propagation direction of a GW on two sphere with the wave vector $\vec{k} = 2\pi f \hat{\Omega}/c$, c is the speed of light and

$d\hat{\Omega} = d\cos\theta d\phi$. $e_{ab}^A(\hat{\Omega})$ is the polarization tensor (for the two polarizations $A = +, \times$) given by

$$\begin{aligned} e_{ab}^+(\hat{\Omega}) &= \hat{m}_a\hat{m}_b - \hat{n}_a\hat{n}_b, \\ e_{ab}^\times(\hat{\Omega}) &= \hat{m}_a\hat{n}_b + \hat{n}_a\hat{m}_b, \end{aligned} \tag{B.2}$$

where \hat{m} and \hat{n} are unit vectors defined as

$$\begin{aligned} \hat{\Omega} &= \cos\phi \sin\theta \hat{x} + \sin\phi \sin\theta \hat{y} + \cos\theta \hat{z}, \\ \hat{m} &= \sin\phi \hat{x} - \cos\phi \hat{y}, \\ \hat{n} &= \cos\phi \cos\theta \hat{x} + \sin\phi \cos\theta \hat{y} - \sin\theta \hat{z}, \end{aligned} \tag{B.3}$$

in terms of the polar and the azimuthal angles (θ, ϕ) . Since GW detectors are sensitive to the displacement produced along the detector arms, the strain $h(t)$ will have the form

$$h(t) = D^{ab}h_{ab}(t, \vec{x}), \tag{B.4}$$

where D^{ab} is known as the detector tensor and can be defined in unit vectors \hat{X}^a and \hat{Y}^a pointing along the direction of the detector arms

$$D^{ab} = h_{ab}(t) \frac{1}{2} \left(\hat{X}^a \hat{X}^b - \hat{Y}^a \hat{Y}^b \right). \tag{B.5}$$

Therefore, from Equation (B.4) we can write

$$h(t) = \sum_A \int_{-\infty}^{+\infty} df \int_{S^2} d\hat{\Omega} h_A(f, \hat{\Omega}) e^{-2\pi i f(t - \hat{\Omega} \cdot \vec{x}/c)} D^{ab} e_{ab}^A(\hat{\Omega}), \quad (\text{B.6})$$

defining a function F_A , such that

$$F^A(\hat{\Omega}) = D^{ab} e_{ab}^A(\hat{\Omega}), \quad (\text{B.7})$$

where $F^A(\hat{\Omega})$ is the antenna pattern function which gives the response of a GW detector to zero frequency, unit amplitude with the two polarizations. $F^A(\hat{\Omega})$ depends upon the direction of propagation of the GW ($\hat{\Omega}$) and also on the polarization tensor $e_{ab}^A(\hat{\Omega})$. Thus from Equation (B.6), we have

$$\begin{aligned} h(t) &= \sum_A \int_{-\infty}^{+\infty} df \int_{S^2} d\hat{\Omega} h_A(f, \hat{\Omega}) e^{-2\pi i f(t - \hat{\Omega} \cdot \vec{x}/c)} F^A(\hat{\Omega}), \\ &= \sum_A \int_{-\infty}^{+\infty} d\hat{\Omega} \tilde{h}_A(f, \hat{\Omega}) F^A(\hat{\Omega}), \end{aligned} \quad (\text{B.8})$$

where $\tilde{h}_A(f, \hat{\Omega})$ is the Fourier transform of the signal $h_A(f, \hat{\Omega})$ which can be simplified further as given

$$h(t) = F^+ h_+(t) + F^\times h_\times(t). \quad (\text{B.9})$$

By using Equations (B.2), (B.3) with (B.7), we will have the following relations of $F^A(\hat{\Omega})$ for a GW detector with perpendicular arms

$$\begin{aligned} F_+^{90^\circ}(\theta, \phi, \psi) &= \frac{1}{2} (1 + \cos^2\theta) \cos 2\phi \cos 2\psi - \cos\theta \sin 2\phi \sin 2\psi, \\ F_\times^{90^\circ}(\theta, \phi, \psi) &= \frac{1}{2} (1 + \cos^2\theta) \cos 2\phi \sin 2\psi + \cos\theta \sin 2\phi \cos 2\psi, \end{aligned} \quad (\text{B.10})$$

with a normalization factor given as (F^A is independent of ψ as it is a linear combination of $F_+^2 + F_\times^2$ in the expectation value of Equation (B.8))

$$F \equiv \sum_A \int_{S^2} d\hat{\Omega} F^A(\hat{\Omega}) F^A(\hat{\Omega}) = \frac{8\pi}{5}. \quad (\text{B.11})$$

The above Equations are true for the current generation GW detectors and also for the third-generation GW detector CE, but this would not be the case for ET detector. In the case of ET, three detectors would be at an angle of 60° with respect to each other, hence, the antenna pattern function will change. From [136] we can write down the Equation (B.5) as

$$\begin{aligned} D^1 &= h_1 \frac{1}{2} (X^1 \otimes X^1 - X^2 \otimes X^2), \\ D^2 &= h_2 \frac{1}{2} (X^2 \otimes X^2 - X^3 \otimes X^3), \\ D^3 &= h_3 \frac{1}{2} (X^3 \otimes X^3 - X^1 \otimes X^1), \end{aligned} \quad (\text{B.12})$$

where X^i , $i = 1, 2, 3$ are the unit vectors in $x - y$ plane along the three arms of the ET detector defined as

$$\begin{aligned} X^1 &= \frac{1}{2} (\sqrt{3}, -1, 0), \\ X^2 &= \frac{1}{2} (\sqrt{3}, 1, 0), \\ X^3 &= \frac{1}{2} (0, 1, 0). \end{aligned} \quad (\text{B.13})$$

In a similar manner to Equation (B.10), we can have the relations for ET detector as follows

$$\begin{aligned}
 F_+^{60^\circ}(\theta, \phi, \psi) &= \frac{\sqrt{3}}{2} \left[\frac{1}{2} (1 + \cos^2\theta) \cos 2\phi \cos 2\psi - \cos\theta \sin 2\phi \sin 2\psi \right], \\
 F_\times^{60^\circ}(\theta, \phi, \psi) &= \frac{\sqrt{3}}{2} \left[\frac{1}{2} (1 + \cos^2\theta) \cos 2\phi \sin 2\psi + \cos\theta \sin 2\phi \cos 2\psi \right].
 \end{aligned} \tag{B.14}$$

On comparing Equations (B.10) and (B.14), one can observe that the antenna pattern function for a GW detector with an arm opening at 60° is smaller than the detector with 90° by a factor of $\sqrt{3}/2$. The overall antenna pattern function for the three ET detectors would be

$$F^2 = \sum_{i=1}^3 (F_+^i)^2 + (F_\times^i)^2. \tag{B.15}$$

The three ET detector will enhance the overall detector response by a factor of $\sqrt{3}$ [136] making it sensitive to cover the whole sky for a GW signal detection.

Appendix C

Data Analysis Tools

C.1 Introduction to statistical inference

Statistical inference is a crucial analysis tool to check for the presence of a GW signal in the detector data and to constrain the parameters of that particular signal. There are mainly two inference approaches being followed by GW analysis community; the first one is the Frequentist inference approach, and the second one is the Bayesian inference approach. These approaches are related to their interpretations of the probability. In the Frequentist approach, the probability is related to the frequency of an event. Whereas in the Bayesian approach, probability depends upon the prior knowledge about the event.

To put it into an example, consider a BBH signal (with parameters λ) is present in the detector data s . Therefore in the Frequentist approach, parameters λ have true and fixed values, but the quantity that matters the most is uncertainty in the detector data and the probability to measure it for a given GW signal parametrized by λ . Hence the likelihood probability distribution can be denoted as $p(s|\lambda)$. Contrary to the Frequentist inference approach, the

Bayesian inference is based on the uncertainties in λ , i.e. λ have particular values for the observed detector data s giving the posterior probability distribution $p(\lambda|s)$.

The likelihood function and the posterior probability distribution are related to each other through the relation

$$p(\lambda|s) = \frac{p(s|\lambda)p(\lambda)}{p(s)}. \quad (\text{C.1})$$

The relationship in Equation (C.1) is known as Bayes theorem. The term $p(\lambda|s)$ is the posterior density function (PDF), $p(\lambda)$ is the prior probability distribution of binary source parameters λ and $p(s)$ is known as marginalized likelihood or evidence given by

$$p(s) = \int p(s|\lambda)p(\lambda)d\lambda. \quad (\text{C.2})$$

The prior probability distribution (a vital quantity for the Bayesian approach) provides with the knowledge on the distribution and the range of parameters λ . In contrast, likelihood function helps to understand the nature of the measured detector noise and the measured signal. Beside estimating source parameters, these statistical inference approaches are also used for the model and hypothesis selection of a GW signal present in the observed GW data.

Since in my studies, I only used the Bayesian approach for the parameter estimation, I will limit the discussion to the Bayesian approach. A detailed study of the Frequentist and the Bayesian approaches can be found in [143].

C.2 Bayesian inference

This section introduces the Bayesian inference with a mathematical framework and its implementation to perform the tasks in GW data analysis, i.e. to extract the source parameters and properties from the given detector data and to test the hypothesis. In Bayesian inference, for a given data stream s , source parameters λ are estimated as a posterior distribution $p(\lambda|s)$ (see Equation (C.1)).

C.2.1 Bayesian parameter estimation

Equation (C.1) represents the most straightforward case for parameter estimation. However, for the parameter estimation of a GW signal, this is not the case, as we have higher-dimensional parameter space making it more challenging to interpret the posterior distribution.

To do this, consider a model (which can be a BBH, BNS or NSBH) \mathcal{H}_α , where α runs over different models with known parameters λ_α (where $\alpha = 1, 2 \dots N_p$ gives the total number of parameters used to characterize the GW signal) providing the description of detector data stream s . Thus the posterior probability distribution can be written from Equation (C.1) as

$$p(\lambda_\alpha|s, \mathcal{H}_\alpha) = \frac{p(s|\lambda_\alpha, \mathcal{H}_\alpha)p(\lambda_\alpha|\mathcal{H}_\alpha)}{p(s|\mathcal{H}_\alpha)}. \quad (\text{C.3})$$

Equation (C.3) is termed as the joint posterior distribution and represents the posterior distribution is given by a likelihood function weighted by the prior probability distribution. With the evaluation of the posterior, we will have information about all the parameters in the detector data stream s . Thus the marginalized likelihood function is

$$p(s|\mathcal{H}_\alpha) = \int p(s|\lambda_\alpha, \mathcal{H}_\alpha)p(\lambda_\alpha|\mathcal{H}_\alpha)d\lambda_\alpha, \quad (\text{C.4})$$

where marginalization is taken over the model parameter values. The posterior probability distribution $p(\mathcal{H}_\alpha|s)$ for a model \mathcal{H}_α can be calculated by using Equation (C.1) as follows

$$p(\mathcal{H}_\alpha|s) = \frac{p(s|\mathcal{H}_\alpha)p(\mathcal{H}_\alpha)}{p(s)}, \quad (\text{C.5})$$

$p(s)$ is calculable if all possible models are known for which $p(\mathcal{H}_\alpha|s) = 1$. But this is not the case, therefore $p(s)$ involves the sum over subset space of all considered models given as

$$p(s) = \sum_{\alpha} p(s|\mathcal{H}_\alpha)p(\mathcal{H}_\alpha). \quad (\text{C.6})$$

The normalization can be ignored by using odd ratio $\mathcal{O}_{\alpha\beta}$, use to compare two models. For any two models \mathcal{H}_α and \mathcal{H}_β , the ratio of the posterior probability distribution is regarded as the odd ratio, given by

$$\mathcal{O}_{\alpha\beta} = \frac{p(\mathcal{H}_\alpha|s)}{p(\mathcal{H}_\beta|s)} = \frac{p(\mathcal{H}_\alpha)}{p(\mathcal{H}_\beta)}\mathcal{B}_{\alpha\beta}, \quad (\text{C.7})$$

where $\mathcal{B}_{\alpha\beta}$ is the Bayes factor (or the ratio of evidence)

$$\mathcal{B}_{\alpha\beta} = \frac{p(s|\mathcal{H}_\alpha)}{p(s|\mathcal{H}_\beta)}. \quad (\text{C.8})$$

Assuming model one \mathcal{H}_0 with $s = n$ (no presence of signal in detector data) and second model \mathcal{H}_1 with $s = n+h$ (signal is present in detector data), odd ratio can be used for the comparison. Equation (C.7), which depends upon the prior

odds ratio tells us about the most preferred model over the other models. Hence, one can conclude that the prior knowledge is crucial for hypothesis testing, but this is not always true. In Bayes theorem, *Occam's razor* can introduce additional parameters which are not even there in the detector data stream and can affect the choice of the best-fit model.

Now, if the posterior distribution depends upon more than one parameter $(\lambda_1, \lambda_2, \dots)$, but we are interested in the evaluation of only one parameter λ_1 , then the posterior distribution will be

$$\begin{aligned} p(\lambda_1|s, \mathcal{H}_\alpha) &= \int d\lambda_2 \dots d\lambda_{N_p} p(\lambda_1, \dots, \lambda_{N_p}|s, \mathcal{H}_\alpha), \\ &= \int d\lambda_2 \dots d\lambda_{N_p} p(\lambda_1|\lambda_2, \dots, \lambda_{N_p}, s, \mathcal{H}_\alpha) p(\lambda_2, \dots, \lambda_{N_p}), \end{aligned} \tag{C.9}$$

where the second equality term shows the relationship between the joint and the conditional probabilities. Therefore, from Equation (C.9), a multidimensional PDF can be used to draw the posterior with a fewer number of parameters (or one parameter). The parameters which we do not need or care about are known as nuisance parameters.

Mean

The representation of the full posterior probability distribution is a tedious task. This task can be simplified by reducing the joint posteriors to a few numbers with the use of expectation value and the corresponding uncertainty in the estimated parameter. Hence, the mean is defined as

$$\begin{aligned} \mu &= E[\lambda], \\ &= \int \lambda p(\lambda|s, \mathcal{H}) d\lambda, \end{aligned} \tag{C.10}$$

the uncertainty in the measurement of parameters is known as variance and given by

$$\begin{aligned}\sigma^2 &= E [(\lambda - \mu)^2], \\ &= \int (\lambda - \mu)^2 p(\lambda|s, \mathcal{H})d\lambda.\end{aligned}\tag{C.11}$$

From the one dimensional representation of the mean and the variance given in Equations (C.10) and (C.11), one can also re-write them in multidimensional representation similarly to Equation (C.9). A higher dimensional variance-like object can be defined as follows

$$\begin{aligned}\Sigma_{ij} &\equiv E [(\lambda_i - \mu_i)(\lambda_j - \mu_j)], \\ &= \int (\lambda_i - \mu_i)(\lambda_j - \mu_j)p(\lambda_1\dots\lambda_N|s, H)d\lambda_1\dots d\lambda_N,\end{aligned}\tag{C.12}$$

where Equation (C.12) defines the covariance matrix and E denotes the expectation value of its argument. The diagonal elements of the matrix gives the variance of parameters, whereas off-diagonal terms gives the correlations between the parameters.

Confidence interval

Bayesian confidence interval (CI) provides with a better representation of the posterior and is used to measure the uncertainty on the estimated parameters. CI defines the lower and the upper limit on the parameter in the smallest limits within the posterior distribution, which contains the true value of the source parameter. A CI can be represented as

$$Prob(\lambda_{low} < \hat{\lambda} < \lambda_{high}) = \int_{\lambda_{low}}^{\lambda_{high}} p(\hat{\lambda}|s, \mathcal{H})d\lambda = CI, \quad (C.13)$$

where $\hat{\lambda}$ is an estimated parameter and CI can be either 0.68 or 0.95 or any other value.

C.2.2 Bayesian computational tools

From Equations (C.3) and (C.5), both the parameter estimation and the hypothesis testing look easy; however, the computation of posteriors for each parameter and the odd ratio can turn to be difficult. Bayesian inference for CBC signals strictly depends upon the dimensionality of the parameter space, which can be nine-dimensional in case of non-spinning components and can increase to fifteen dimensional space when spins are included—thus making these processes computationally expensive and time-consuming. Hence, more efficient statistical techniques are required.

Till now, there are two main methods used by LVC members to perform the CBC parameter estimation, implemented into algorithm library known as LALInference (LIGO Scientific Collaboration Algorithm Library Inference) [165] namely: Markov Chain Monte Carlo (MCMC) and nested sampling.

MCMC

A MCMC method is used to generate the PDF $P(x)$ from a given probability distribution $\tilde{P}(x)$ as

$$P(x) = \frac{\tilde{P}(x)}{Z}, \quad (C.14)$$

where Z is a normalization constant. Thus a set of samples $\{x^r\}$ can be generated from $\tilde{P}(x)$ using the transition from one point to another point in the parameter space. Therefore, the probability distribution on a transition from t to $t + 1$ in the parameter space is given by

$$p^{t+1}(x') = \int dx T(x', x) p^t(x), \quad (\text{C.15})$$

where $T(x', x)$ is the transition probability.

Nested sampling

In nested sampling, a set of N randomly distributed samples are calculated from the parameter space with the highest likelihood in each iteration and then taking a sum over the evidence as the number of iteration increases. Nesting sampling is used for the calculation of the evidence (Equation (C.8)), irrespective of the size and dimensionality of the parameter space, and the calculation of CBC parameters PDF at a negligible computational cost. Following Equation (C.8), one can rewrite it as follows

$$p(s|H) = \int d^{N_p} \lambda p(s|\lambda, \mathcal{H}) p(\lambda|\mathcal{H}). \quad (\text{C.16})$$

In this respect, nested sampling has the upper hand in testing hypothesis (by effectively calculating evidence integral Equation (C.16)). Besides nested sampling is also effective in calculating posterior distribution of parameters than MCMC algorithm [166].

Python based Bayesian inference library

LAL inference library helped in the GW discoveries and the parameter estimation during the various observation runs of aLIGO and AdV detectors. Since

the code in itself is decade old, hard to maintain and understand, it puts a restriction to access and to resolve the challenges regarding future upgrades. Hence, new tools are required for the purpose which are easy to learn, adapt and update with the current and future requirements in GW parameter estimation and data analysis.

For these purposes, two python-based libraries are developed (and are under continuous development). The first one is PyCBC [44], an open-source GW toolkit for the parameter estimation of CBC and GW astronomy analysis. Whereas the second one is Bilby [38, 144], a user-friendly infrastructure to perform the parameter estimation and GW data analysis. The difference between Bilby and other libraries is, its modularity, adaptability and ease to access the publicly available GW data from the GW detectors.

C.3 Fisher information matrix

Fisher information matrix (FIM) is a theoretical statistical approach to calculate the parameters of a GW signal. FIM provide with ease for the parameter estimation in comparison to other methods (in terms of computation cost). To estimate the parameters of a CBC signal, FIM calculates the first-order partial derivatives of the GW signal model with the constraint that the GW signal is in the strong-signal limit (i.e. a high-SNR signal). The variance-covariance in estimated parameters is calculated by inverting the FIM. A MCMC method explores the whole CBC parameter space with the fixed detector data, whereas FIM explores detector data for fixed CBC parameters. FIM is used extensively for the parameter estimation but have limitations while performing the task [162]. FIM has limitation over the low-SNR signals and validation of lower-order expansion investigated in [141].

Consider a model \mathcal{H} parametrized by a set of N_p number of parameters λ in a given detector data stream s , using Equation (C.3), we will have

$$p(\lambda|s, \mathcal{H}) = \frac{p(s|\lambda, \mathcal{H})p(\lambda|\mathcal{H})}{p(s|\mathcal{H})}. \quad (\text{C.17})$$

The posterior distribution $p(\lambda|s, \mathcal{H})$ contains all the information about the parameters λ . If the true values of binary source parameters λ_{true} accord with the maximum likelihood value λ_{ML} , then the likelihood function in Equation (C.17) can expand around λ_{ML} leading to the expression

$$\Gamma_{ij} = \left\langle - \frac{\partial}{\partial \lambda_i} \frac{\partial}{\partial \lambda_j} \ln p(s|\lambda, \mathcal{H}) \right\rangle \Big|_{\lambda=\lambda_{ML}}, \quad (\text{C.18})$$

where Γ_{ij} is the FIM. Equation (C.18) is a first-order partial differential equation and referred to as linearized-signal-approximation (LSA). In LSA, the posteriors expand as SNR^{-1} , thus, can be considered in a strong-signal limit (high-SNR regime). Further, FIM can be represented in terms of *Cramer-Rao bound* [162]

$$\sigma^2(\lambda_\alpha) \geq (\Gamma^{-1})_{ij}, \quad (\text{C.19})$$

which shows that the diagonal elements of the FIM set the lower bound on the variance in the parameter estimation of a GW signal.

C.4 Matched filtering

This section describes the matched filtering used in order to search for a GW signal within the observed GW data. Matched filtering is an optimal tool for the signal processing and extraction from the stationary and Gaussian noisy data

of the detector. It gives the estimated best-fit of a signal waveform weighted with the detector's noise PSD (to mark the most sensitive frequencies of a GW detector), which is then cross-correlated with the GW data at different times to generate a filtered output (i.e. to study those parts of data where a GW signal matches with the estimated best-fit signal waveform). For a GW signal generated with matched filtering, if present in the GW data, there would be a coherent contribution from the cross-correlation.

The GW detector data s contains the noise $n(t)$ with a GW signal $h(t)$ as described in Equation (1.20). Since the noise is characterized by its PSD $S_n(f)$, for convenience, it is optimal to opt for the frequency domain. Hence, the one sided PSD can be written as given in Equation (1.23) with the noise Fourier transformation given as

$$\tilde{n}(f) \equiv \int_{-\infty}^{+\infty} n(t)e^{-2\pi i f t} dt. \quad (\text{C.20})$$

For the noise spectrum, one can introduce an inner product as given by [31]

$$(g|h) \equiv \int_0^\infty \frac{\tilde{g}^*(f)\tilde{h}(f) + \tilde{g}(f)\tilde{h}^*(f)}{S_n(f)} df. \quad (\text{C.21})$$

Now, for any signal h in the detector data s , an optimal detection process can be implemented by using a matched filtering template either of the same shape as that of true GW signal or a best-fit $h_{bf} = \alpha s$, where α gives the magnitude of mismatch, as

$$\alpha \equiv (s|h_{bf}), \quad (\text{C.22})$$

and the detectability of a GW signal is given by the SNR of the optimal detection, hence

$$SNR = \frac{(h|h_{bf})}{\sqrt{\langle (h_{bf}|n)(n|h_{bf}) \rangle}} \Big|_{h_{bf}=\alpha s} = (h|h)^{1/2}. \quad (\text{C.23})$$

Equation (C.23) gives the SNR and does not depend on the normalization of h_{bf} , and holds true if there is no mismatch between the signal and the estimated template waveform. But if there is a mismatch between the shape of a true GW signal and the estimated template waveform, the SNR will be reduced to

$$SNR = (h|h)^{1/2} \mathcal{X}, \quad (\text{C.24})$$

where $\mathcal{X} < 1$, is the mismatch between the two signal waveforms represented as

$$\mathcal{X} \equiv \frac{(h|h_{bf})}{\sqrt{(h|h)(h_{bf}|h_{bf})}} \equiv (h^{norm}|h_{bf}^{norm}), \quad (\text{C.25})$$

h^{norm} and h_{bf}^{norm} are the normalized signal waveforms. The match between these two waveforms can be maximized over time t and phase shift $\phi(t)$; hence, the matching is [72]

$$X(h, h_{bf}) = \max_{t, \phi(t)} (h^{norm}|h_{bf}^{norm}). \quad (\text{C.26})$$

Therefore, the mismatch due to the modeling errors can be re-written as

$$\mathcal{X}(h, h_{bf}) = 1 - X(h, h_{bf}). \quad (\text{C.27})$$

C.5 Cross-correlations

The SCGWB is weak and does not have deterministic waveform, so it is nearly impossible to distinguish between the detector noise and a true SCGWB in a single GW detector data. For this purpose, a correlation method is used between a pair of GW detectors with different noise realization. The correlation method (or cross-correlation) between two detectors is performed by using the output of one detector as a template for the second detector including the distance between two detectors and their orientation with respect to each other.

Here, I will discuss the cross-correlation method in reference to Bayesian inference. The key idea behind cross-correlating the output of a detector pair or multi-detector pair is to identify the SCGWB in the detector noise. An SCGWB would be same in the correlated data between detector pairs whereas detector noise is not. To understand this concept of cross-correlation and how it works between detector pairs, consider two coaligned and coincident detectors with output s_1 and s_2 , respectively

$$s_i = h_i + n_i, \tag{C.28}$$

where s_i denotes the overall detector output, h_i is the GW signal and n_i is the instrumental noise with index i running over total number of detectors. To search for an SCGWB with just one detector is impossible as one would not be able to distinguish between the detector noise and the SCGWB. Therefore,

$$\begin{aligned} s_1 &= h_1 + n_1, \\ s_2 &= h_2 + n_2. \end{aligned} \tag{C.29}$$

If both detectors are coaligned and coincident, then GW strains are $h = h_1 = h_2$. In contrast, noise would not be equal to each other. Hence the output of one detector works as a template for the second detector and vice-versa. Now, for the cross-correlation, we will take a product of these two outputs $\hat{C}_{12} = s_1 s_2$. Hence, we will have

$$\langle \hat{C}_{12} \rangle = \langle s_1 s_2 \rangle = \langle h^2 \rangle + \langle n_1 n_2 \rangle + \cancel{\langle h n_2 \rangle} + \cancel{\langle n_1 h \rangle} = \langle h^2 \rangle + \langle n_1 n_2 \rangle. \quad (\text{C.30})$$

Further, the instrumental noise of different detectors would be uncorrelated and leads to $\langle n_1 n_2 \rangle = 0$. Hence we will have

$$\langle \hat{C}_{12} \rangle = \langle h^2 \rangle \equiv S_h. \quad (\text{C.31})$$

The expectation value of the cross-correlation between a detector pair gives the variance of an SCGWB. If the detector noise $n(t)$ follows the Gaussian distribution, then the probability distribution of noise is given as [143]

$$p(n) = \frac{1}{2\pi\sqrt{\sigma}} \exp\left[-\frac{n^2}{2\sigma^2}\right], \quad (\text{C.32})$$

where σ is the standard deviation corresponds to detector noise. Hence, we can write the likelihood function $p(s|S_n, \mathcal{H})$ for a detector with output s , noise PSD S_n and for a given model \mathcal{H} as follows

$$p(s|S_n, \mathcal{H}) \propto \exp\left[-\frac{s^2}{2S_n}\right], \quad (\text{C.33})$$

which we can expand for a detector pair with two choices of models, i.e. when we have only noise ($h = 0$), \mathcal{H}_N as

$$p(s|S_{n_1}, S_{n_2}, \mathcal{H}_N) \propto \exp \left[-\frac{1}{2} \left(\frac{s_1^2}{S_{n_1}} + \frac{s_2^2}{S_{n_2}} \right) \right], \quad (\text{C.34})$$

and when a signal \mathcal{H}_S is also present in the data

$$p(s|S_{n_1}, S_{n_2}, h, \mathcal{H}_S) \propto \exp \left[-\frac{1}{2} \left(\frac{(s_1 - h)^2}{S_{n_1}} + \frac{(s_2 - h)^2}{S_{n_2}} \right) \right], \quad (\text{C.35})$$

with the GW signal probability distribution

$$p(h|S_h, \mathcal{H}_S) \propto \exp \left[-\frac{1}{2} \frac{h^2}{S_h} \right]. \quad (\text{C.36})$$

The cross-correlation method is useful when two or more detectors detect the common GW signal. The SCGWB in itself is an additional noise source in a single detector. As mentioned in Equation (C.30), when the data from two or more detectors is multiplied the common GW signal in all of these detectors adds up coherently. The only drawback of cross-correlation method is that it is of no use with a single detector.

To handle this issue with a single detector, one can construct the estimated noise variance from the detector output and excess power as

$$S_h = \frac{1}{N} \sum_{i=1}^N s_i^2 - S_n, \quad (\text{C.37})$$

where N is the total number of data samples for a single detector; however, this approach is also not suitable as GW detectors are not screened to GWs. The formation of a null channel can help to overcome this challenge as discussed in [136].

C.6 Optimal filter

To resolve and extract information about CBC with future third-generation GW detectors with a large number of merger signals, it would be a difficult task as the uncertainty of overlap between different binary signals will also increase. When the statistical properties and the source of noise in the detector are known, then the exact form of the signal by using a theoretical model can be predicted. Therefore, it is possible to use optimal match filtering, which expresses the probability that detector data contains a GW signal.

Optimal filtering increases the detection probability, maximize the SNR and minimize the variance. For a GW detector with the output as given in Equation (1.20). Thus the cross-correlation signal S_{12} between the two GW detector outputs s_1 and s_2 is an integration over observation time T [35] given by

$$S_{12} = \int_{-T/2}^{+T/2} dt \int_{-T/2}^{+T/2} dt' s_1(t) s_2(t') Q(t, t'), \quad (\text{C.38})$$

where $Q(t, t')$ is optimal filter function depends upon time difference $\Delta t = t - t'$. Therefore, one can find an optimal filter for any time difference such that $Q(t - t') = Q(t, t')$.

Optimal filter function $Q(t - t')$ depends upon ORF (see Appendix B), i.e. location and orientation of detectors with respect to each other, on the noise PSD of the detectors and energy spectrum density of SGWB. When time delay factor $\Delta t = t - t'$ is larger in comparison to the travel time of light d/c between two detector sites, the optimal filter rapidly falls to zero.

During SGWB searches, we assume that amplitude of an SGWB is extremely below the detector sensitivity level. Since the observation time is $T \gg d/c$, from Equation (C.38) we will have

$$S_{12} \equiv \int_{-T/2}^{+T/2} dt \int_{-\infty}^{+\infty} dt' s_1(t)s_2(t')Q(t-t'), \quad (\text{C.39})$$

and the Fourier transformation is

$$S_{12} = \int_{-\infty}^{+\infty} df \int_{-\infty}^{+\infty} df' \delta_T(f-f') \tilde{s}_1^*(f) \tilde{s}_2(f') \tilde{Q}(f'), \quad (\text{C.40})$$

where terms with \sim represent the Fourier transform of the corresponding terms in Equation (C.39) and $\delta_T(f-f')$ is time limited Dirac-delta function of $\delta(f-f')$. For optimal filter $Q(t)$ to be a real quantity, it must satisfy the condition $\tilde{Q}(-f) = \tilde{Q}^*(f)$. The purpose of using an optimal filter is to maximize the quantity in Equation (C.40), thus it's evident to maximize SNR like

$$SNR = \frac{\mu}{\sigma}, \quad (\text{C.41})$$

where $\mu = \langle S_{12} \rangle$ and $\sigma = \sqrt{\langle S_{12}^2 \rangle - \langle S_{12} \rangle^2}$ are the mean and variance of the cross-correlating signal S_{12} . Using Equation (C.40), (C.29), (B.8) and (C.31) one can calculate μ and σ as

$$\mu = \frac{T}{2} \int_{-\infty}^{+\infty} df S_h(f) \gamma(f) \tilde{Q}(f), \quad (\text{C.42})$$

where S_h is expectation value of cross-correlation between detectors output (see Equation (C.31)) and the variance is

$$\sigma^2 = \frac{T}{4} \int_{-\infty}^{+\infty} df S_{n_1}(f) S_{n_2}(f) |\tilde{Q}(f)|^2. \quad (\text{C.43})$$

To maximize the SNR (Equation (C.41)), from Equations (C.42) and (C.43) with inner product from Equation (3.3), we will have

$$\begin{aligned}\mu &= \frac{T}{2} \left(\tilde{Q}, \frac{S_h \gamma(f)}{S_{n_1}(f) S_{n_2}(f)} \right), \\ \sigma^2 &= \frac{T}{4} \left(\tilde{Q}, \tilde{Q} \right).\end{aligned}\tag{C.44}$$

Therefore from Equations (C.41) and (C.44), we have the maximized SNR

$$SNR^2 = \frac{\mu^2}{\sigma^2} \approx T \left[\frac{\tilde{Q}, \frac{\gamma(f) S_h(f)}{S_{n_1} S_{n_2}}}{\tilde{Q}, \tilde{Q}} \right].\tag{C.45}$$

with an optimal filter defined as

$$\tilde{Q}(f) = \mathcal{C} \frac{\gamma(f) S_h(f)}{S_{n_1}(f) S_{n_2}(f)},\tag{C.46}$$

where \mathcal{C} is a real-valued overall normalization constant. The optimal filter in Equation (C.46) depends upon the energy spectrum of the SGWB. For an SGWB, $S_h = S_{GW}$ (see Equation (3.35)) depends upon Ω_{GW} , which is a frequency-dependent quantity, for a given detector operating in a particular frequency band, we can construct a set of optimal filters for different values of frequency by using the following relation

$$\Omega_{GW}(f) = \Omega_\alpha f^\alpha.\tag{C.47}$$

After following this process, one can analyze the output of two GW detectors for each optimal filter. Equation (C.47) is an approximation used while searching for SGWB.

C.7 Overlap reduction function

This subsection discusses the frequency-dependent quantity referred as the overlap reduction function (ORF) [82, 63, 35, 123], a set of geometrical factors associated with the structural geometry and the location of a GW detector pair [81]. To search for an SGWB in the detector data, it is crucial to understand the geometry of a GW detector pair such as non-parallel alignment of detector arms, their shape and time delay between them. But in reality, two GW detectors are not coaligned and coincident. The distance between two GW detectors causes the arrival time difference of a GW signal in the detector. In contrast, the non-parallel alignment of the detectors arm (for e.g. the case of CE and ET detectors) reduces the overall sensitivity of a GW detector pair.

In particular, ET and CE would be different in terms of their geometry. The ORF $\gamma(f)$, a dimensionless quantity, for a detector pair is given as (from Equations (B.8), (C.29) and (C.31))

$$\gamma(f) = \frac{5}{8\pi} \sum_A \int_{S^2} d\hat{\Omega} e^{2\pi i f \hat{\Omega} \cdot \Delta \vec{x} / c} F_1^A(\hat{\Omega}) F_2^A(\hat{\Omega}), \quad (\text{C.48})$$

where $5/(8\pi)$ is the overall normalization factor, and is chosen such that $\gamma(f) = 1$ for a coaligned and coincident detector pair with perpendicular arms. Even for the GW detectors with non-perpendicular arms like ET, it is convenient to adopt the same normalization factor. Summation over A represent the sum over all polarization modes $A = +, \times$, $\hat{\Omega}$ is the unit vector specifying direction on two-sphere whereas integration over S^2 is an isotropic average over all possible directions of incoming GW signal. The exponential term represents the phase shift and depends on the relative position vector $\Delta \vec{x}$ between two detector sites. With the phase shift, detectors become more sensitive to detect different mode of polarizations [136], [137] and non-GR modes. We would be able to observe these

polarizations with ET detector as it is sensitive to different modes of polarization due to its triangular shape. At last $F_i^A(\hat{\Omega})$, ($i = 1, 2$) is the antenna response function [123] of the i th detector to polarization A (see Equation (B.7)).

Since both ET and CE are different in their geometry, shape and size, we would like to understand how antenna response and ORF would be calculated. Figure 3.11 presents the ORF between the CE and ET detector pair with different ET sub-detector. As mentioned in [82], the detector's orientation with respect to each other also affect the sensitivity of the detector pair towards the polarization modes, SNR value and then towards the SGWB searches (for more details see [88]).

Bibliography

- [1] <https://dcc.ligo.org/t2000384>.
- [2] <https://git.ligo.org/gwinc>.
- [3] <https://git.ligo.org/stochastic-public/stochastic>.
- [4] Matlab, 9.8.0.1323502 (r2020a) (the mathworks 1177 inc., natick, massachusetts, 2020).
- [5] <https://cosmicexplorer.org/researchers.html>, October 2020.
- [6] <https://gracedb.ligo.org/superevents/public/o3/>, October 2020.
- [7] <https://www.ligo.org/science/gw-stochastic.php>, October 2020.
- [8] B. P. Abbott et al. An upper limit on the stochastic gravitational-wave background of cosmological origin. *Nature*, 460(7258):990–994, 2009.
- [9] B. P. Abbott et al. GW150914: Implications for the stochastic gravitational-wave background from binary black holes. *Phys. Rev. Lett.*, 116:131102, Mar 2016.
- [10] B. P. Abbott et al. Observation of gravitational waves from a binary black hole merger. *Phys. Rev. Lett.*, 116:061102, Feb 2016.

- [11] B. P. Abbott et al. Effects of waveform model systematics on the interpretation of GW150914. *Classical and Quantum Gravity*, 34(10):104002, Apr 2017.
- [12] B. P. Abbott et al. Exploring the sensitivity of next generation gravitational wave detectors. *Classical and Quantum Gravity*, 34(4):044001, 01 2017.
- [13] B. P. Abbott et al. GW170817: Observation of gravitational waves from a binary neutron star inspiral. *Phys. Rev. Lett.*, 119:161101, Oct 2017.
- [14] B. P. Abbott et al. Multi-messenger observations of a binary neutron star merger. *The Astrophysical Journal*, 848(2):L12, oct 2017.
- [15] B. P. Abbott et al. Upper limits on the stochastic gravitational-wave background from advanced LIGO’s first observing run. *Phys. Rev. Lett.*, 118:121101, Mar 2017.
- [16] B. P. Abbott et al. Constraints on cosmic strings using data from the first advanced LIGO observing run. *Phys. Rev. D*, 97:102002, May 2018.
- [17] B. P. Abbott et al. GW170817: Implications for the stochastic gravitational-wave background from compact binary coalescences. *Phys. Rev. Lett.*, 120:091101, Feb 2018.
- [18] B. P. Abbott et al. Binary black hole population properties inferred from the first and second observing runs of advanced LIGO and advanced Virgo. *The Astrophysical Journal*, 882(2):L24, Sep 2019.
- [19] B. P. Abbott et al. GWTC-1: A gravitational-wave transient catalog of compact binary mergers observed by LIGO and Virgo during the first and second observing runs. *Physical Review X*, 9(3), Sep 2019.
- [20] B. P. Abbott et al. Search for the isotropic stochastic background using data from advanced LIGO’s second observing run. *Phys. Rev. D*, 100:061101, Sep 2019.

- [21] B. P. Abbott et al. GW190425: Observation of a compact binary coalescence with total mass $3.4 M_{\odot}$. *The Astrophysical Journal*, 892(1):L3, mar 2020.
- [22] R. Abbott et al. GW190412: Observation of a binary-black-hole coalescence with asymmetric masses. *Phys. Rev. D*, 102:043015, Aug 2020.
- [23] R. Abbott et al. GW190521: A binary black hole merger with a total mass of $150 M_{\odot}$. *Phys. Rev. Lett.*, 125:101102, Sep 2020.
- [24] R. Abbott et al. GW190814: Gravitational waves from the coalescence of a 23 solar mass black hole with a 2.6 solar mass compact object. *The Astrophysical Journal*, 896(2):L44, jun 2020.
- [25] R. Abbott et al. GWTC-2: Compact Binary Coalescences Observed by LIGO and Virgo During the First Half of the Third Observing Run. 10 2020.
- [26] R. Abbott et al. Upper limits on the isotropic gravitational-wave background from advanced LIGO's and advanced Virgo's third observing run, Jan 2021. arXiv:2101.12130.
- [27] T. Accadia et al. Virgo: a laser interferometer to detect gravitational waves. *Journal of Instrumentation*, 7(3):3012, March 2012.
- [28] F. Acernese et al. Advanced Virgo: a second-generation interferometric gravitational wave detector. *Classical and Quantum Gravity*, 32(2):024001, dec 2014.
- [29] P. A. R. Ade, Z. Ahmed, R. W. Aikin, et al. Constraints on Primordial Gravitational Waves Using Planck, WMAP, and New BICEP2/Keck Observations through the 2015 Season. *Phys. Rev. Lett.*, 121:221301, Nov 2018.

- [30] P. A. R. Ade et al. Planck 2015 results XIII. cosmological parameters. *Astronomy and Astrophysics*, 594(A13), sep 2016.
- [31] P. Ajith et al. Template bank for gravitational waveforms from coalescing binary black holes: Nonspinning binaries. *Phys. Rev. D*, 77:104017, May 2008.
- [32] P. Ajith, M. Hannam, S. Husa, et al. Inspiral-merger-ringdown waveforms for black-hole binaries with nonprecessing spins. *Phys. Rev. Lett.*, 106:241101, Jun 2011.
- [33] T. Akutsu et al. Overview of KAGRA: Detector design and construction history, 2020. arXiv:2005.05574.
- [34] B. Allen. Spherical ansatz for parameter-space metrics. *Phys. Rev. D*, 100:124004, Dec 2019.
- [35] B. Allen and J. D. Romano. Detecting a stochastic background of gravitational radiation: Signal processing strategies and sensitivities. *Phys. Rev. D*, 59:102001, Mar 1999.
- [36] Z. Arzoumanian et al. The NANOGrav 12.5-year data set: Search for an isotropic stochastic gravitational-wave background, 2020. arVix:2009.04496.
- [37] J. Asai et al. Advanced LIGO. *Classical and Quantum Gravity*, 32(7):074001, 03 2015.
- [38] G. Ashton, M. Hübner, et al. Bilby: A user-friendly bayesian inference library for gravitational-wave astronomy. *The Astrophysical Journal Supplement Series*, 241(2):27, Apr 2019.
- [39] R. Balasubramanian, B. S. Sathyaprakash, and S. V. Dhurandhar. Gravitational waves from coalescing binaries: Detection strategies and monte carlo estimation of parameters. *Phys. Rev. D*, 53:3033–3055, Mar 1996.

- [40] S. W. Ballmer. A radiometer for stochastic gravitational waves. *Classical and Quantum Gravity*, 23(8):S179–S185, mar 2006.
- [41] N. Bartolo et al. Science with the space-based interferometer LISA. IV: probing inflation with gravitational waves. *Journal of Cosmology and Astroparticle Physics*, 2016(12):026–026, dec 2016.
- [42] K. Belczynski, K. Vassiliki, and T. Bulik. A Comprehensive Study of Binary Compact Objects as Gravitational Wave Sources: Evolutionary Channels, Rates, and Physical Properties. *The Astrophysical Journal*, 572(1):407–431, jun 2002.
- [43] P. Binétruy, A. Bohé, C. Caprini, and J. F. Dufaux. Cosmological backgrounds of gravitational waves and eLISA/NGO: phase transitions, cosmic strings and other sources. *Journal of Cosmology and Astroparticle Physics*, 2012(06):027–027, jun 2012.
- [44] C. M. Biwer, C. D. Capano, et al. PyCBC inference: A python-based parameter estimation toolkit for compact binary coalescence signals. *Publications of the Astronomical Society of the Pacific*, 131(996):024503, Jan 2019.
- [45] J. J. Blanco-Pillado, K. D. Olum, and B. Shlaer. Number of cosmic string loops. *Phys. Rev. D*, 89:023512, Jan 2014.
- [46] A. Bohé et al. Improved effective-one-body model of spinning, nonprecessing binary black holes for the era of gravitational-wave astrophysics with advanced detectors. *Phys. Rev. D*, 95:044028, Feb 2017.
- [47] L. Bosi and E. K. Porter. Data analysis challenges for the Einstein Telescope. *General Relativity and Gravitation*, 43(2):519–535, Feb 2010.

- [48] A. Buonanno and Y. Chen. Quantum noise in second generation, signal-recycled laser interferometric gravitational-wave detectors. *Phys. Rev. D*, 64:042006, Jul 2001.
- [49] A. Buonanno, Y. Pan, J. G. Baker, et al. Approaching faithful templates for nonspinning binary black holes using the effective-one-body approach. *Phys. Rev. D*, 76:104049, Nov 2007.
- [50] A. Buonanno, Y. Pan, H. P. Pfeiffer, et al. Effective-one-body waveforms calibrated to numerical relativity simulations: Coalescence of nonspinning, equal-mass black holes. *Phys. Rev. D*, 79:124028, Jun 2009.
- [51] C. T. Byrnes et al. Primordial black holes with an accurate QCD equation of state. *Journal of Cosmology and Astroparticle Physics*, 2018(08):041, aug 2018.
- [52] C. Caprini and R. Durrer. Gravitational waves from stochastic relativistic sources: Primordial turbulence and magnetic fields. *Phys. Rev. D*, 74:063521, Sep 2006.
- [53] C. Caprini, R. Durrer, T. Konstandin, and G. Servant. General properties of the gravitational wave spectrum from phase transitions. *Phys. Rev. D*, 79:083519, Apr 2009.
- [54] C. Caprini, R. Durrer, and G. Servant. Gravitational wave generation from bubble collisions in first-order phase transitions: An analytic approach. *Phys. Rev. D*, 77:124015, Jun 2008.
- [55] C. Caprini et al. Science with the space-based interferometer eLISA. II: gravitational waves from cosmological phase transitions. *Journal of Cosmology and Astroparticle Physics*, 2016(04):001–001, apr 2016.
- [56] C. Caprini and D. G. Figueroa. Cosmological backgrounds of gravitational waves. *Classical and Quantum Gravity*, 35(16):163001, jul 2018.

- [57] B. Carr, K. Kohri, et al. Constraints on primordial black holes, 2020. arXiv:2002.12778.
- [58] B. Carr and F. Kühnel. Primordial black holes as dark matter: Recent developments. *Annual Review of Nuclear and Particle Science*, 70(1), Aug 2020.
- [59] G. Cella. Off-Line Subtraction of Seismic Newtonian Noise. In B. Casciari, D. Fortunato, M. Francaviglia, and A. Masiello, editors, *Recent Developments in General Relativity*, pages 495–503. Springer Milan, 2000.
- [60] K. Chakravarti, A. Gupta, S. Bose, et al. Systematic effects from black hole-neutron star waveform model uncertainties on the neutron star equation of state. *Phys. Rev. D*, 99:024049, Jan 2019.
- [61] K. Chamberlain and N. Yunes. Theoretical physics implications of gravitational wave observation with future detectors. *Phys. Rev. D*, 96:084039, Oct 2017.
- [62] Z. Chen, E. A. Huerta, et al. Observation of eccentric binary black hole mergers with second and third generation gravitational wave detector networks, 2020.
- [63] N. Christensen. Measuring the stochastic gravitational-radiation background with laser-interferometric antennas. *Phys. Rev. D*, 46:5250–5266, Dec 1992.
- [64] N. Christensen. Stochastic gravitational wave backgrounds. *Reports on Progress in Physics*, 82(1):016903, Nov 2018.
- [65] A. J. K. Chua, N. Korsakova, et al. Gaussian processes for the interpolation and marginalization of waveform error in extreme-mass-ratio-inspiral parameter estimation. *Phys. Rev. D*, 101:044027, Feb 2020.

- [66] S. Clesse, J. García-Bellido, and S. Orani. Detecting the stochastic gravitational wave background from primordial black hole formation, 2018. arXiv:1812.11011.
- [67] R. Cotesta, A. Buonanno, A. Bohé, et al. Enriching the symphony of gravitational waves from binary black holes by tuning higher harmonics. *Phys. Rev. D*, 98:084028, Oct 2018.
- [68] M. W. Coughlin, N. L. Christensen, R. De Rosa, et al. Subtraction of correlated noise in global networks of gravitational-wave interferometers. *Classical and Quantum Gravity*, 33(22):224003, oct 2016.
- [69] M. W. Coughlin, A. Cirone, P. Meyers, et al. Measurement and subtraction of schumann resonances at gravitational-wave interferometers. *Phys. Rev. D*, 97:102007, May 2018.
- [70] J. Crowder and N. J. Cornish. Beyond LISA: Exploring future gravitational wave missions. *Phys. Rev. D*, 72(8):083005, Oct 2005.
- [71] Y. Cui, M. Lewicki, et al. Probing the pre-BBN universe with gravitational waves from cosmic strings. *Journal of High Energy Physics*, 2019(1), Jan 2019.
- [72] C. Cutler and E. E. Flanagan. Gravitational waves from merging compact binaries: How accurately can one extract the binary’s parameters from the inspiral waveform? *Phys. Rev. D*, 49:2658–2697, Mar 1994.
- [73] C. Cutler and J. Harms. Big bang observer and the neutron-star-binary subtraction problem. *Phys. Rev. D*, 73:042001, Feb 2006.
- [74] C. Cutler and M. Vallisneri. Lisa detections of massive black hole inspirals: Parameter extraction errors due to inaccurate template waveforms. *Phys. Rev. D*, 76:104018, Nov 2007.

- [75] T. Damour and A. Vilenkin. Gravitational radiation from cosmic (super)strings: Bursts, stochastic background, and observational windows. *Phys. Rev. D*, 71:063510, Mar 2005.
- [76] K. Danzmann et al. LISA mission proposal. 2017. arXiv:1702.00786.
- [77] P. S. Bhupal Dev, F. Ferrer, et al. Gravitational waves from first-order phase transition in a simple axion-like particle model. *Journal of Cosmology and Astroparticle Physics*, 2019(11):006–006, nov 2019.
- [78] J. C. Driggers, J. Harms, and R. X. Adhikari. Subtraction of newtonian noise using optimized sensor arrays. *Phys. Rev. D*, 86:102001, Nov 2012.
- [79] S. Dwyer et al. Gravitational wave detector with cosmological reach. *Phys. Rev. D*, 91:082001, Apr 2015.
- [80] R. Easther, J. T. Giblin, and E. A. Lim. Gravitational wave production at the end of inflation. *Phys. Rev. Lett.*, 99:221301, Nov 2007.
- [81] L. S. Finn, S. L. Larson, and J. D. Romano. Detecting a stochastic gravitational-wave background: The overlap reduction function. *Phys. Rev. D*, 79:062003, Mar 2009.
- [82] E. E. Flanagan. Sensitivity of the laser interferometer gravitational wave observatory to a stochastic background, and its dependence on the detector orientations. *Phys. Rev. D*, 48:2389–2407, Sep 1993.
- [83] B. Gadre, S. Mitra, and S. Dhurandhar. Hierarchical search strategy for the efficient detection of gravitational waves from nonprecessing coalescing compact binaries with aligned-spins. *Phys. Rev. D*, 99:124035, Jun 2019.
- [84] Y. Gouttenoire, G. Servant, and P. Simakachorn. Beyond the standard models with cosmic strings. *Journal of Cosmology and Astroparticle Physics*, 2020(07):032–032, jul 2020.

- [85] A. M. Green and B. J. Kavanagh. Primordial black holes as a dark matter candidate, 2020. arXiv:2007.10722.
- [86] A. H. Guth. Inflationary universe: A possible solution to the horizon and flatness problems. *Phys. Rev. D*, 23:347–356, Jan 1981.
- [87] M. C. Guzzetti, N. Bartolo, M. Liguori, and S. Matarrese. Gravitational waves from inflation, 2016. arXiv:1605.01615.
- [88] E. D. Hall and M. Evans. Metrics for next-generation gravitational-wave detectors. *Classical and Quantum Gravity*, 36(22):225002, oct 2019.
- [89] M. Hannam, P. Schmidt, et al. Simple model of complete precessing black-hole-binary gravitational waveforms. *Phys. Rev. Lett.*, 113:151101, Oct 2014.
- [90] J. Harms et al. Low-frequency terrestrial gravitational-wave detectors. *Phys. Rev. D*, 88:122003, Dec 2013.
- [91] J. Harms, C. Mahrtdt, et al. Subtraction-noise projection in gravitational-wave detector networks. *Phys. Rev. D*, 77:123010, Jun 2008.
- [92] S. Hild, S. Chelkowski, and A. Freise. Pushing towards the ET sensitivity using 'conventional' technology, 2008. arXiv:0810.0604.
- [93] S. Hild et al. A xylophone configuration for a third-generation gravitational wave detector. *Classical and Quantum Gravity*, 27(1):015003, dec 2009.
- [94] S. Hild et al. Sensitivity studies for third-generation gravitational wave observatories. *Classical and Quantum Gravity*, 28(9):094013, apr 2011.
- [95] I. Hinder, S. Ossokine, H. P. Pfeiffer, and A. Buonanno. Gravitational waveforms for high spin and high mass-ratio binary black holes: A synergistic use of numerical-relativity codes. *Phys. Rev. D*, 99:061501, Mar 2019.

- [96] M. Hindmarsh, S. J. Huber, et al. Gravitational waves from the sound of a first order phase transition. *Phys. Rev. Lett.*, 112:041301, Jan 2014.
- [97] M. Hindmarsh, S. J. Huber, et al. Numerical simulations of acoustically generated gravitational waves at a first order phase transition. *Phys. Rev. D*, 92:123009, Dec 2015.
- [98] Y. Huang, C. Haster, et al. Statistical and systematic uncertainties in extracting the source properties of neutron star - black hole binaries with gravitational waves, 2020. arXiv:2005.11850.
- [99] S. J. Huber and T. Konstandin. Gravitational wave production by collisions: more bubbles. *Journal of Cosmology and Astroparticle Physics*, 2008(09):022, sep 2008.
- [100] S. Husa et al. Frequency-domain gravitational waves from nonprecessing black-hole binaries. I. new numerical waveforms and anatomy of the signal. *Phys. Rev. D*, 93:044006, Feb 2016.
- [101] M. G. Jackson, N. T. Jones, and J. Polchinski. Collisions of cosmic F- and D-strings. *Journal of High Energy Physics*, 2005(10):013–013, oct 2005.
- [102] T. Kahniashvili, A. Kosowsky, G. Gogoberidze, and Y. Maravin. Detectability of gravitational waves from phase transitions. *Phys. Rev. D*, 78:043003, Aug 2008.
- [103] M. Kamionkowski, A. Kosowsky, and M. S. Turner. Gravitational radiation from first-order phase transitions. *Phys. Rev. D*, 49:2837–2851, Mar 1994.
- [104] S. Kawamura et al. The japanese space gravitational wave antenna—DECIGO. *Classical and Quantum Gravity*, 23(8):S125–S131, 03 2006.

- [105] S. Khan et al. Frequency-domain gravitational waves from nonprecessing black-hole binaries. II. a phenomenological model for the advanced detector era. *Phys. Rev. D*, 93:044007, Feb 2016.
- [106] K. Kohri and T. Terada. Possible solar-mass primordial black holes for NANOGrav hint of gravitational waves, 2020. arXiv:2009.11853.
- [107] A. Kosowsky and M. S. Turner. Gravitational radiation from colliding vacuum bubbles: Envelope approximation to many-bubble collisions. *Phys. Rev. D*, 47:4372–4391, May 1993.
- [108] A. Kosowsky, M. S. Turner, and R. Watkins. Gravitational radiation from colliding vacuum bubbles. *Phys. Rev. D*, 45:4514–4535, Jun 1992.
- [109] A. Kosowsky, M. S. Turner, and R. Watkins. Gravitational waves from first-order cosmological phase transitions. *Phys. Rev. Lett.*, 69:2026–2029, Oct 1992.
- [110] P. Kumar, T. Chu, et al. Accuracy of binary black hole waveform models for aligned-spin binaries. *Phys. Rev. D*, 93:104050, May 2016.
- [111] P. D. Lasky, Chiara M. F. Mingarelli, et al. Gravitational-wave cosmology across 29 decades in frequency. *Phys. Rev. X*, 6:011035, Mar 2016.
- [112] A. D. Linde. A new inflationary universe scenario: A possible solution of the horizon, flatness, homogeneity, isotropy and primordial monopole problems. *Phys. Lett. B*, 108(6):389–393, feb 1982.
- [113] T. B. Littenberg, J. G. Baker, et al. Systematic biases in parameter estimation of binary black-hole mergers. *Phys. Rev. D*, 87:104003, May 2013.
- [114] J. Lizarraga, J. Urrestilla, et al. New CMB constraints for abelian higgs cosmic strings. *Journal of Cosmology and Astroparticle Physics*, 2016(10):042–042, oct 2016.

- [115] L. Lorenz, C. Ringeval, and M. Sakellariadou. Cosmic string loop distribution on all length scales and at any redshift. *Journal of Cosmology and Astroparticle Physics*, 2010(10):003–003, Oct 2010.
- [116] J. Luo et al. TianQin: a space-borne gravitational wave detector. *Classical and Quantum Gravity*, 33(3):035010, jan 2016.
- [117] Z. Luo, Z. Guo, et al. A brief analysis to Taiji: Science and technology. *Results in Physics*, 16:102918, 2020.
- [118] M. Maggiore et al. Science case for the Einstein Telescope. *Journal of Cosmology and Astroparticle Physics*, 2020(03):050–050, mar 2020.
- [119] V. Mandic, S. Bird, and I. Cholis. Stochastic gravitational-wave background due to primordial binary black hole mergers. *Physical Review Letters*, 117(20), Nov 2016.
- [120] P. Daniel Meerburg, Renée Hložek, Boryana Hadzhiyska, and Joel Meyers. Multiwavelength constraints on the inflationary consistency relation. *Phys. Rev. D*, 91:103505, May 2015.
- [121] C. M. F. Mingarelli, S. R. Taylor, B. S. Sathyaprakash, and W. M. Farr. Understanding $\Omega_{gw}(f)$ in gravitational wave experiments, 2019. arXiv:1911.09745.
- [122] S. Mukherjee, P. K. Aluri, et al. Direction dependence of cosmological parameters due to cosmic hemispherical asymmetry. *Journal of Cosmology and Astroparticle Physics*, 2016(06):042–042, jun 2016.
- [123] A. Nishizawa et al. Probing nontensorial polarizations of stochastic gravitational-wave backgrounds with ground-based laser interferometers. *Phys. Rev. D*, 79:082002, Apr 2009.
- [124] The Next-Generation Global Gravitational-Wave Observatory. <https://gwic.ligo.org/3gsubcomm/documents/science-case.pdf>, 2019.

- [125] S. Ölmez, V. Mandic, and X. Siemens. Gravitational-wave stochastic background from kinks and cusps on cosmic strings. *Phys. Rev. D*, 81:104028, May 2010.
- [126] B. J. Owen. Search templates for gravitational waves from inspiraling binaries: Choice of template spacing. *Phys. Rev. D*, 53:6749–6761, Jun 1996.
- [127] Y. Pan, A. Buonanno, M. Boyle, et al. Inspiral-merger-ringdown multipolar waveforms of nonspinning black-hole binaries using the effective-one-body formalism. *Phys. Rev. D*, 84:124052, Dec 2011.
- [128] Y. Pan, A. Buonanno, A. Taracchini, et al. Inspiral-merger-ringdown waveforms of spinning, precessing black-hole binaries in the effective-one-body formalism. *Phys. Rev. D*, 89:084006, Apr 2014.
- [129] E. S. Phinney. A Practical theorem on gravitational wave backgrounds. 7 2001.
- [130] Planck Collaboration and P. A. R. Ade et al. Planck 2013 results XXV. searches for cosmic strings and other topological defects. *A&A*, 571:A25, 2014.
- [131] M. Punturo et al. The Einstein Telescope: a third-generation gravitational wave observatory. *Classical and Quantum Gravity*, 27(19):194002, 09 2010.
- [132] M. Pürrer, M. Hannam, P. Ajith, and S. Husa. Testing the validity of the single-spin approximation in inspiral-merger-ringdown waveforms. *Phys. Rev. D*, 88:064007, Sep 2013.
- [133] M. Pürrer and C. Haster. Gravitational waveform accuracy requirements for future ground-based detectors. *Phys. Rev. Research*, 2:023151, May 2020.

- [134] M. Raidal, V. Vaskonen, and H. Veermäe. Gravitational waves from primordial black hole mergers. *Journal of Cosmology and Astroparticle Physics*, 2017(09):037–037, Sep 2017.
- [135] T. Regimbau. The astrophysical gravitational wave stochastic background. *Research in Astronomy and Astrophysics*, 11(4):369–390, mar 2011.
- [136] T. Regimbau et al. Mock data challenge for the Einstein Gravitational-Wave Telescope. *Phys. Rev. D*, 86(12):122001, Dec 2012.
- [137] T. Regimbau, M. Evans, et al. Digging deeper: Observing primordial gravitational waves below the binary-black-hole-produced stochastic background. *Phys. Rev. Lett.*, 118(15):151105, Apr 2017.
- [138] D. Reitze et al. Cosmic Explorer: The U.S. contribution to gravitational-wave astronomy beyond LIGO, 2019. arXiv:1907.04833.
- [139] C. Ringeval, M. Sakellariadou, and F. R. Bouchet. Cosmological evolution of cosmic string loops. *Journal of Cosmology and Astroparticle Physics*, 2007(02):023–023, feb 2007.
- [140] F. Robinet et al. Omicron: a tool to characterize transient noise in gravitational-wave detectors, 2020. arXiv:2007.11374.
- [141] C. L. Rodriguez, B. Farr, W. M. Farr, and I. Mandel. Inadequacies of the Fisher information matrix in gravitational-wave parameter estimation. *Phys. Rev. D*, 88:084013, Oct 2013.
- [142] J. D. Romano. Searches for stochastic gravitational-wave backgrounds, 2019. arXiv:1909.00269.
- [143] J. D. Romano and Neil. J. Cornish. Detection methods for stochastic gravitational-wave backgrounds: a unified treatment. *Living reviews in relativity*, 20, 2017.

- [144] I. M. Romero-Shaw, C Talbot, et al. Bayesian inference for compact binary coalescences with Bilby: Validation and application to the first LIGO–Virgo gravitational-wave transient catalogue. *Monthly Notices of the Royal Astronomical Society*, Sep 2020.
- [145] J. Roulet et al. Template bank for compact binary coalescence searches in gravitational wave data: A general geometric placement algorithm. *Phys. Rev. D*, 99:123022, Jun 2019.
- [146] S. Roy, A. S. Sengupta, and P. Ajith. Effectual template banks for upcoming compact binary searches in advanced LIGO and Virgo data. *Phys. Rev. D*, 99:024048, Jan 2019.
- [147] S. Sachdev, T. Regimbau, and B. S. Sathyaprakash. Subtracting compact binary foreground sources to reveal primordial gravitational-wave backgrounds. *Phys. Rev. D*, 102:024051, Jul 2020.
- [148] A. Samajdar and T. Dietrich. Waveform systematics for binary neutron star gravitational wave signals: Effects of the point-particle baseline and tidal descriptions. *Phys. Rev. D*, 98:124030, Dec 2018.
- [149] A. Samajdar and T. Dietrich. Waveform systematics for binary neutron star gravitational wave signals: Effects of spin, precession, and the observation of electromagnetic counterparts. *Phys. Rev. D*, 100:024046, Jul 2019.
- [150] L. Santamaría, B. Krishnan, and J. T. Whelan. Searching for numerically simulated signals from black-hole binaries with a phenomenological template family. *Classical and Quantum Gravity*, 26(11):114010, may 2009.
- [151] L. Santamaría, F. Ohme, P. Ajith, et al. Matching post-newtonian and numerical relativity waveforms: Systematic errors and a new phenomenological model for nonprecessing black hole binaries. *Phys. Rev. D*, 82:064016, Sep 2010.

- [152] M. Sasaki, T. Suyama, et al. Primordial black holes—perspectives in gravitational wave astronomy. *Classical and Quantum Gravity*, 35(6):063001, Feb 2018.
- [153] A. Sharma and J. Harms. manuscript in preparation.
- [154] A. Sharma and J. Harms. Searching for cosmological gravitational-wave backgrounds with third-generation detectors in the presence of an astrophysical foreground. *Phys. Rev. D*, 102:063009, Sep 2020.
- [155] X. Siemens, V. Mandic, and J. Creighton. Gravitational-wave stochastic background from cosmic strings. *Phys. Rev. Lett.*, 98:111101, Mar 2007.
- [156] R. Smith and E. Thrane. Optimal search for an astrophysical gravitational-wave background. *Phys. Rev. X*, 8:021019, Apr 2018.
- [157] T. Souradeep. LIGO-India. *Resonance*, 21:225–231, 2016.
- [158] A. Taracchini, A. Buonanno, Y. Pan, et al. Effective-one-body model for black-hole binaries with generic mass ratios and spins. *Phys. Rev. D*, 89:061502, Mar 2014.
- [159] E. Thrane, N. Christensen, and R. M. S. Schofield. Correlated magnetic noise in global networks of gravitational-wave detectors: Observations and implications. *Phys. Rev. D*, 87:123009, Jun 2013.
- [160] M. S. Turner. Detectability of inflation-produced gravitational waves. *Phys. Rev. D*, 55:R435–R439, Jan 1997.
- [161] T. Vachaspati and A. Vilenkin. Gravitational radiation from cosmic strings. *Phys. Rev. D*, 31:3052–3058, Jun 1985.
- [162] M. Vallisneri. Use and abuse of the Fisher information matrix in the assessment of gravitational-wave parameter-estimation prospects. *Phys. Rev. D*, 77:042001, Feb 2008.

- [163] E. Vangioni, K. A. Olive, et al. The impact of star formation and gamma-ray burst rates at high redshift on cosmic chemical evolution and reionization. *Monthly Notices of the Royal Astronomical Society*, 447(3):2575–2587, 01 2015.
- [164] V. Varma et al. Surrogate model of hybridized numerical relativity binary black hole waveforms. *Phys. Rev. D*, 99:064045, Mar 2019.
- [165] J. Veitch, V. Raymond, et al. Parameter estimation for compact binaries with ground-based gravitational-wave observations using the LALInference software library. *Phys. Rev. D*, 91:042003, Feb 2015.
- [166] J. Veitch and A. Vecchio. Bayesian coherent analysis of in-spiral gravitational wave signals with a detector network. *Phys. Rev. D*, 81:062003, Mar 2010.
- [167] S. Vitale, W. M. Farr, et al. Measuring the star formation rate with gravitational waves from binary black holes. *The Astrophysical Journal*, 886(1):L1, nov 2019.
- [168] B. Von Harling, A. Pomarol, et al. Peccei-quinn phase transition at LIGO. *Journal of High Energy Physics*, 2020(4):195.
- [169] C. W. Misner, K. S. Thorne, and J. A. Wheeler. *Gravitation*. Princeton University Press, 2017.
- [170] A. R. Williamson, J. Lange, et al. Systematic challenges for future gravitational wave measurements of precessing binary black holes. *Phys. Rev. D*, 96:124041, Dec 2017.
- [171] B. Willke et al. The GEO-HF project. *Classical and Quantum Gravity*, 23(8):S207–S214, mar 2006.

- [172] X. J. Zhu, E. Howell, T. Regimbau, et al. Stochastic gravitational wave background from coalescing binary black holes. *The Astrophysical Journal*, 739(2):86, sep 2011.
- [173] X. J. Zhu, E. J. Howell, et al. On the gravitational wave background from compact binary coalescences in the band of ground-based interferometers. *Monthly Notices of the Royal Astronomical Society*, 431(1):882–899, 03 2013.